Thermoelectrics and Aerogels for Solar Energy Conversion Systems

by

Kenneth McEnaney

Submitted to the Department of Mechanical Engineering
in partial fulfillment of the requirements for the degree of

Doctor of Philosophy

at the

MASSACHUSETTS INSTITUTE OF TECHNOLOGY

February 2015

Author .....
Department of Mechanical Engineering
September 30, 2014

Certified by .....
Gang Chen
Carl Richard Soderberg Professor of Power Engineering
Thesis Supervisor

Accepted by .....
David E. Hardt
Chairman, Department Committee on Graduate Theses

Thermoelectrics and Aerogels for Solar Energy Conversion Systems

by

Kenneth McEnaney

Submitted to the Department of Mechanical Engineering
on September 30, 2014, in partial fulfillment of the
requirements for the degree of
Doctor of Philosophy

Abstract

Concerns about climate change, the world's growing energy needs, and energy independence are driving demand for solar energy conversion technologies. Solar thermal electricity generation has the potential to fill this demand. Solar thermal technology could also be used to displace fossil fuels in applications which require heat as an input. This thesis addresses the potential of two solar thermal technologies: solar thermoelectric generators and aerogel-based solar thermal receivers.

Thermoelectrics are materials which produce a voltage when subjected to a temperature gradient. In a solar thermoelectric generator (STEG), sunlight heats one end of the thermoelectric materials, generating a voltage across the device. The voltage can be connected to a load and useful work can be extracted. By adding optical concentration and using higher-temperature materials, the power output and energy conversion efficiency of STEGs can be increased. In this work, segmented thermoelectric generators (TEGs) made of bismuth telluride and skutterudite alloys are modeled, optimized, built, and tested. These TEGs achieve a heat-to-electricity conversion efficiency of 10.7% at a hot side of 550 °C, the highest TEG efficiency reported in this temperature range. From these TEGs, STEGs are built which achieve a sunlight-to-electricity conversion efficiency of 5.7% at less than 60 suns, higher than the best reported literature values in this concentration range. With further improvements, it is projected that these STEGs will achieve 10% efficiency at 100 suns.

In any type of solar thermal system, heat losses from the system must be suppressed to achieve high efficiency. Aerogels, which are stable ultra-low density foams, can suppress radiative and convective losses. It is shown that aerogel-based solar thermal receivers can increase the efficiency of traditional solar thermal electricity and hot water generation. These results can help advance the field and expand the scope of solar thermal technologies.

Thesis Supervisor: Gang Chen
Title: Carl Richard Soderberg Professor of Power Engineering

Acknowledgments

Great collaborations under the guidance of my advisor Professor Gang Chen and my committee member Professor Zhifeng Ren allowed this thesis to come to fruition. At MIT, Daniel Kraemer gave helpful advice every step of the way, from the initial simulations to device construction, testing, and analysis. I cannot thank him enough for his help. All the simulations were based on the properties of materials synthesized and characterized at the University of Houston under Professor Ren. Specifically, Dr. Qing Jie made all the skutterudites and Dr. Weishu Liu made all of the bismuth telluride segments. Their development of excellent thermoelectric materials and contact materials is what made exceeding 10% efficiency a possibility. For the solar thermoelectrics, Dr. Feng Cao in Professor Ren's lab developed the selective surfaces for this project.

I would also like to thank my committee members Professor John Lienhard V and Professor Evelyn Wang for providing helpful advice and a different perspective on the work. Thanks also go to Leslie Regan in the Graduate Office of the Department of Mechanical Engineering for her assistance in navigating the degree process. The members of the NanoEngineering Group have also been a great resource for work and a fun group to spend time with.

Outside of work, I would like to thank a number of people and groups at MIT that made my time here so enjoyable. Daniel Kraemer, Poetro Sambegoro, and Kimberlee Collins were always available for a coffee, no matter what time of day (or night). The entire house team in Burton-Conner and especially the residents of Burton Five provided a fantastic living experience for four years. Jose Gomez-Marquez, Anna Young, Amit Gandhi, and the staff at D-Lab gave me great opportunities to explore fun technical problems.

Finally, I'd like to thank those closest to me for sticking out these six years with me. My mother, father, superstar sister, and the rest of my family are a constant source of happiness for me. Most importantly, I would like to thank my amazing wife Jaime. She was unfailingly supportive for the past six years, never complaining about

the long hours and stress for both of us so I could complete graduate school at MIT. To her I owe an enormous debt of gratitude.

Contents

List of Figures

List of Tables

Chapter 1

Introduction

Access to energy is projected to be one of the defining global engineering challenges of the twenty-first century. The human population continues to increase, naturally increasing the demand for energy. More of the world is being lifted out of poverty, and as income levels rise, so do levels of consumption, including energy. Climate change should also be encouraging us to conserve energy and to find renewable clean sources of it. Harnessing the energy of the sun appears to be one of the best ways to address the energy challenge.

1.1 The Energy Landscape

The world's primary energy sources can be broadly divided into three categories: fossil fuels including coal, petroleum, and natural gas; nuclear energy; and renewables including wind, hydropower, solar, geothermal, biomass, and others. Fossil fuels provide more than 80% of our primary energy; biofuels, mainly for heating and cooking, contribute 10%; and nuclear contributes 5%. That leaves less than 5% of our energy from hydropower and other renewables[1]. This is despite the abundance of solar power; our average global primary power consumption of 19 TW is still three orders of magnitude smaller than the solar power striking the earth.

Given its abundance, there should clearly be room for solar in the energy landscape. However, solar energy still produces less than 1% of the world's electricity.[2]

This solar electricity is produced by photovoltaic (PV) panels, or it can be produced by concentrated solar thermal (CSP) plants, where the sun's rays are concentrated to heat up a fluid which is coupled to a steam turbine or other traditional power block. The vast majority of the solar electricity produced today comes from photovoltaics: globally, by the end of 2013 there were 139 GW of photovoltaic capacity installed, compared to just 3.4 GW of CSP capacity[3].

Solar thermal energy conversion, where sunlight is first converted into heat before being used such as in CSP plants, has huge potential. Thermal storage can be added to solar thermal energy conversion to add much-valued dispatchability to the energy flow, and thermal systems can integrate with, and use highly refined technology of, existing fossil fuel or nuclear power plants. Solar thermal systems can also be used for domestic hot water or space heating, eliminating costly components and efficiency barriers involved in the conversion to electricity.

1.1.1 Solar Thermal Energy Conversion

The most common solar thermal energy conversion technology is domestic water heating. In 2013, 45 GW of solar thermal capacity (GW_{th}) was installed worldwide, bringing the installed total to an estimated 330 GW_{th}[3]. The most basic solar domestic hot water application is for hot water for showers and swimming pools. The water is circulated through a black pipe or set of pipes placed in a sunny location. The pipes absorb the sunlight, heating the water passing through them before it is directed to the pool or shower.

The same basic principle can be used to produce hot water for domestic consumption, although the operating temperature must be higher if the system incorporates a storage tank. Typical domestic hot water tanks maintain the water at a temperature of at least 65 °C in order to prevent Legionnaire's Disease. There are a wide variety of configurations for solar hot water systems. The water can be circulated through the system with a pump, or the temperature gradients within the system can be used as a thermosyphon to drive the flow; water can flow continuously through the system, or a batch of water can be left to sit in the solar collector for a period of time, heating

it up significantly; and the system could be direct, where the fluid which is desired to be warmed is passed through the collector, or it could have a heat exchanger in which the fluid that passes through the collector can transfer its heat to another fluid.

Solar collectors can be designated as either concentrating or non-concentrating. In concentrating collectors, there are optics such as lenses or mirrors to concentrate the light to the receiver. In non-concentrating collectors, the receiver is directly exposed to the sunlight. The receiver itself is usually in one of three configurations: flat panel, evacuated tube, or Sydney tube. Flat panel receivers have a large, usually rectangular absorbing surface. Water or another fluid passes through a series of tubes attached to the bottom of the absorbing surface to extract the heat. Insulation is often installed below the absorber and fluid loop to prevent heat leakage through the bottom side to the surroundings. For weather protection and to reduce heat losses, a transparent plate (usually glass) is suspended above the absorbing surface. A metal or plastic frame encases the entire receiver. Evacuated tube receivers differ in that they comprise a single evacuated glass tube which surrounds the absorbing surface and fluid loop. Often the fluid loop is a narrow U-shaped tube, two concentric counterflow tubes, or a heat pipe. The absorber attached to the fluid loop is often metal so that it easily conducts the heat from the whole absorber inward to the fluid loop. The absorber is usually a wavelength-selective surface with high solar absorptance and low thermal emittance. The ends of the evacuated tube have a metal-to-glass seal around the fluid loop. The Sydney tube, a modification of the standard evacuated tube, is made by evacuating the space between two concentric glass tubes. The glass tubes are closed on one end, and sealed to each other on the other end. The outer surface of the inner tube is coated in a selective surface and acts as the solar absorber. The heat is conducted radially through the glass to the inner surface of the inner glass tube, where it is delivered to the fluid loop. The Sydney tube exchanges the difficult metal-to-glass seal of an evacuated tube with a simple glass-to-glass seal; they also replace the metal absorber with the inner glass tube, reducing the cost of the system. Because the thermal resistance of the Sydney tube's inner glass tube is larger than that of the metal fin used in typical evacuated tubes, thermal losses are larger in the

Sydney tube. Another difference is that the entire perimeter of the Sydney tube's inner glass tube is coated in the selective surface, whereas for a typical evacuated tube the absorbing surface is just one side of a fin. This means that Sydney tubes have relatively larger radiation losses than evacuated tubes. Being symmetric in the θ direction, Sydney tubes avoid the cosine losses in evacuated tubes caused by the flat absorber not being rotated perpendicular to the sun.

Compared to flat panel receivers, evacuated tubes are more efficient because flat panels have higher convection losses. Sydney tubes fall between flat panel and evacuated tube receivers in both cost and efficiency. The efficiencies of these systems as a function of the temperature difference between the fluid and the environment are shown in figure 1-1.

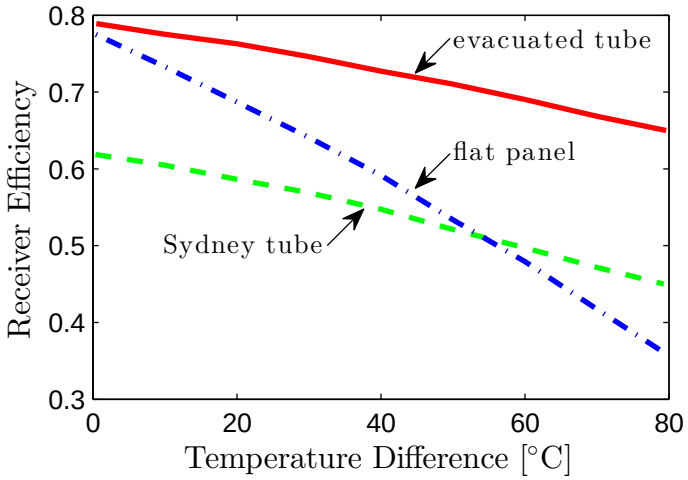

Figure 1-1: Efficiency of an evacuated tube (red solid line), Sydney tube (green dashed line), and flat panel collector (blue dash-dotted line) as a function of the temperature difference between the fluid and the environment. Data from NARVA[4].

Solar energy can also be converted into electricity by first converting it into heat, and then using a heat engine to convert the heat into electricity. The benefits of such systems are that heat engines are very mature technologies, and that thermal storage is fairly straightforward. In order to reach the temperatures required by the heat engine, these systems employ solar concentration and are called concentrated solar power (CSP) systems. CSP systems are classified based on their optics; the most

common are parabolic trough, linear Fresnel, dish, and power tower. Parabolic trough systems use a linear parabolic mirror to reflect light onto a receiver tube located at the focus of the parabola, and can reach solar fluxes of 60 suns ($60\,\mathrm{kW\,m^{-2}}$)[5]. The receiver tube is usually evacuated similar to a domestic hot water evacuated receiver, but the absorber is the coated fluid pipe which is illuminated on nearly all sides. Linear Fresnel systems are similar to parabolic trough systems, except that the parabolic mirror is replaced by a series of adjustable flat mirrors that act as a Fresnel reflector. Linear Fresnel concentrators can reach fluxes of 70 suns[6]. Dish reflectors are parabolic reflectors which focus sunlight onto an absorber surface at its focus. Unlike parabolic troughs and linear Fresnel concentrators, dish reflectors track the sun with two degrees of freedom and concentrate the light in two dimensions, producing on the order of 1000 suns on the absorber surface[7], or higher if secondary optics are used[8]. The dish reflector is usually many mirror facets as opposed to a true continuous parabola. The absorber is not usually evacuated, since at higher concentrations the reflection losses introduced by the added glass outweighs the greenhouse effect it could create. Power tower CSP systems use a field of heliostats to reflect the sunlight onto an absorber mounted on a large tower. These systems achieve fluxes in excess of 1000 suns and therefore, like CSP dish systems, do not employ a vacuum in front of the absorber.

1.2 Solar Thermoelectric Generators

The heat from a solar thermal receiver can also be used to drive a heat engine in the form of a thermoelectric generator. Thermoelectric generators are devices which convert a heat flux into electricity. They are based on the Seebeck effect, where a temperature gradient across a thermoelectric material generates a voltage. The proportionality constant between the temperature difference across the thermoelectric material and the voltage that is produced is the material's Seebeck coefficient:

$$S = -\frac{dV}{dT} \tag{1.1}$$

Thermoelectric materials are either classified as p-type or n-type, depending on whether the majority carriers inside the material are holes or electrons. The Seebeck coefficient of a p-type material is positive, while that of an n-type material is negative. Due to this difference in sign, if a p-type material and an n-type material are put thermally in parallel and electrically in series, the magnitudes of their Seebeck voltages will add, producing a larger output voltage. This configuration is called a thermoelectric couple or unicouple, and is shown schematically in figure 1-2. The voltage output of this unicouple can be attached to a load, resulting in electrical power being extracted from the unicouple.

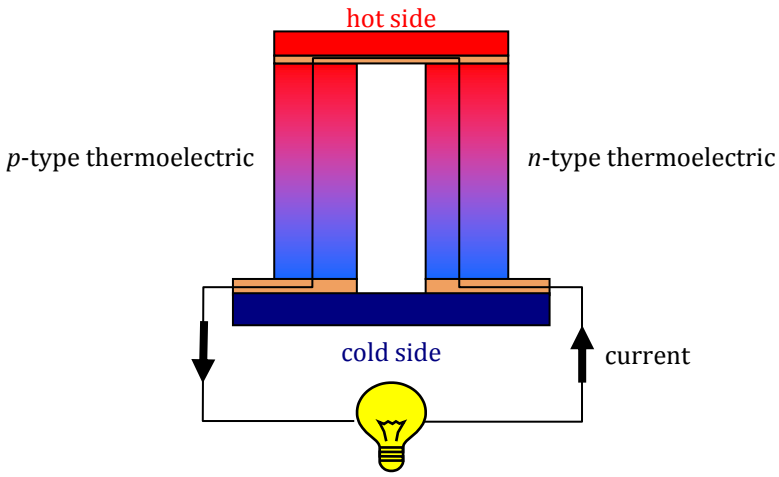

Figure 1-2: When a p-type and an n-type thermoelectric material are connected thermally in parallel and electrically in series, their Seebeck voltages add together. This voltage can be used to drive an electric load.

To power a load, the thermoelectric materials must not just have high Seebeck coefficients; analogous to a battery, the legs' electrical conductivities, σ, should be high so that a current can flow with minimal impedance from the "internal resistance" of the device. A high output voltage and low internal resistance will produce a large amount of electricity. If the device's conversion efficiency is to be high, the heat flux should be kept to a minimum, and thus the thermal conductivity, k, should be low. When all of these material properties are combined to assess the efficiency with which a thermoelectric material converts heat into electricity, the dimensionless figure of merit is[9]:

$$zT = \frac{S^2\sigma}{k}T \tag{1.2}$$

Heavily-doped semiconductors often show the right combination of material properties to have a high zT[10]. As early as the 1940s, thermoelectric materials such as bismuth telluride and zinc antimony were being tested as thermoelectric generators[11]. Materials that have been shown to have a peak zT in excess of 1 include silicon germanium alloys[12]; V-VI compounds of bismuth, tellurium, antimony, and selenium[13–15]; IV-VI compounds based off of lead telluride or selenide[16–23]; lead antimony silver telluride (LAST)[24, 25]; tellurium antimony germanium silver (TAGS)[26]; indium selenide[27]; skutterudites[28–30]; lanthanum telluride[31]; Tl_9BiTe_6[32]; Zn_4Sb_3[33]; the zintl $Yb_{14}MnSb_{11}$[34]; low-dimensional materials such as superlattices[35] or quantum dot structures[36]; and more. Detailed reviews of thermoelectric materials and theory abound in the literature[37–40].

Most of the attention to thermoelectrics has focused on finding materials with a high peak zT; much less work has been devoted to building and testing thermoelectric generators. Prior to 1947, the highest demonstrated TEG efficiencies were less than 1%[11]. In 1947, Telkes measured the efficiencies of several TEGs, although the heat inputs to the legs were estimated, not measured directly. With this technique she reported efficiencies of 4.2% for a zinc antimonide and bismuth antimonide couple at a hot-side temperature of 250 °C, and 7% for a zinc antimonide and lead sulfide couple under a 400 °C temperature difference. In 1962, Himle et al. measured a zinc antimonide and lead telluride TEG efficiency of less than 3%[41]. Later that decade, Fuschillo et al. measured a bismuth telluride TEG with an efficiency of 4.4% at a hot side of 245 °C and a cold side of 70 °C[42]. In 1995, Gross et al. measured 3% efficiency from a higher manganese silicide and iron disilicide TEG at a cold side of 100 °C and a hot side of 700 °C[43]. In 2001, Caillat et al. measured the power output from a skutterudite TEG. From simulations they estimated the heat flux into the TEG, and calculated an efficiency of approximately 10% at a cold side of 90 °C and a hot side of 590 °C[44]. Two years later, El-Genk et al. measured the efficiency of

such a skutterudite TEG to be 7.3%; the authors postulated that sidewall losses were the reason the efficiency did not reach the predicted 10%[45]. In 2009, Crane et al. measured 10% TEG efficiency with TAGS and bismuth telluride p-type legs and lead telluride and bismuth telluride n-type legs[46]. In 2011, D'Angelo et al. measured a segmented module with lead tin telluride and bismuth telluride p-type legs and lead antimony telluride and bismuth telluride n-type legs. They measured 6.6% with the hot side at 400 °C and the cold side at 23 °C[47]. Guo et al. measured 8% efficiency for a skutterudite TEG operating between 50 °C and 600 °C in 2012[48]. In 2013, Muto et al. measured a skutterudite TEG; the efficiency when corrected for parasitic losses was calculated to be 9.1% operating between 70 °C and 550 °C[49]. This year, Salvador et al. measured a skutterudite TEG operating between 500 °C and 40 °C; the efficiency was 7%[50]. The most efficient TEG to date is a 15% segmented device operating between 1000 °C and 150 °C. The p-type leg comprised a zintl $Yb_{14}MnSb_{11}$ and a skutterudite; the n-type leg was lanthanum telluride and a skutterudite[51]. Commercially, thermoelectrics used in conjunction with radioisotope generators for space power are 8% efficient[52].

In a solar thermoelectric generator (STEG), the sunlight is absorbed by the absorber, and the heat is conducted to the thermoelectric generator. The first patent for a STEG was filed in 1888[53]. The first STEG was demonstrated in 1922, and had an efficiency of less than 0.01%[54]. Telkes made major advances when she published her 1954 results demonstrating 0.63% efficiency without concentration, and 3.35% efficiency at 50X concentration[55]. From the late 1950s through the 1970s, most of the experiments and modeling papers were focused on space-based STEGs[41,56–61]. Later papers focused on concentrating STEGs[62], with a module by Amatya and Ram reaching 3% efficiency at 66 suns concentration[63], and Dent and Cobble achieving 6.3% under very high optical concentration with a solar furnace[64]. Both of those efficiencies were based on the flux incident upon the absorber. In 2011, Kraemer et al. returned the focus to unconcentrated STEGs, demonstrating 4.7% efficiency based on the flux incident on the evacuated glass tube[65]. Following his work, the potential for STEGs using optical concentration with multiple thermoelectric materials systems

has been explored[66]. The demonstration of such a system is the focus of chapter 3. For an extensive review of solar thermoelectrics, the reader is referred to [67].

1.3 Thesis Outline

This thesis focuses on two topics: solar thermoelectric generators (STEGs), and aerogel-based solar receivers. In chapter 2, the modeling, optimization, and testing of segmented bismuth telluride and skutterudite thermoelectric generators as engines for STEGs are presented. These optimized TEGs can exceed 10% efficiency with a hot side of 550 °C. In chapter 3, a STEG design methodology is presented. This methodology is used to design a STEG capable of operating at temperatures up to 600 °C. The STEG is built and tested, and the results are presented. This is the first STEG built with skutterudite and bismuth telluride segmented TEGs. In chapter 4, a receiver is designed for hot water and solar thermal electricity generation applications. The receiver, based around aerogels to reduce losses even at high temperatures with only moderate concentrations (less than 100 suns), shows promise as a viable solar thermal technology. Chapter 5 summarizes the new ideas and technology presented in the thesis, and suggests a path for future work on these topics.

Chapter 2

Segmented Thermoelectric Generator Development

For thermoelectrics to impact the energy landscape, effective devices incorporating thermoelectric materials must be developed. For power generation, this entails combining p- and n-type materials into a thermoelectric generator (TEG). A single thermoelectric generator unicouple comprises one p-type and one n-type leg (Fig. 2-1). In this work each leg is segmented, comprising a bismuth telluride segment and a skutterudite segment in order to efficiently convert heat to electricity across a large temperature range. Each segment incorporates its own contact electrodes at the ends, which provide good electrical and thermal contact to the thermoelectric material. The contact electrodes also promote stability by limiting diffusion into or out of the thermoelectric materials. The development of the thermoelectric materials and contact electrodes for this project was carried out by our collaborators at the University of Houston under the guidance of Professor Zhifeng Ren.

In this chapter, progress in the modeling and testing of segmented thermoelectric generator unicouples is presented. First, a model for optimizing a single thermoelectric leg is presented which incorporates the effects of the temperature-dependent zT, materials stability, contact resistance, and parasitic losses. Next, two legs are optimized as a pair to form a thermoelectric generator unicouple. The optimized unicouple is then built and tested, with the results compared to the model.

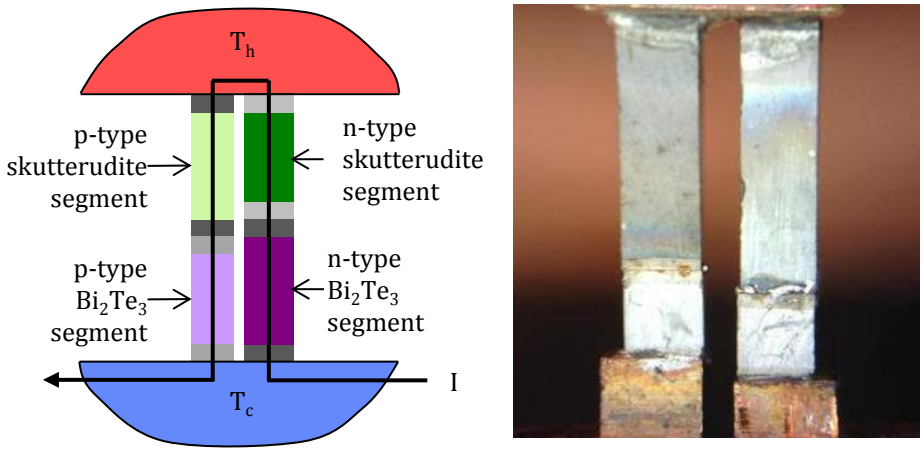

Figure 2-1: Schematic (left) and photograph (right) of a segmented TEG. Each thermoelectric material is bounded by thin contact electrode layers.

2.1 Thermoelectric Leg Modeling

A schematic of a single thermoelectric leg is shown in figure 2-2. Heat Q flows from the heat source at a temperature T_h through the thermoelectric leg to the cold sink at temperature T_c. To calculate the thermal and electrical flow, the leg is discretized in the z-direction into thin slices, as shown in figure 2-2. Domenicali's equations[37] conserving energy and current are discretized and applied to each slice[68], resulting in the coupled equations Eq. (2.1) and Eq. (2.2) which are valid for the thermoelectrics as well as the contact electrodes.

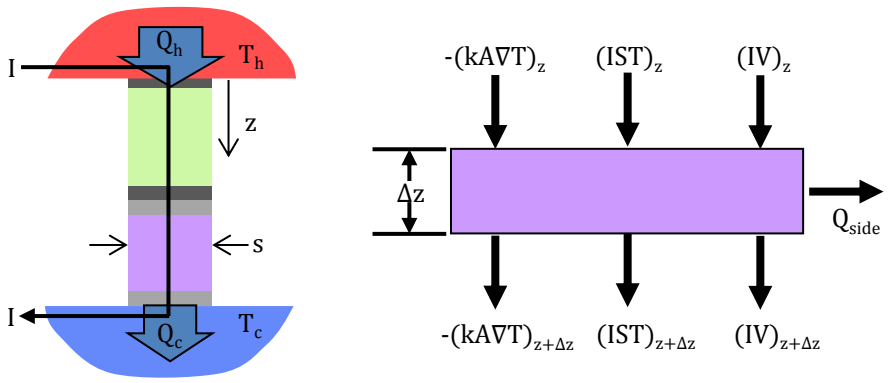

Figure 2-2: Each material in the thermoelectric generator is discretized in the z-direction (down the leg). Using a slice as a control volume, energy and current are conserved, taking into account thermoelectric effects as outlined by Domenicali[37].

$$dT = \frac{IST - Q}{kA} dz \tag{2.1}$$

$$dQ = I^2 \rho \frac{dz}{A} + IS\,dT - Q_{side} \tag{2.2}$$

Here T is the temperature, I is the electric current, dz is the slice thickness, and $A = s^2$ is the cross-sectional area of the leg. The Seebeck coefficient S, thermal conductivity k, and electrical resistivity ρ are all temperature-dependent. The total heat current, Q, can be thought of as the sum of the Fourier heat and a thermoelectric heat (Eq. (2.3)).

$$Q = -kA\frac{dT}{dz} + IST \tag{2.3}$$

Equation (2.2) is a slight modification of that presented by Hogan and Shih[68] in order to capture the parasitic heat losses from the sidewall of the slice, Q_{side}. The three terms in equation (2.2) can be though of as the Joule heating, the Thomson effect, and a sidewall loss. If the thermoelectric generator is in vacuum, the sidewall loss is purely radiative:

$$Q_{side} = \sigma_{sb}\,\epsilon\,p\,dz\left(T^4 - T_{amb}^4\right) \tag{2.4}$$

where σ_{sb} is the Stefan-Boltzmann constant, ϵ is the emittance of the sidewall of the thermoelectric leg, $p = 4s$ is the perimeter of the leg, and T_{amb} is the ambient temperature.

Applying equations (2.1) through (2.4) implies the following assumptions:

- *The system is at steady-state.* There are no transient thermal or capacitative terms.

- *The leg sidewalls only see an environment at T_{amb}.* The legs do not exchange radiation with each other, with themselves (including reflections), or with the hot side. It is assumed that the ambient temperature T_{amb} is the same as the cold-side temperature T_c. This assumption and Eq. (2.4) will be modified in

subsection 2.1.4.

- *The material properties are solely a function of temperature.* Each contact electrode or thermoelectric region is a homogeneous material. The properties within a homogeneous material may vary due to the non-isothermal temperature profile in the region.

- *The temperature, heat flow, and electrical current flows are uniform across the cross-section of the leg.* This Biot number for the thermoelectric legs used in this thesis is always less than 0.05.

The metric used to evaluate the leg is the leg efficiency η_{leg}, which is the electrical power produced by the leg, P_{el}, divided by the total heat flux entering the hot end of the leg, Q_h. This definition of efficiency assumes that there is no other heat input into the leg, for example radiation from a hot enclosure. In these simulations we assume the environment is at the same temperature as the cold end of the leg, so the leg is always hotter than the environment and thus the radiative heat flux is always a loss from the leg, not a heat gain.

$$\eta_{leg} = \frac{P_{el}}{Q_h} \tag{2.5}$$

2.1.1 Material Properties

These thermoelectric generators will be made from skutterudite and bismuth telluride thermoelectric elements. The skutterudites are stable up to 600 °C[30], while bismuth telluride alloys are usually only stable to 280 °C. The bismuth telluride materials are incorporated into the device because they have a higher zT than skutterudites at lower temperatures (Fig. 2-3). The temperature-dependent Seebeck coefficients, thermal conductivities, and electrical conductivities of the thermoelectric materials are shown in figures 2-4 to 2-7.

Each thermoelectric material has its own contact electrode material. The contact electrodes should be highly thermally and electrically conductive in order to reduce

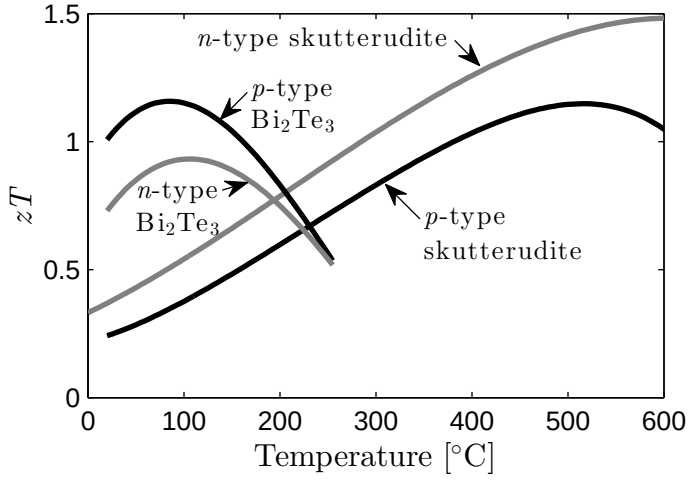

Figure 2-3: The temperature-dependent zT of the thermoelectric materials used in this thesis.

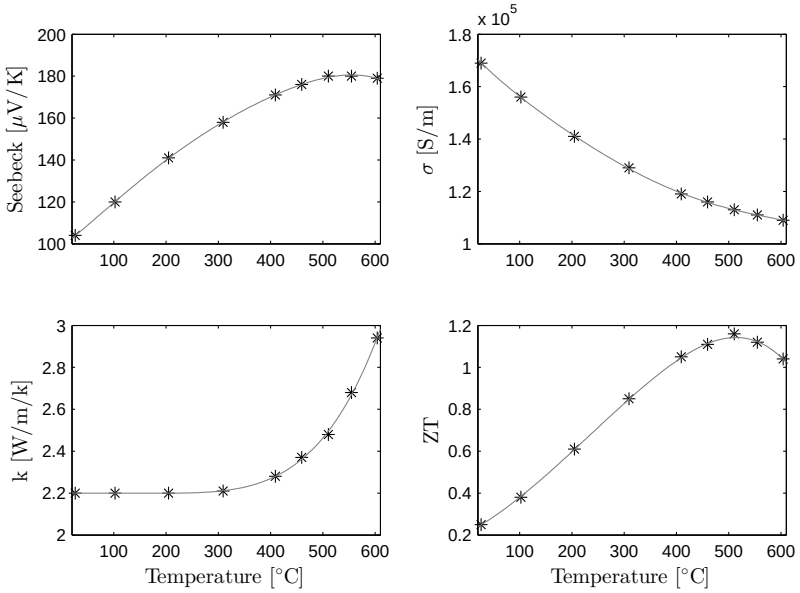

Figure 2-4: Thermoelectric properties of the p-type skutterudite used in this thesis.

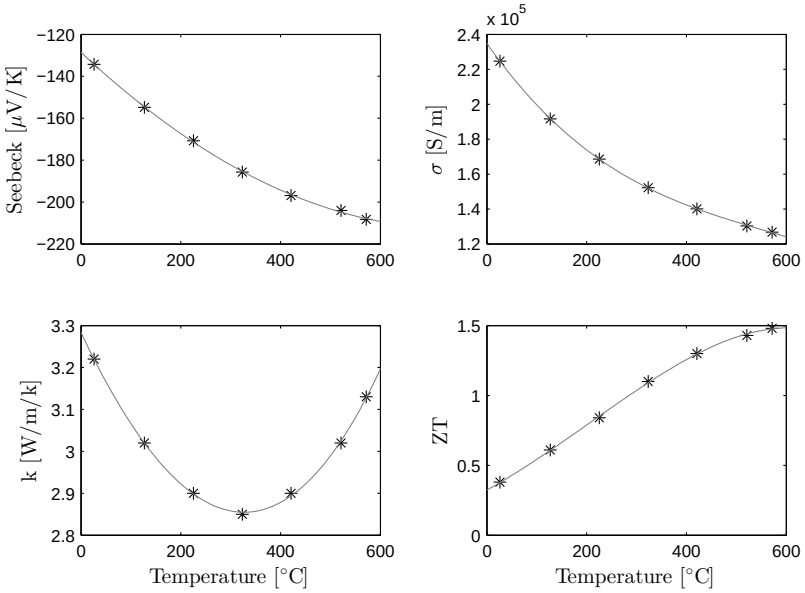

Figure 2-5: Thermoelectric properties of the n-type skutterudite used in this thesis.

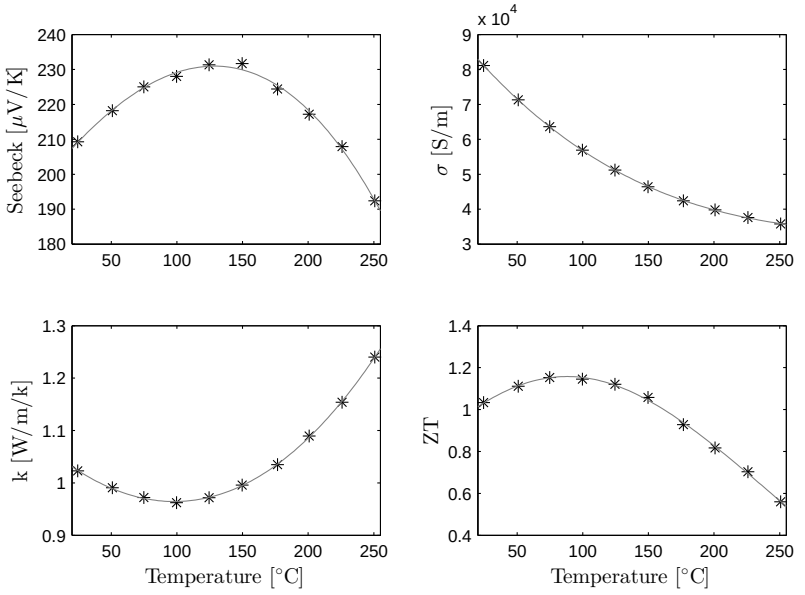

Figure 2-6: Thermoelectric properties of the p-type Bi_2Te_3 material used in this thesis.

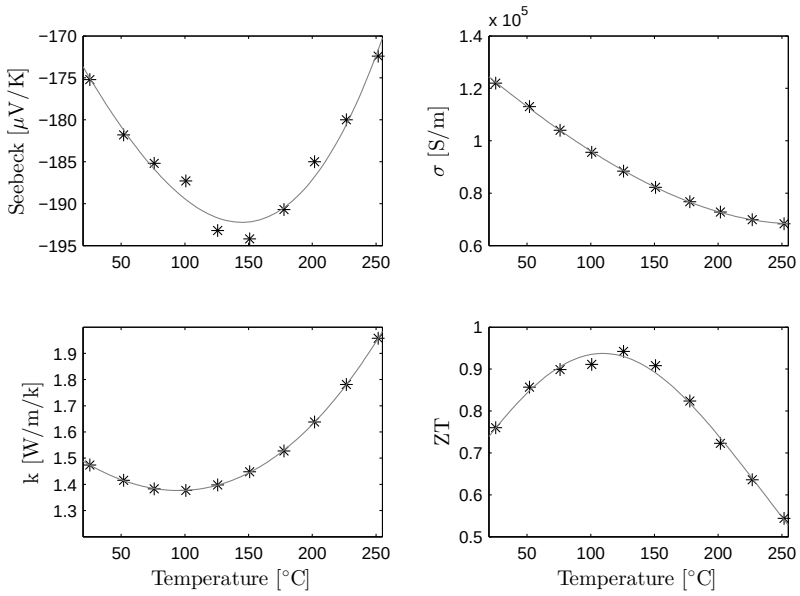

Figure 2-7: Thermoelectric properties of the n-type Bi_2Te_3 material used in this thesis.

the parasitic effects of voltage and temperature drops across the contact electrodes as opposed to across the thermoelectric materials. They should also have complementary or near-zero Seebeck coefficients, i.e. the Seebeck should be the same sign as the adjacent thermoelectric material. The properties of the contact electrode materials are shown in figures 2-8 to 2-11. The interfacial contact resistances between the thermoelectrics and their contact electrodes have been measured. For the n-type bismuth telluride and its contact electrode, the interfacial contact resistance is $4 \times 10^{-10}\,\Omega\,\mathrm{m}^2$. For the p-type bismuth telluride and its contact electrode, the interfacial contact resistance is less than $1 \times 10^{-10}\,\Omega\,\mathrm{m}^2$. For the n-type skutterudite and its contact electrode, the interfacial contact resistance is less than $1 \times 10^{-10}\,\Omega\,\mathrm{m}^2$. For the p-type skutterudite and its contact electrode, the interfacial contact resistance is less than $1 \times 10^{-10}\,\Omega\,\mathrm{m}^2$. All measurements of the contact electrodes and the interfacial contact resistances were performed at the University of Houston.

The spectral emittances of the skutterudite thermoelectrics were measured at room temperature with an FTIR (Fig. 2-12(a)). The skutterudites are most critical since they are at the highest temperature, and they comprise most of the length of the thermoelectric legs. From these FTIR data we can infer the emittance as a

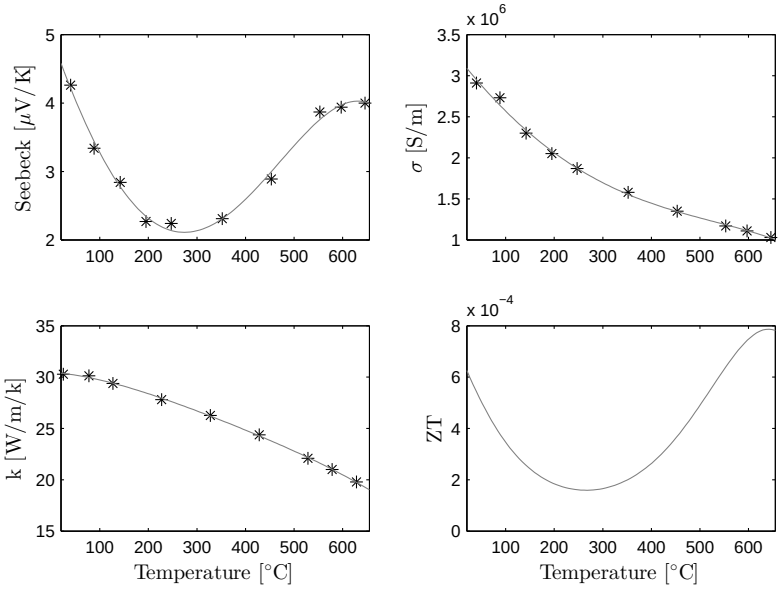

Figure 2-8: Thermoelectric properties of $Cr_{0.3}Fe_{0.6}Ni_{0.1}$, the p-type skutterudite contact electrode material used in this thesis.

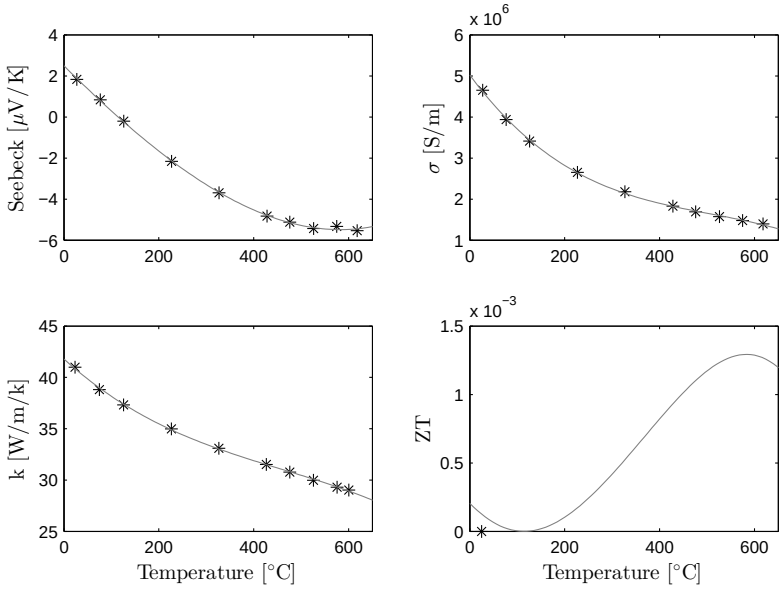

Figure 2-9: Thermoelectric properties of $CoSi_2$, the n-type skutterudite contact electrode material used in this thesis.

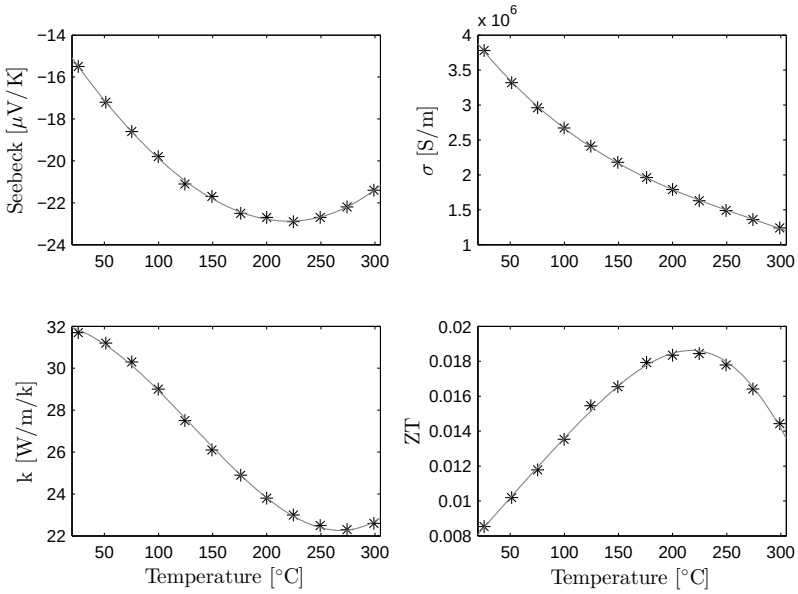

Figure 2-10: Thermoelectric properties of pressed Ni, the p-type Bi_2Te_3 contact electrode material used in this thesis.

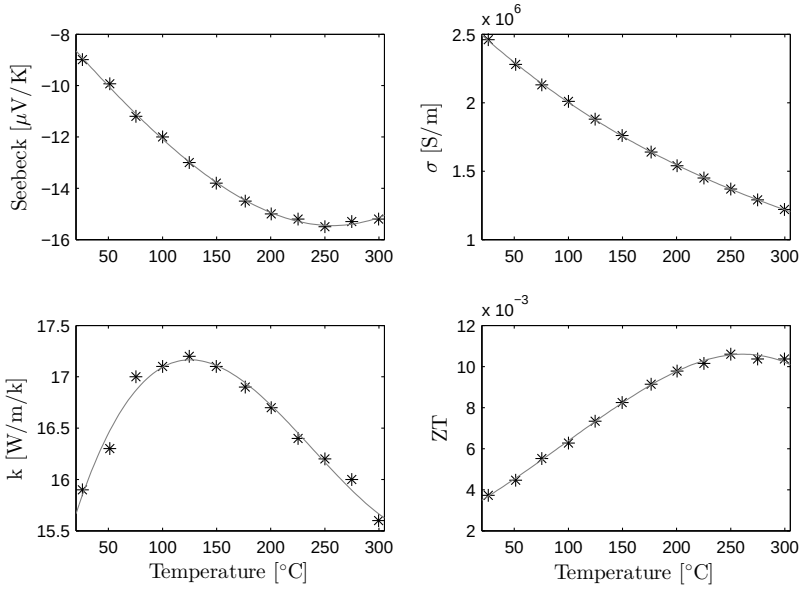

Figure 2-11: Thermoelectric properties of FeS_2-doped $Ni_{0.85}In_{0.15}$, the n-type Bi_2Te_3 contact electrode material used in this thesis.

function of temperature. From 300 °C to 600 °C, the calculated emittance values are approximately 0.5 (Fig. 2-12(b)). These values do not consider that the spectral properties could be temperature-dependent. In addition, the FTIR measures reflectance at near-normal incidence and does not take into account a directional dependence of the reflectance. An integrating sphere was not used with the FTIR, but the polished legs appear to be specularly reflecting in the visible, which suggests that they are also specular for longer wavelengths as well. A good discussion of uncertainties in high-temperature emittance measurements was written by Kraemer et al.[69].

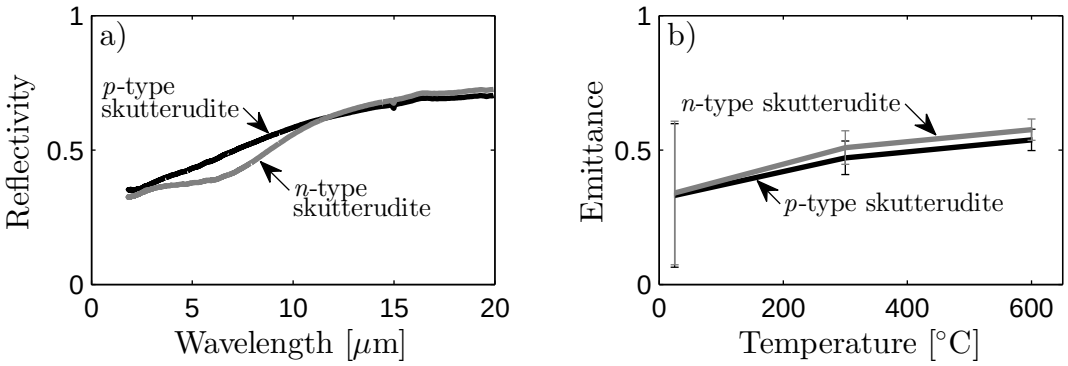

Figure 2-12: (a) Near-normal spectral emittance of polished skutterudites, measured at room temperature. (b) Inferred temperature-dependent emittance, calculated by integrating room-temperature spectral properties and the blackbody spectrum of various temperatures.

2.1.2 Leg Geometry Optimization

Once the material properties and interfacial contact resistances are known, the cross-sectional area and length of each thermoelectric segment and each contact can be adjusted to optimize the thermoelectric performance. For ease of manufacturing and to prevent spreading resistances, the cross-sections of the thermoelectric segments and contact electrodes within a given leg are the same. Ideally, the contact electrodes would be made negligibly thin. However, thicker contacts are easier to manufacture. In addition, thicker contacts better serve to separate the thermoelectric material from the brazing and soldering materials used to join the parts together. Realistically, the

thinnest each contact can be made in our hot-pressing process is 0.3 mm.

There are three first-order effects seen when optimizing the leg geometry. First, the relative length of the bismuth telluride segment compared to that of the skutterudite segment determines how much of the overall temperature drop occurs across each segment. For short bismuth telluride segments, nearly all of the temperature drop will occur across the skutterudite and there will be only a very small temperature gradient across the bismuth telluride element. Care must be taken to not make the bismuth telluride segment too long with respect the the skutterudite length, or else the hot side of the bismuth telluride segment will be pushed beyond the bismuth telluride's operating temperature limit.

For example, a p-type skutterudite and bismuth telluride leg is simulated, varying the fraction of the total leg length which is bismuth telluride. When the fraction is zero, the leg is solely skutterudite; when the fraction is 1, the leg is entirely bismuth telluride. The materials used are the materials presented in section 2.1.1. There are no contact electrodes, no interfacial contact resistance, and no radiation losses from the leg. Various hot-side temperatures are simulated, with the cold side fixed at 50 °C. The performance is not plotted if the temperature of the bismuth telluride would exceed 255 °C, since that is the highest temperature at which the materials have been tested. The results are presented in figure 2-13. For each hot-side temperature, the maximum efficiency occurs at the point where the midpoint temperature between the bismuth telluride and the skutterudite is approximately 230 °C, which is very close to the temperature at which the zT of the skutterudite begins to exceed that of the bismuth telluride (Fig. 2-3). The only exception is the simulation where the hot-side temperature is fixed at 200 °C, as for over this entire temperature range the bismuth telluride has a higher zT than the skutterudite. Thus the optimum configuration in this case is a leg which is entirely bismuth telluride.

The second first-order effect is that the overall length of the leg determines the relative importance of the parasitic losses caused by the interfacial contact resistances and the contact electrodes. As the legs are made shorter, the finite resistance values of the interfacial contact and the contact electrodes (set at their minimum possible

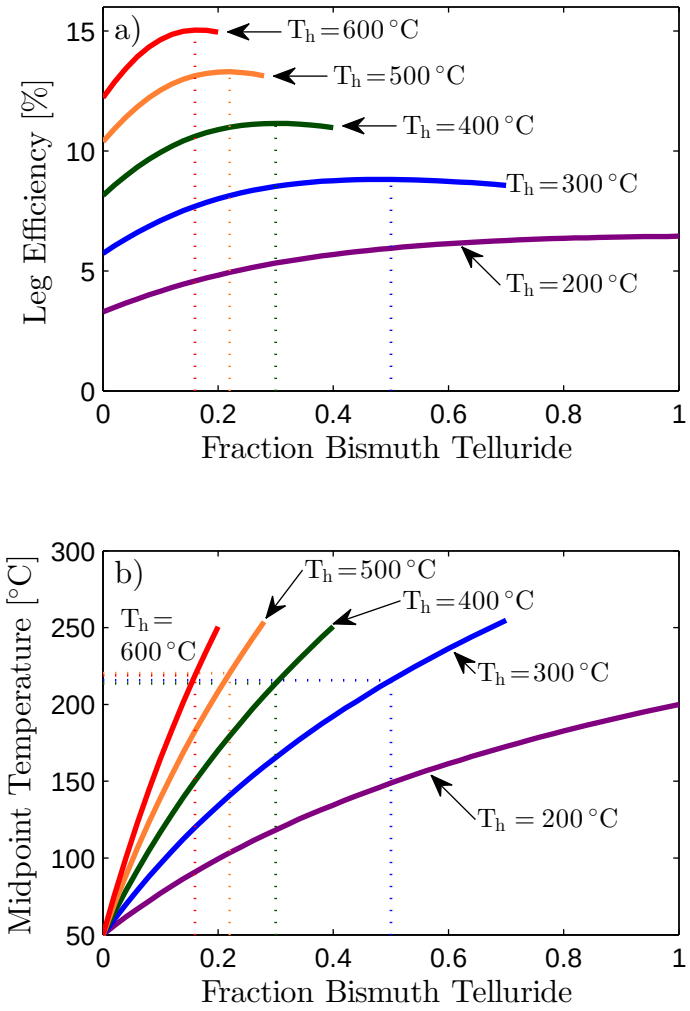

Figure 2-13: The (a) efficiency and (b) maximum bismuth telluride temperature of a skutterudite and bismuth telluride segmented leg as a function of the fraction of the leg which is bismuth telluride. The results are plotted for five different hot-side temperatures; the cold side is fixed at 50 °C. Results are not plotted if the maximum temperature within the bismuth telluride segment would exceed 255 °C.

thickness) begin to dominate the total electrical and thermal resistance of the leg, reducing the leg performance. In very long legs, the intrinsic electrical and thermal resistances of the thermoelectric segments are large, and the parasitic effects of the contacts are minimized (note that parasitic effects of radiation losses from the sidewalls are not yet included). The parasitic electrical resistance effects are seen in figure 2-14. In this simulation, the performance of a segmented p-type leg with a cold side at 50 °C and a hot side of 600 °C is calculated. The overall length of the leg is varied, but interfacial contact resistances of $1 \times 10^{-10}\,\Omega\,\mathrm{cm}^2$ are included, as are contact electrodes 0.3 mm in length. It is critical to note that this simulation does not include convective or radiative losses from the sidewalls of the leg; these effects are the focus of the third first-order effect described below.

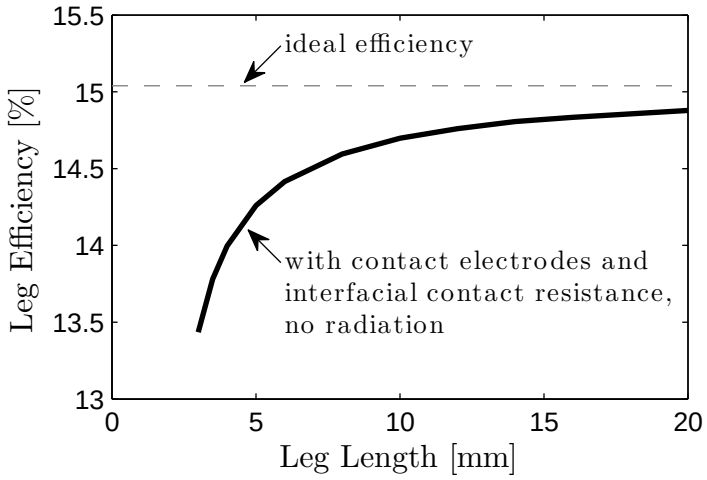

Figure 2-14: Efficiency of a p-type thermoelectric leg as a function of the length of the leg. The solid line is the calculated efficiency with contact electrodes and interfacial contact resistance. Each of the four contact electrodes is 0.3 mm long. The hot-side temperature is 600 °C; the cold side is at 50 °C. There are no radiation losses in this simulation. The efficiency of longer legs asymptotically approaches the case where contact electrodes and interfacial contact resistance are neglected (dashed line).

The third first-order effect is that the geometry determines the relative importance of the sidewall losses from the legs. To examine the effect of sidewall radiative losses, we will simulate a p-type segmented leg, ignoring interfacial contact resistance and contact electrodes for the moment. We will also assume that the hot side is fixed at

600 °C and the cold side is fixed at 50 °C. Additionally, it is assumed that there are no convective losses. The heat loss will be proportional to the emittance of the leg ϵ_{leg}, which is assumed to be the same for both thermoelectric materials and independent of temperature. The heat loss is also proportional to the surface area of the leg, which for a square leg of cross-sectional area $s \times s$ and length L is $4sL$. The heat flux down the leg is proportional to the effective thermal conductance of the leg, which has a geometric factor of s^2/L. The relative importance of the radiative losses, f_{rad}, is the ratio of these two terms:

$$f_{rad} = \frac{4sL\epsilon_{leg}}{s^2/L} = 4\epsilon_{leg}\frac{L^2}{s} \tag{2.6}$$

With respect to radiative losses, shorter legs have a twofold advantage: first, they have a smaller overall surface area; second, they have lower thermal resistance which results in a higher through-leg heat flux. Legs with larger cross-sectional area (larger s), although they have larger radiative losses, have higher efficiency because the increase in through-leg heat flux (proportional to the cross-sectional area) is larger than the increase in the radiative losses (proportional to the perimeter). The calculated efficiencies for two emittances and various leg geometries (s and L) are plotted as a function of the radiative loss factor f_{rad} in figure 2-15. As expected, the efficiencies collapse onto a single curve, confirming the validity of $4\epsilon_{leg}L^2/s$ as the independent parameter which determines the radiative losses for these materials and operating conditions.

To optimize the geometry, all three effects must be simulated at the same time, as each effect affects the other. For example, the thickness of the contacts will affect the temperature profile in the leg, which will affect the radiation losses. When these three effects are combined together, the optimal geometry is not bounded. A leg with a larger cross-sectional area will always be more efficient because of the smaller relative radiative losses. Legs with larger cross-sectional areas can also be longer without having so large a penalty from radiative losses. These longer legs reduce the parasitic effects of contacts, making the leg more efficient.

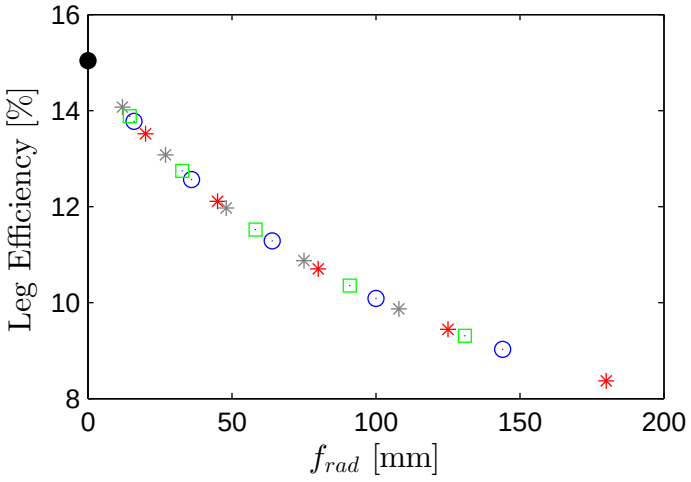

Figure 2-15: Efficiency of a segmented p-type thermoelectric leg as a function of the geometry of the leg. Results are plotted as a function of the radiative loss factor, $f_{rad} = 4\epsilon_{leg}L^2/s$. The black dot is the case with no radiative losses ($\epsilon = 0$). Legs with an emittance of 0.5 and lengths of 4, 6, 8, 10, and 12 mm are calculated for side lengths s=1.6 mm (red stars), s=2.0 mm (blue circles), and s=2.2 mm (green squares). The gray stars have the same geometry as the red stars, but with a lower emittance ($\epsilon_{leg} = 0.3$).

The full optimization was performed for the p-type leg. The emittance of the thermoelectrics and the contacts was assumed to be 0.5. The contact lengths were set at their minimum, 0.3 mm. As is expected, the leg efficiency increases with side length (Fig. 2-16). The optimal leg length, which is a balance between high parasitic contact losses at short lengths vs. high parasitic radiation losses at long lengths (Fig. 2-17), increases with increasing side length (Fig. 2-18). The optimal current for the optimal leg geometry increases rapidly with increasing side width (Fig. 2-19).

2.1.3 Limits on Geometry

The thicknesses of the contacts are not the only limits on a leg geometry. With our current manufacturing processes, it is difficult to make thermoelectric segments that are less than approximately 1.5 mm in length. There are also limits imposed by our testing facilities: with our most precise electrical sourcing and measurement equipment we are limited to 3 A of current. In order to be able to do on the leg

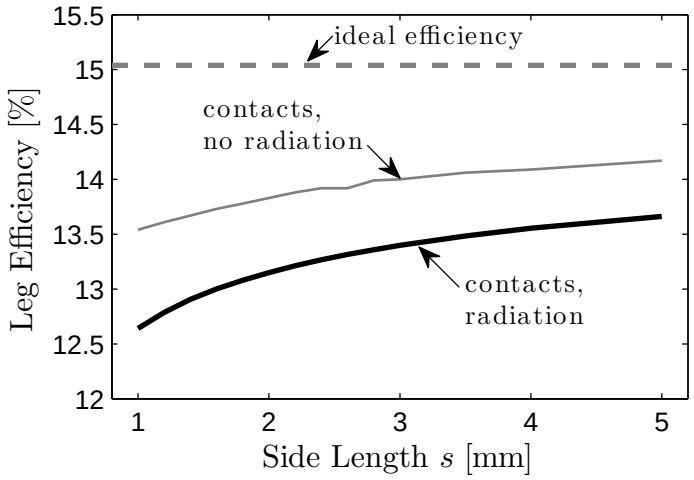

Figure 2-16: Efficiency of a segmented p-type thermoelectric leg as a function of the width of the side of the leg, s. The emittance of the leg is 0.5. The gray dashed line is the limit of no parasitic (radiative, contact electrode, or interfacial contact) losses. The gray solid line is the leg efficiency of a leg with the same geometry as the black line, but without radiation losses.

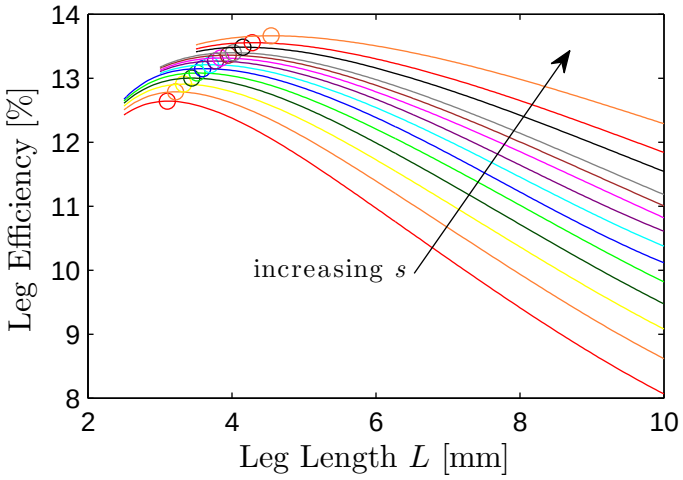

Figure 2-17: Efficiency of a segmented p-type thermoelectric leg as a function of the length of the leg, L, plotted for various values of the width of the side of the leg, s. The values of s are 1.0, 1.2, 1.4, 1.6, 1.8, 2.0, 2.2, 2.4, 2.6, 2.8, 3.0, 3.5, 4.0, and 5.0 mm. The emittance of the leg is 0.5. Legs with larger cross-sectional area (larger s) have higher efficiency, and the optimal L is longer.

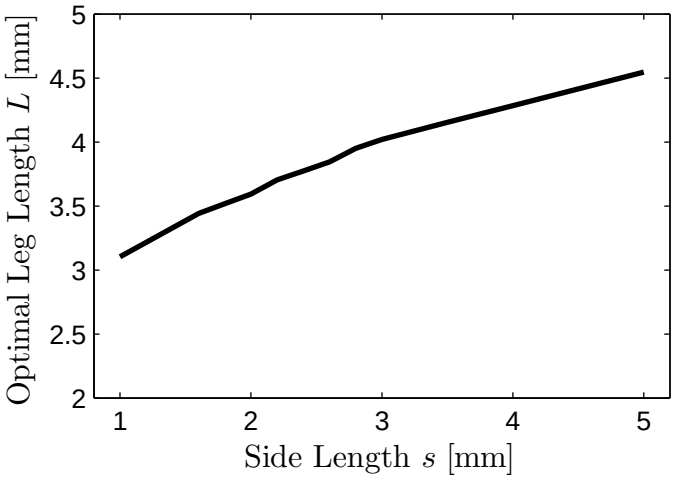

Figure 2-18: Optimal leg length L of a segmented p-type thermoelectric leg as a function of the width of the side of the leg, s. The emittance of the leg is 0.5.

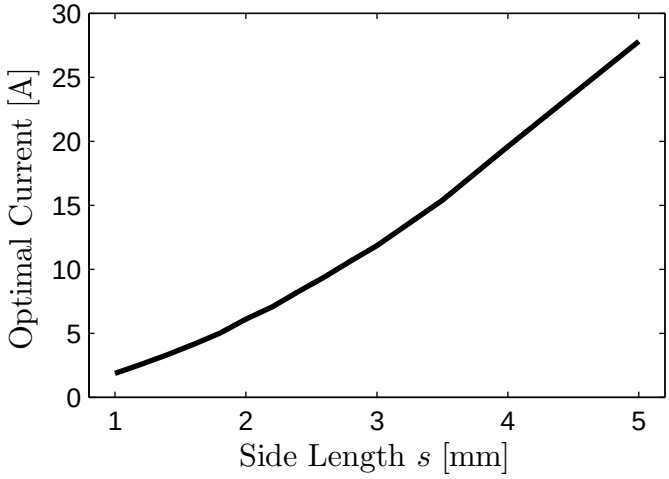

Figure 2-19: Optimal electrical current for a segmented p-type thermoelectric leg as a function of the width of the side of the leg, s. The emittance of the leg is 0.5.

an I-V sweep which extends slightly past the peak, and in order to have a small margin of safety in case of the device properties not exactly matching the model, we will aim to have the optimal current be less than 2.6 A. With these limits in place, we can calculate the performance of each thermoelectric leg. Because these bismuth telluride leg lengths are longer than what is optimal, there is strong pressure for the skutterudite legs to be shorter, which raises the hot-side temperature of the bismuth telluride. We want to make sure that the maximum temperature the hot end of the bismuth telluride could reach is less than 250 °C. The efficiency and optimal geometry of the legs are given in table 2.1. The hot-side temperature of the bismuth telluride segments, T_{mid}, stays below 250 °C.

Table 2.1: Individually optimized p- and n-type segmented thermoelectric legs.

	p-type	n-type
T_h [°C]	600	
T_{mid} [°C]	231	213
T_c [°C]	50	
T_{amb} [°C]	50	
Contact electrode thickness [mm]	0.3	
Skutterudite length [mm]	5.7	6.6
Bismuth telluride length [mm]	1.5	1.5
Cross-sectional side width [mm]	2.2	2.0
Leg efficiency	11.1%	11.7%

In the end, these manufacturing and testing limits reduce the predicted maximum efficiency of each leg to less than 12%, as opposed to the predicted ideal efficiencies of 15.1% for the p-type leg and 15.6% for the n-type leg.

2.1.4 Radiation Losses

Radiation losses clearly have a large effect on the efficiency of the thermoelectric legs. A radiation shield can be included to reduce the radiation losses from the

leg by reflecting some of the thermal radiation back to the leg. Because there is a temperature gradient along the thermoelectric leg, the calculation of the effect of a radiation shield becomes somewhat involved. A schematic of the radiation shield around the leg is shown in figure 2-20. The thermoelectric leg, in gray, is surrounded by four polished copper walls (yellow) set off by a gap of width g. The ends of the gap are faced by two surfaces, one at the hot end (red) and one at the cold end (blue).

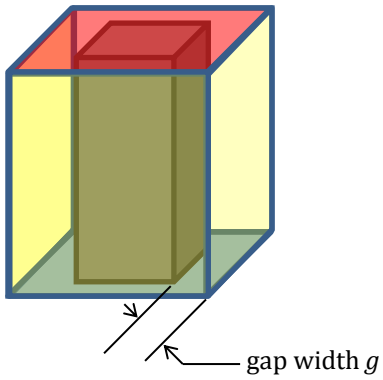

Figure 2-20: A thermoelectric leg (gray) is surrounded by four copper walls (yellow), all the same height at the thermoelectric leg. The distance between the leg and the walls, g, is the same on all four sides. The top and bottom of the gap space are bounded by a hot surface (red) at the top end and a cold surface (blue) at the bottom end.

To calculate the performance of the thermoelectric leg, the generalized radiation exchange factors between the discretized slices, the radiation shield, and the top and bottom surfaces must be calculated as a function of the surface emittances, specularities, the sidewall width s, the leg length L, and the gap distance g. The generalized radiation exchange factor, $\widetilde{F}_{ij}$, is the fraction of energy leaving slice/surface i that ends up being absorbed by slice/surface j. A ray tracing code was written to perform this calculation. For each slice, the code generates rays from the slice and traces where the energy ends up. Each ray's origin on the surface of the slice is random, as is its azimuthal direction. For the polar angle ϕ, a random number, *rand()*, is generated between zero and 1, and the polar angle is calculated as:

$$\phi = arcsin\left(\sqrt{rand()}\right) \tag{2.7}$$

such that the resulting rays should have a Lambertian distribution. These surfaces are assumed to be completely specular (specularity parameter p=1), with an emittance of 0.10. This emittance is a good estimate for the tungsten-coated stainless steel on the hot side, or the solder-covered cold shoe on the cold end. The copper radiation shield is assumed to be completely specular with an emittance of 0.03. The net heat transfer leaving a slice j is:

$$Q_{net,j} = \sigma_{sb}\epsilon_j A_j T_j^4 - \sum_{i=1}^{N} \widetilde{F}_{ij}\sigma_{sb}\epsilon_i A_i T_i^4 \tag{2.8}$$

where N is the total number of slices/surfaces, σ_{sb} is the Stefan-Boltzmann constant, A_n is the surface area of slice/surface n, T_n is the absolute temperature of surface n, and ϵ_n is the emittance of surface n. Figure 2-21 shows the exchange factors of the end, quarter point, and midpoint slices to the rest of the leg. Also plotted are the exchange factors from the hot side, cold side, and radiation shield (Fig. 2-23). In this simulation, the side width of the leg s is 2.2 mm and the leg length L is 8.4 mm, which matches the optimized dimensions of the p-type leg. The gap g is 0.2 mm. As is expected, the slices "see" themselves the most. The hot and cold ends "see" the slices nearest themselves the most. The radiation shield sees all the slices nearly evenly. When the gap between the radiation shield is increased, the distribution of the energy broadens, thus reducing the effectiveness of the radiation shield. The exchange factor for three different gaps are plotted in figures 2-22 and 2-24.

With these calculated exchange factors, the performance of the thermoelectric leg with the radiation shield can be calculated. The upper hot surface surrounding the top of the leg will be a net source of energy into the thermoelectric leg. This is accounted for by adjusting the definition of the thermoelectric leg efficiency to include this radiative heat flux from the hot upper surface, $Q_{h,rad}$, in the denominator (Eq. (2.9)) for these cases. The results are shown in figure 2-25. A radiation shield can be effective in increasing efficiency, even when the gap between the shield and the leg is as large as 1 mm.

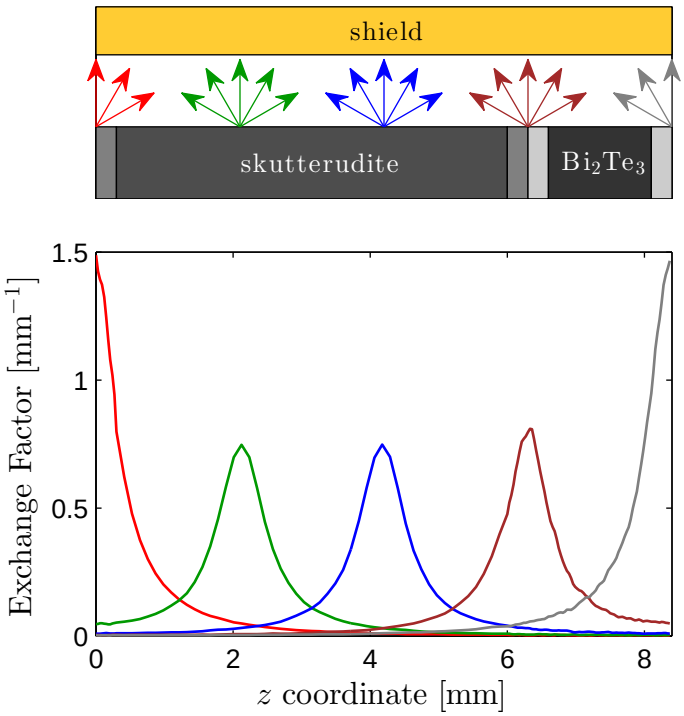

Figure 2-21: The exchange factor from the two end slices (red and gray), the two quarter point slices (green and brown, centered around quarter point), and the midpoint slice (blue, centered around midpoint) to the slices of the leg. The exchange factor is normalized to the length Δz of the receiving slice.

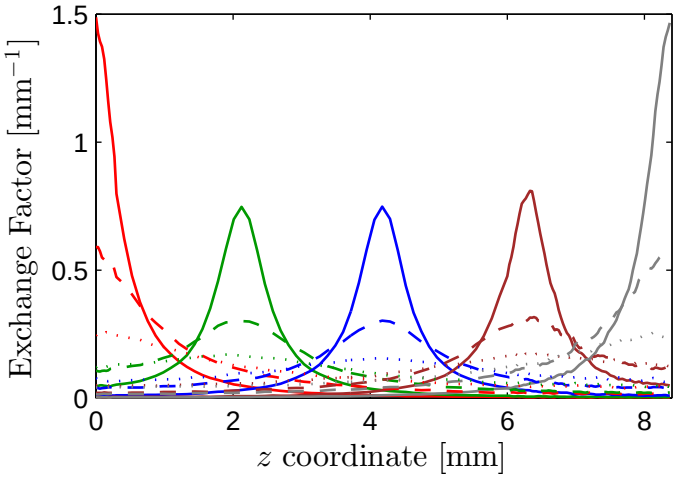

Figure 2-22: The exchange factors from various slices to the slices of the leg for three different gap sizes: g=0.2 mm (solid lines), g=0.5 mm (dashed lines), and g=1.0 mm (dotted lines). The exchange factor is normalized to the length Δz of the receiving slice.

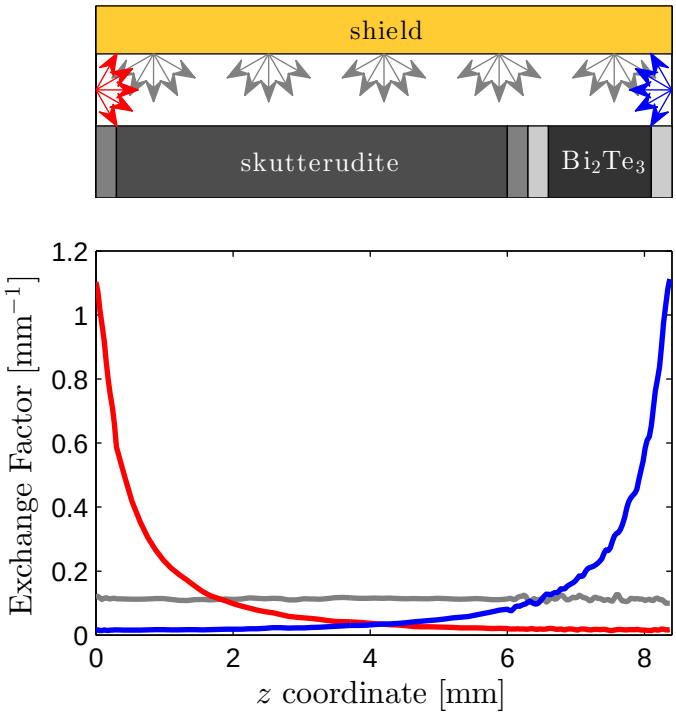

Figure 2-23: The exchange factor from the hot end (red), cold end (blue), and radiation shield (gray) to the slices of the leg. The exchange factor is normalized to the length Δz of the receiving slice.

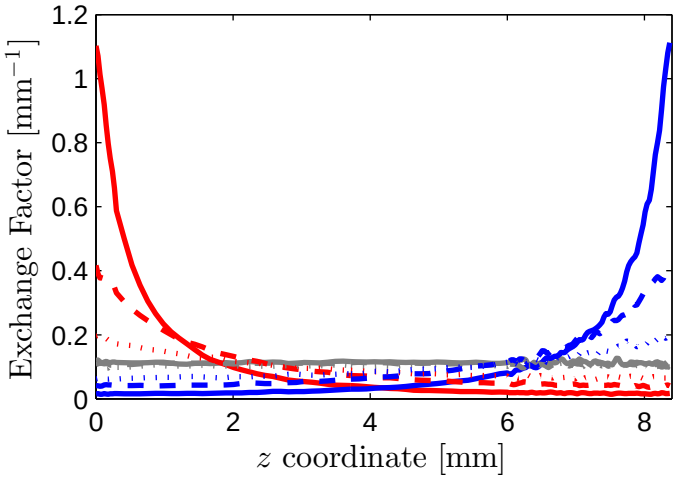

Figure 2-24: The exchange factor from the hot end (red), cold end (blue), and radiation shield (orange) to the slices of the leg for three different gap sizes: g=0.2 mm (solid lines), g=0.5 mm (dashed lines), and g=1.0 mm (dotted lines). The exchange factor is normalized to the length Δz of the receiving slice.

$$\eta_{leg} = \frac{P_{el}}{Q_h + Q_{h,rad}} \tag{2.9}$$

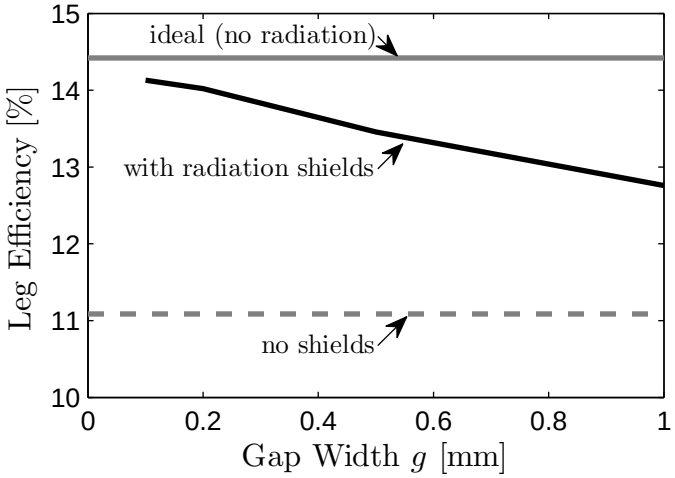

Figure 2-25: The efficiency of a p-type thermoelectric leg as a function of gap distance g as defined in figure 2-20. The leg geometry is the same as presented in table 2.1. The upper gray line is the upper limit of efficiency for this leg geometry, i.e. when there is no radiation exchange. The lower gray line is the efficiency with no radiation shields. The black line is the efficiency with radiation shields, defined in Eq. (2.9).

For the experiments in this thesis, it is difficult to know the exact emittance of the hot and cold surfaces at the top and bottom of the gap. In addition, there must be small gaps to the environment between the radiation shield and the hot side to ensure that the TEG does not short out electrically. However it is still instructive to know that radiation shields are quite beneficial, even at larger gap sizes.

2.2 Unicouple Modeling

The method described above is used to calculate the efficiency of both the n-type and p-type legs for a range of currents and geometries. In a TEG unicouple the same current passes through each thermoelectric leg. Thus, two leg geometries must be chosen such that they are provide the maximum combined efficiency for the pair. The efficiency of a unicouple TEG is:

$$\eta_{teg} = \frac{P_{el,p} + P_{el,n}}{Q_{h,p} + Q_{h,n}} \tag{2.10}$$

Depending on the efficiencies of the individual legs, the ideal current through the TEG may not be the ideal current of either of the legs; the leg with the lower efficiency may be made smaller in order to limit the heat flux through it, even if that means operating at a higher-than-ideal leg current. In the same way, the leg with the higher efficiency may be made larger in order to have more of the heat converted by it instead of the lower-efficiency leg. A deeper investigation of this topic can be found elsewhere in the literature[39]. Usually this effect is small - on the order of a few percent change in size - when the legs are as close in efficiency as the two simulated in the previous section. These small changes in size are smaller than the accuracy with which the thermoelectric legs can be made, and are smaller than the uncertainty in the material properties. Thus the leg sizes requested from our collaborators at the University of Houston are just those presented in Table 2.1, as both of these legs were already optimized for the same current (2.6 A).

2.3 Measurement

A test setup was built to measure the unicouple TEG efficiency. Our collaborators at the University of Houston made the thermoelectric samples. The samples were joined together at MIT and tested on our test stage. The experimental results were compared to simulations to validate the models.

2.3.1 Test Configuration

To test a TEG, the device must be sandwiched between a heat source and a cold sink at fixed temperatures T_h and T_c. The heat flux into the TEG from the top side must be monitored to calculate the efficiency of the TEG. The TEG must be electrically connected to a load resistance, and the output current and voltage is monitored as a function of load resistance.

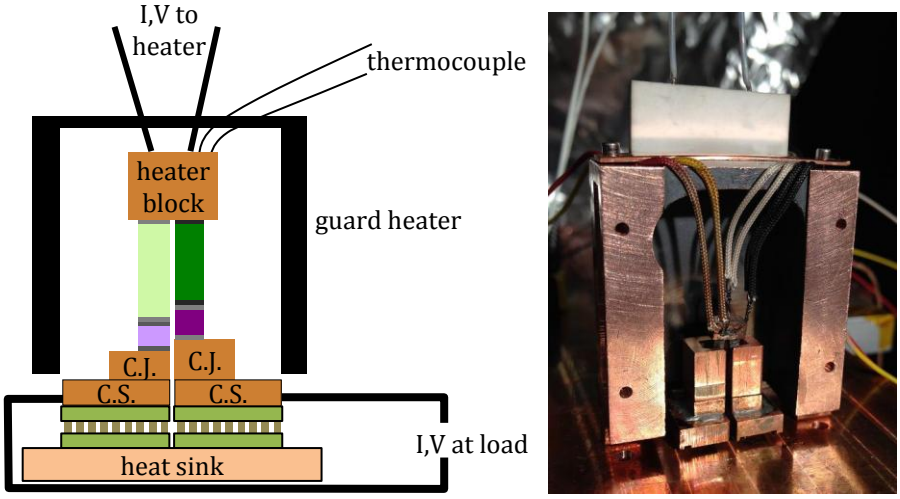

Figure 2-26: Schematic and picture of a TEG test setup. The thermoelectric legs are sandwiched between the heater block and the cold shoes (C.S.), using cold junctions (C.J.) to accommodate the difference in lengths of the thermoelectric legs. The cold shoes are maintained at a fixed temperature T_c via Peltier coolers. The Peltier coolers reject heat to a heat sink. The hot side temperature is maintained with an electric heater block. Radiation and wire conduction losses are reduced by the temperature-controlled guard heater. Leg radiation shields, shown in the picture, are not shown in the schematic.

A schematic and picture of a TEG in the test setup is shown in figure 2-26. In order to generate a temperature difference across the TEG, the bottom end of each leg of the TEG is attached to its own copper cold electrode, which is soldered to a cold junction. The cold junctions serve to accommodate the difference in lengths of the thermoelectric legs, and the have datums which align the radiation shields. The cold junctions are attached to the cold shoes, which are maintained at the temperature T_c by individually-controlled Peltier coolers. The Peltier coolers reject heat to a heat sink cooled with a fluid (water) loop. The temperatures of the cold shoes are monitored with T-type thermocouples. A K-type thermocouple monitors the heater block temperature. The heater block is a copper block with one or two $100\,\Omega$ RTDs brazed into it. The RTDs have an electrically insulating outer shell, isolating them electrically from the rest of the heater block. The heater block serves as the electrical connection between the p-type leg and the n-type leg. The power into the heater is supplied by a current source; the voltage across the heater is measured with the four-point method at the heater block to eliminate voltage drops in the wire. The

voltage and current produced by the TEG are measured with a source meter, and the voltage is mesaured with a four-point probe method at the cold shoes to eliminate voltage drops in the wires. In this setup, all the source meters are Keithley 2420 series; the TEG voltage is measured with a Keithley 2182 nanovoltmeter; and the temperatures are measured with a National Instruments NI-9214 thermocouple block. All instruments and signals are read and controlled by a computer running LabVIEW. The entire setup is placed in a vacuum chamber, with the pressure during the test below approximately 1×10^{-4} torr (0.013 Pa).

Of the electrical heater power put into the heater block, some passes into the thermoelectric legs. There are radiation losses to the environment, and conduction losses down the four 125 µm diameter copper electrical wires and two 125 µm K-type thermocouple wires. In order to reduce these losses, a guard heater is placed around the TEG and heater. The heat loss from the heater block to the guard heater should go to zero as the temperature of the guard heater approaches the temperature of the heater block. The guard heater is maintained at the temperature of the heater block. The guard heater is a copper chamber which has a 380 Ω platinum-core ceramic resistive heater attached to it. The guard heater is powered by an Agilent 5772 power supply, and its temperature is monitored with a K-type thermocouple.

In order to avoid radiation from the guard heater being absorbed by the thermoelectric legs, copper radiation shields are added around the thermoelectric legs. The radiation shields are thermally grounded to the cold junctions, maintaining them at the cold-side temperature.

2.3.2 Segmented TEG Assembly

Our collaborators at the University of Houston use a DC-current hot press technique to manufacture thermoelectric legs comprising a single thermoelectric pellet with contact electrodes attached at each end. These legs must be soldered or brazed together with the heater block and cold shoes. Since we are testing the TEGs up to 600 °C, the skutterudite legs are brazed to the heater block with a braze with a solidus temperature of 620 °C and a liquidus temperature of 650 °C. The braze is

56% Ag, 22% Cu, 5% Sn, and 17% Zn. The bismuth telluride legs are then attached to the skutterudite legs in one of two ways. For some legs we use a solder with a solidus temperature of 252 °C and a liquidus temprerature of 260 °C. This solder is 90% Pb and 10% Sn. Depending on the contact electrode materials, sometimes it is advantageous to introduce a piece of thin copper foil between the skutterudite leg and the bismuth telluride leg to encourage wetting of the solder. In this case, the copper foil is soldered to the skutterudite leg using a 92.5% Pb, 5% Sn, 2.5% Ag solder (solidus temperature 287 °C, liquidus temperature 296 °C), and then the bismuth telluride legs are soldered to the copper foil with the 252/260 °C solder. The cold junctions are attached to the bismuth telluride legs with 183 °C eutectic solder (63% Sn, 37% Pb). The leg radiation shields are soldered to the cold junctions with a 138 °C eutectic alloy (58% Bi, 42% Ni). Square connector posts on the cold junctions accommodate the difference in lengths of the thermoelectric legs, and also serve to locate the radiation shields. This allows us to have better control over the gap between the radiation shield and the thermoelectric legs2-27. Finally, the cold junctions are soldered to the cold shoes with a 118 °C eutectic solder (52% In, 48% Sn). All solders are in thin-film form, between 50 to 125 µm thick (Table 2.2).

Table 2.2: Brazes and solders used in the TEG assembly.

Solidus/ Liquidus [°C]	Composition	Thickness [μ m]	Flux
620/650	56% Ag, 22% Cu, 5% Sn, 17% Zn	125	Stay-Silv
287/296	92.5% Pb, 5% Sn, 2.5% Ag	50	Indalloy Flux #5RA
252/260	90% Pb, 10% Sn	125	Indalloy Flux #5RA
183	63% Sn, 37% Pb	50	Indalloy Flux #5RA
138	58% Bi, 42% Ni	50	Indalloy Flux #5RA
118	52% In, 48% Sn	50	Indalloy Flux #5RA

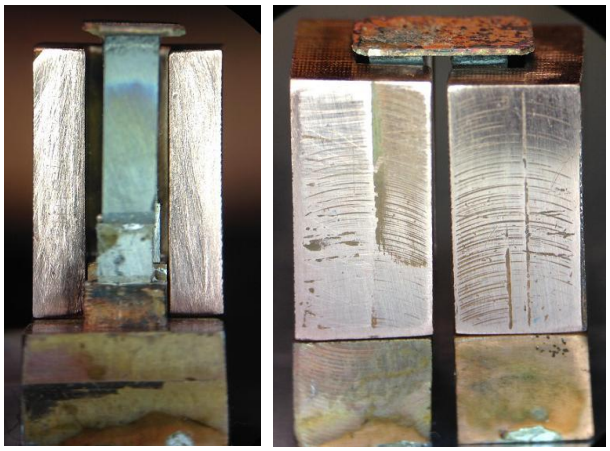

Figure 2-27: Each copper leg radiation shield sits around three sides of the thermoelectric leg. The alignment of the leg and the radiation shield is set by the square posts machined into the cold junctions. The gap between the radiation shield and the leg averages 0.5 mm. For this TEG, the skutterudite legs were brazed to a copper plate before being attached to the heater block.

2.3.3 Results

TEGs of various thermoelectric materials, contact electrodes, and geometries have been tested as our collaborators at the University of Houston improved their thermoelectric and contact electrode materials. The best to date are those materials presented earlier in this chapter. The legs which were tested are shown in figure 2-28. Their geometries are presented in table 2.3.

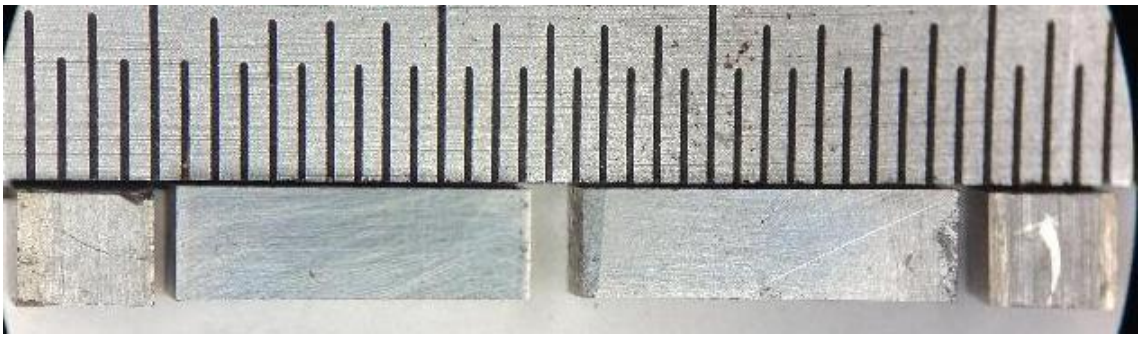

Figure 2-28: Individual leg segments prior to assembly. From left to right: p-type bismuth telluride, p-type skutterudite, n-type skutterudite, n-type bismuth telluride. The contact electrodes are clearly visible on the ends of the thermoelectric segments. The scale is in half millimeter increments.

The segments were assembled as mentioned in subsection 2.3.2. For these experi-

Table 2.3: Geometry of tested TEG components.

Leg	Cross-section [mm]	TE Segment Length [mm]	Contact Electode Lengths [mm]
p-type skutterudite	2.02 x 2.04	5.91	0.18 & 0.18
n-type skutterudite	1.96 x 2.04	6.27	0.35 & 0.25
p-type bismuth telluride	2.05 x 2.05	1.62	0.40 & 0.20
n-type bismuth telluride	2.01 x 2.03	1.47	0.34 & 0.34

ments, the hot side was swept from 100 °C to 550 °C. The cold side was maintained at 25 °C. At each temperature, the output current of the TEG was controlled by the source meter, effectively changing the external load resistance. At each current point, once the system was in thermal equilibrium (defined as each temperature staying within 0.05 °C of its set point temperature for thirty seconds) the TEG output voltage and heater block power were recorded. Then the electrical resistance of the leg was measured with an alternating DC resistance measurement. The mean amplitude of the alternating DC current was the TEG current set point; an added alternating current of 0.1 to 0.4 A was applied.

When the TEG is assembled, the leg and heater block surfaces can become somewhat tarnished, probably by oxidation. Because of this, the emittances of the surfaces of the tested TEG are unknown. Thus instead of comparing one simulation to the experimental results, simulations run with a range of emittances are compared to the experimental results. The simulation cases, which should bound the results of the experiment, are: I. leg emittance = 1 (worst case); II. leg emittance = 0 (upper limit); and III. leg emittance = 0.5 (as a guiding line). These cases are calculated without radiation shields. From the radiation shield calculations, it is expected that the results should fall between the $\epsilon = 0$ and $\epsilon = 0.5$ cases.

The emittances of the legs have little effect on the electrical properties, i.e. the open-circuit voltage and electrical resistance, of the TEG. Increasing the radiation lost from a leg will slightly lower the temperature profile across most of the leg (with-

out affecting the temperature right at the hot or cold boundary condition). Lower temperatures usually correspond to lower electrical resistance, so if the radiation losses on a leg increases, the leg should have a slightly lower electrical resistance. The open-circuit voltage will also be slightly affected by increased radiation losses. The sagging temperature profile means that more of the temperature drop will be in the skutterudite, and less in the bismuth telluride. Thus the temperature at the junction between the bismuth telluride and the skutterudite will be lower (i.e. suboptimal), and the open-circuit voltage will drop.

The emittance of the legs will have a large effect on the efficiency of the TEG, as has been shown in simulations. This is because radiation losses along the leg subtract from the amount of heat that is flowing down the leg and being converted to electricity. At the TEG level, higher emittance would be indistinguishable from higher thermal conductivities of the thermoelectric materials.

The results of the experiment are presented here. The TEG efficiency is 10.7% at a hot side of 550 °C and a cold side of 25 °C. The measured voltage vs. current and efficiency vs. current curves of the TEG at the different hot-side temperatures are shown in figures 2-29 and 2-30. The TEG efficiency is 15% to 30% below the efficiency we expect (Fig. 2-31).

To investigate why the efficiency is low, the individual properties are device are compared to the model. The device resistance is very close to the simulated values (Fig. 2-32), always within 2% of the predicted values. This indicates that the electrical resistivities of the materials, and contact resistances inbetween them, are very close to the as-modeled properties. Since the resistivities are temperature-dependent, it also suggests that the thermal model is giving good results. The accuracy of the thermal model is also confirmed by comparing the measured heater power to the simulations at the open-circuit condition (Fig. 2-33). The experiment matches the model well, falling between the $\epsilon = 0$ and $\epsilon = 0.5$ cases as expected.

The open-circuit voltage is shown in figure 2-34. It is approximately 12% lower than expected at all temperatures. One potential cause is that the Seebeck coefficient of at least one of the thermoelectric materials is low. A second potential cause is

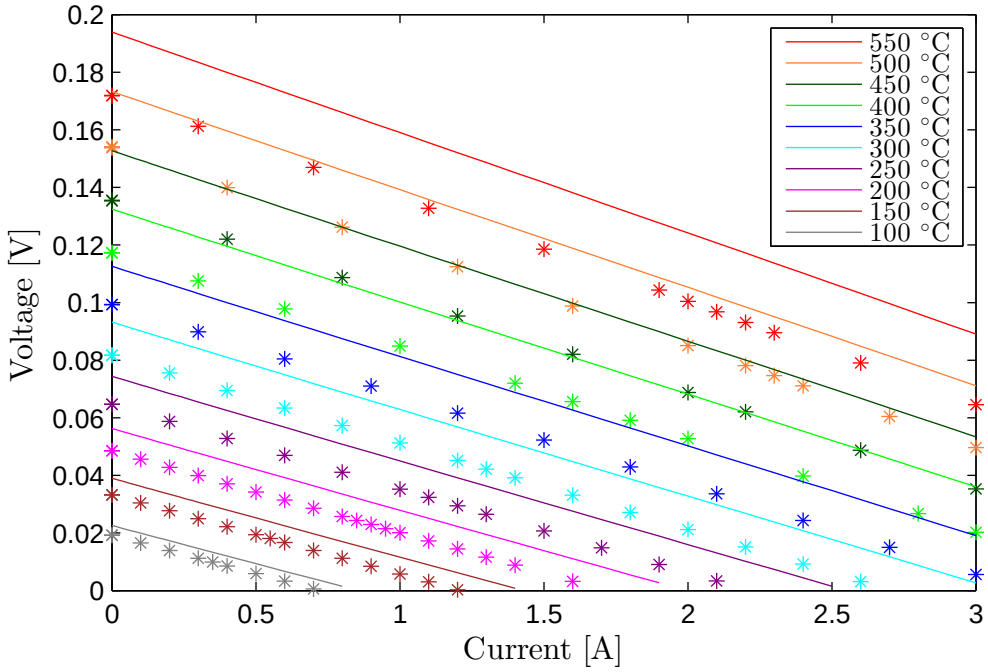

Figure 2-29: Segmented TEG voltage vs. current curves. The simulations shown (solid lines) are for a leg emittance of 0.5 with no radiation shields. The measured points are shown as asterisks. The different colors represent hot-side temperatures ranging from 550 °C (top, red) down to 100 °C (bottom, gray) in 50 °C increments.

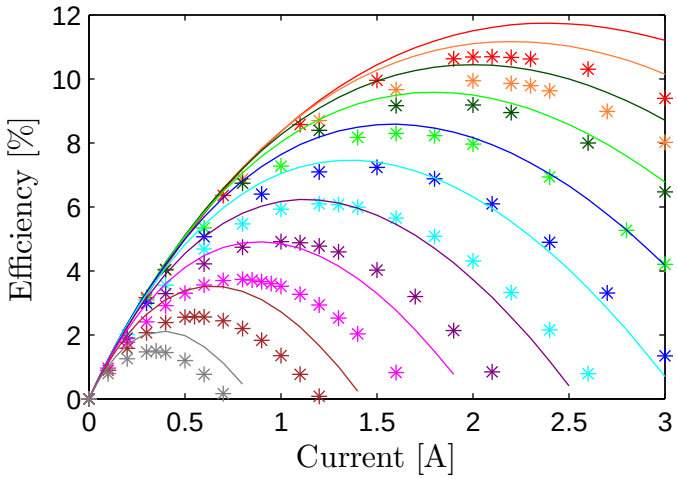

Figure 2-30: Segmented TEG efficiency vs. current curves. The simulations shown (solid lines) are for a leg emittance of 0.5 with no radiation shields. The measured points are shown as asterisks. The different colors represent hot-side temperatures ranging from 550 °C (top, red) down to 100 °C (bottom, gray) in 50 °C increments.

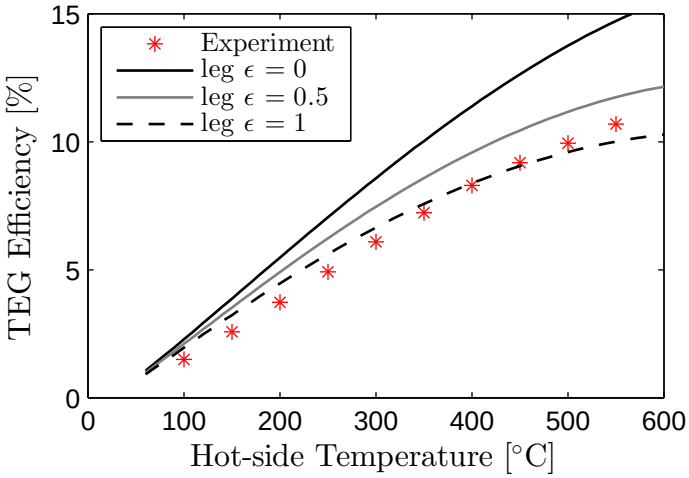

Figure 2-31: Segmented TEG device efficiency. The highest efficiency measured was 10.7% at a hot side of 550 °C and a cold side of 25 °C. The results are lower than predicted by the model.

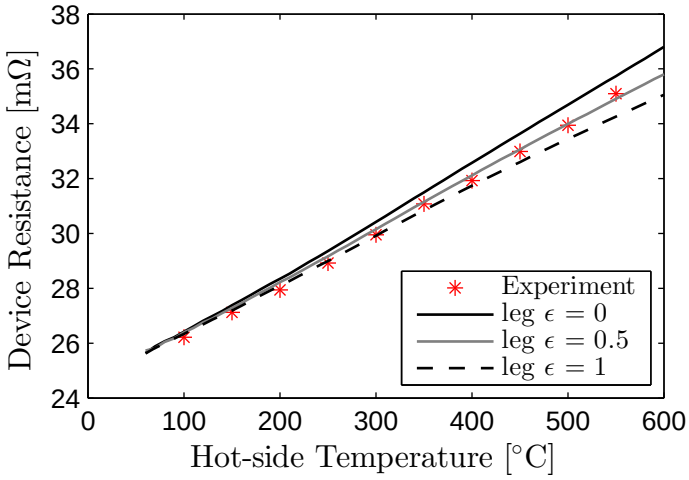

Figure 2-32: Segmented TEG device resistance, measured at the open-circuit condition. The simulations show little sensitivity to the effective leg radiation due to the constituent materials' small change in electrical resistivity with temperature.

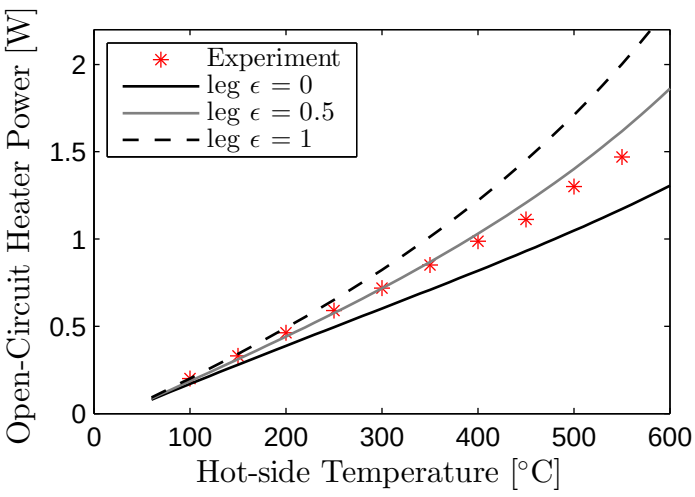

Figure 2-33: Segmented TEG heater power at the open-circuit condition. As expected, the experimental data fall between the $\epsilon = 0$ and $\epsilon = 0.5$ cases.

contact resistance between the heater and the top of the TEG. Contact resistance there would cause the hot junction of the TEG to experience a lower temperature than the thermocouple measures at the heater. A lower temperature would result in a lower Seebeck voltage.

Fortunately, the Peltier effect allows us to differentiate these causes. Due to the Peltier effect, as the current through the TEG increases, the heat flux into the TEG increases. This higher heat flux as a function of current can be seen by plotting the heater power as a function of the TEG current for various temperatures (Fig. 2-35). The heat flux can increase by as much as 50% at the highest currents. A larger heat flux would produce a larger temperature drop between the heater and the hot junction of the TEG. We do not directly measure the temperature of the hot junction, but we can evaluate whether or not it changes by reconstructing the Seebeck voltage at each current setpoint. At any current setpoint, the voltage measured is the Seebeck voltage less the resistive drop due to the current flow: $V_{teg} = V_s - IR$. Since the resistance is measured with an alternating DC technique at every current setpoint, the Seebeck voltage is calculated and shown in figure 2-36 for a range of currents and heater temperatures. Also shown in figure 2-36 is a dashed line indicating the predicted Seebeck voltage if the right amount of contact resistance is added to match the open-

circuit voltage. The Seebeck voltage is nearly constant at all currents, signifying that contact resistance is not the problem. The leg samples we are using may have lower Seebeck coefficients than the thermoelectric samples made for property measurements because the leg samples are hot pressed together with the contact electrodes. The high electrical and thermal conductivity of the contact electrodes could be reshaping the current and heating distribution within the DC hot press, which could lead to slightly different properties.

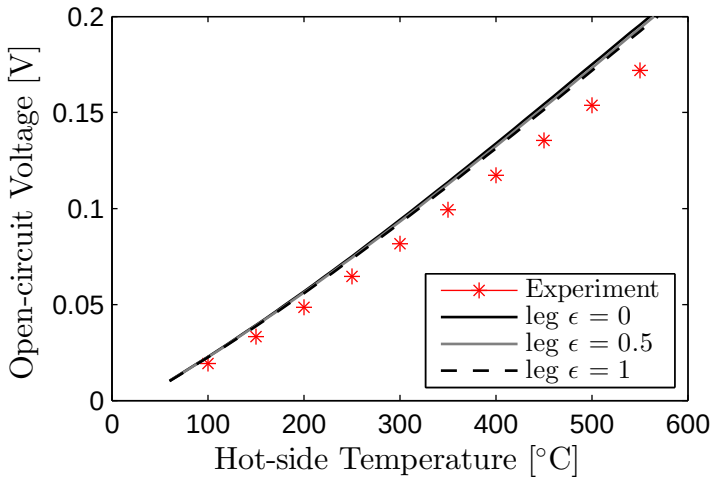

Figure 2-34: Segmented TEG open-circuit voltage. The simulations show little sensitivity to the effective leg radiation.

When the models are correted for a 12% lower Seebeck voltage, there is much better agreement with the experiment(Fig. 2-37).

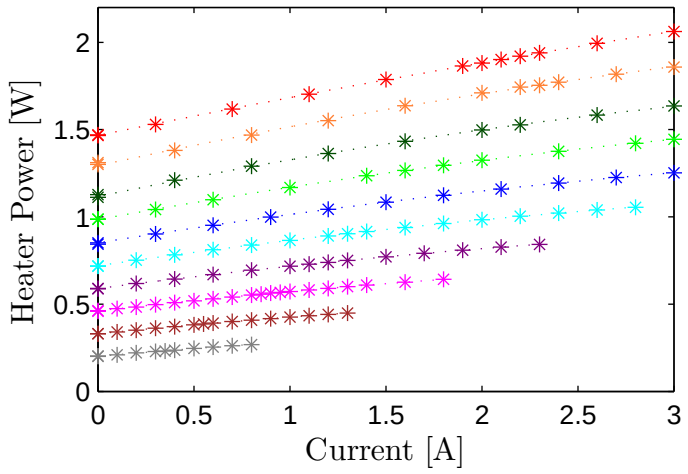

Figure 2-35: Heater power required to maintain the heater temperature as a function of current through the TEG, for heater temperatures of 550 °C (top, red) down to 100 °C (bottom, gray) in 50 °C increments. The increase with TEG current is due to the Peltier effect at the TEG hot junction.

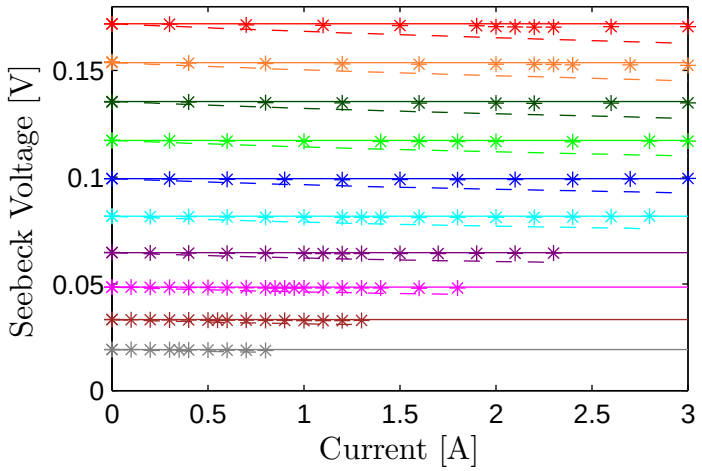

Figure 2-36: The measured Seebeck voltage (asterisks) for heater temperatures of 550 °C (top, red) down to 100 °C (bottom, gray) in 50 °C increments. Solid lines show constant Seebeck voltage. The Seebeck voltage is nearly independent of TEG current at each hot-side temperature. The predicted Seebeck voltage for a system with contact resistance (dashed line) does not match the trend of the experiments.

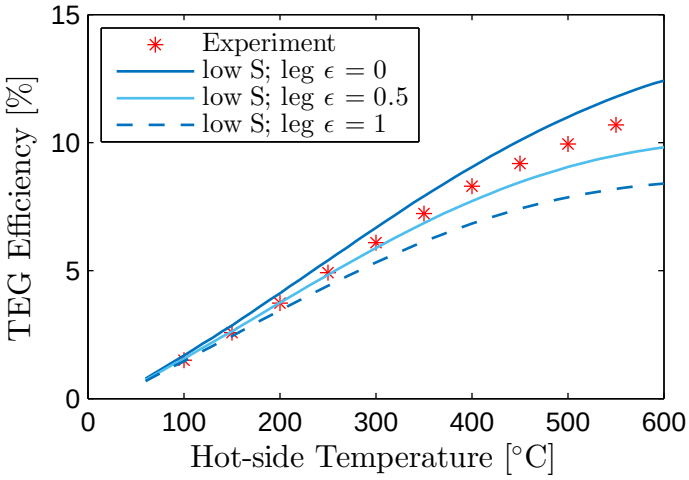

Figure 2-37: Segmented TEG efficiency. The cold side is at 25 °C. The models, adjusted to have a 12% lower Seebeck voltage, show good agreement with the experiment.

2.4 Conclusion

A model was developed to simulate the power conversion efficiency of a thermoelectric leg, including the effects of interfacial contact resistance, contact electrode segments, and radiation losses with and without a radiation shield. The model can be used to optimize the geometry of individual segmented thermoelectric legs. Results of a p-type and n-type leg can be combined to simulate a thermoelectric generator. Given the materials and manufacturing capabilities of our collaborators at the University of Houston and the testing capabilities at MIT, a unicouple TEG was optimized. The generator was also assembled and tested. The experimental results were in good agreement with the model when the average Seebeck coefficient is lowered 12%. This demonstrated TEG is the core of the high-temperature, high-concentration STEGs developed in the next chapter.

Chapter 3

Concentrating Solar Segmented Thermoelectric Generators

A concentrating solar thermoelectric generator (STEG) takes sunlight, concentrates it using focusing mirrors or lenses, and converts it into heat via absorption at the receiver. The heat is conducted to the thermoelectric generator (TEG), which converts a portion of the heat into electricity. The TEG rejects waste heat to the environment at its cold junction. This chapter describes system-level STEG modeling, and presents the testing of a STEG and its subsystems.

3.1 Basic System-level Model

A schematic of a STEG is presented in figure 3-1. Solar energy is intercepted by the optical system. The area of sunlight intercepted is the aperture area, A_{ap}. The average solar irradiation per unit area across the aperture is the aperture flux, H_{ap}. The total sunlight intercepted is the product of the flux and the irradiation: $Q_{ap} = H_{ap}A_{ap}$. The intercepted flux is concentrated by the optics onto the absorber, which has an area A_{abs}. To be clear with terminology, the absorber is not just the selective surface; it includes the substrate, as well as any other parts required to deliver heat to the TEG, such as any interface materials or heat spreaders. Sometimes the word receiver is used in place of the word absorber; per ASTM E772-11[70], the receiver also includes

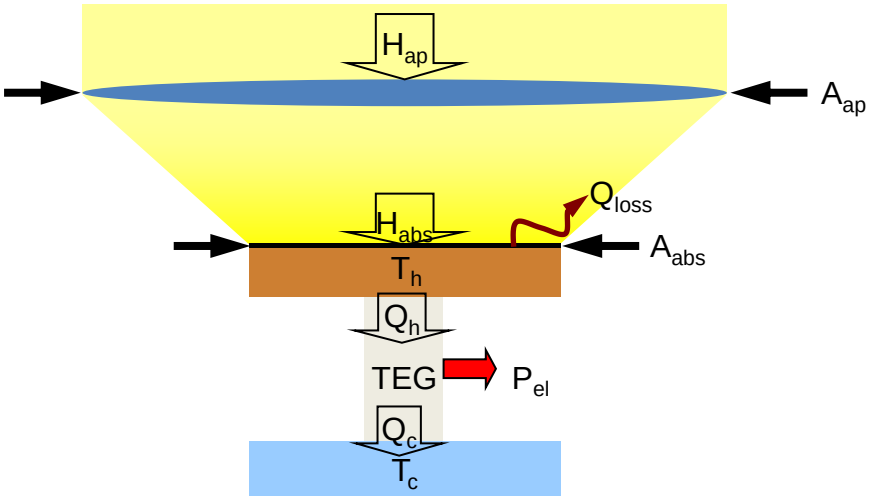

Figure 3-1: STEG schematic.

any glazings which cover the absorbing surface. Since in this STEG system we do not have any glazings between the absorber and the optics, the receiver and the absorber are the same.

The ratio of the aperture area to the absorber area is the geometric concentration ratio, C_g (Eq. (3.1)).

$$C_g = \frac{A_{ap}}{A_{abs}} \tag{3.1}$$

The average solar irradiation at the absorber, H_{abs}, is less than the product of the geometric concentration ratio and the aperture flux due to losses in the optics. These losses are typically reflection and absorption losses in the lenses or mirrors, and spillage losses. Spillage is light that passes through the lens, but does not fall onto the receiver. This can be the result of tracking inaccuracies, misalignment, aberration, or imperfections in the optics such as imperfect curvature or surface roughness. The fraction of the intercepted sunlight which reaches the absorber is the optical efficiency, η_{opt}:

$$\eta_{opt} = \frac{Q_{abs}}{Q_{ap}} = \frac{H_{abs} A_{abs}}{H_{ap} A_{ap}} \tag{3.2}$$

The solar flux that is incident on the absorbing surface is either absorbed or

reflected. The absorbed light is converted into heat, some of which is lost through radiation, convection, or conduction. The heat that is not lost via these mechanisms is delivered to the hot side of the TEG, where it can be converted into electricity. When the STEG is tested in vacuum there will be no convection losses, and there should be no conduction losses because only the TEG should be in contact with the absorber. This leaves just radiation as the loss mechanism. Radiation losses happen off of the front, back, and edges of the absorber. At larger scales, the edge area should be small with respect to the front and back surface areas, so the edge losses can be neglected. The radiation losses off of the front and back surfaces can be calculated with Planck's Law. With these assumptions we can calculate the absorber efficiency, η_{abs}, which is defined as the fraction of the incident flux at the absorber which is converted into heat and delivered to the TEG. There are no transmission losses in this equation as we are just looking at the absorber, not the whole receiver or system including the optics, and are normalizing to the light incident upon the absorber surface.

$$\eta_{abs} = \frac{Q_h}{Q_{abs}} = \frac{\alpha_{ss} A_{abs} H_{abs} - \sigma_{sb} \epsilon_{ss} A_{abs} \left(T_h^4 - T_{amb}^4\right) - \sigma_{sb} \epsilon_b A_b \left(T_h^4 - T_{amb}^4\right)}{A_{abs} H_{abs}} \tag{3.3}$$

where Q_h is the heat delivered to the TEG at a temperature T_h, α_{ss} is the absorptance of the absorbing surface, ϵ_{ss} is the emittance of the absorbing surface, σ_{sb} is the Stefan-Boltzmann constant, T_{amb} is the ambient temperature, ϵ_b is the emittance of the back side of the absorber, and A_b is the area of the back side of the absorber. The absorbing surface is typically some type of spectrally-selective surface which has a high absorptance in the solar spectrum and a low emittance in the infrared. If we assume that the back side of the absorber is approximately equal to the front side of the absorber, equation (3.3) can be simplified as shown in equation (3.4). The assumptions made in this simple absorber model, namely that there are no conduction losses, that the edge losses can be neglected, that the absorber is uniform in temperature, and that the back side radiation losses can be defined by the front-side

area and a single emittance, will be examined in detail and modified in the following subsystem-specific sections of this chapter.

$$\eta_{abs} = \alpha_{ss} - (\epsilon_{ss} + \epsilon_b) \frac{\sigma_{sb} (T_h^4 - T_{amb}^4)}{H_{abs}} \tag{3.4}$$

In equation (3.4), the fraction which multiplies the emittance sum is a function of the operating temperature, the ambient temperature, and the absorber insolation. These three variables are specific to the design point of the system, and can be lumped into the weighting factor, w, so that the absorber efficiency is simply calculated as $\eta_{abs} = \alpha_{ss} - w(\epsilon_{ss} + \epsilon_b)$. The weighting factor is plotted as a function of hot-side temperature and incident flux in figure 3-2. In low-temperature, low-concentration applications (such as domestic hot water systems), the weighting factor is relatively high, meaning that the emittance is as important as the absorptance in determining the absorber efficiency. In high-concentration applications, the weighting factor is low, signifying that the absorptance is more important than the emittance for high absorber efficiency.

$$w = \frac{\sigma_{sb} (T_h^4 - T_{amb}^4)}{H_{abs}} \tag{3.5}$$

Once heat is delivered from the absorber to the TEG, the TEG converts some of it into efficiency. As defined in Chapter 2, the TEG efficiency is the ratio of the electrical power produced to the heat flux into the TEG. This efficiency can be expressed as the product of the Carnot efficiency and a fraction which is dependent on the effective thermoelectric figure of merit, ZT_{eff}, of the material.

$$\eta_{teg} = \frac{P_{el}}{Q_h} = \frac{T_h - T_c}{T_h} \frac{\sqrt{1 + ZT_{eff}} - 1}{\sqrt{1 + ZT_{eff}} - T_c/T_h} \tag{3.6}$$

In the case of a TEG with no parasitic losses, and materials with temperature-independent properties, this effective figure of merit is the average over the temperature gradient of the figure of merit of the material:

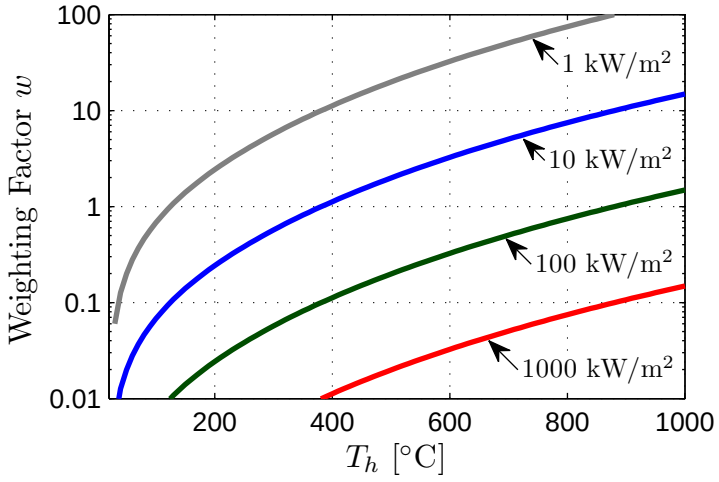

Figure 3-2: The weighting factor as a function of hot-side temperature and incident flux. The weighting factor is the relative importance of emittance vs. absorptance in absorbers with only radiative losses. A low weighting factor means that the absorber efficiency is mostly determined by its absorptance.

$$ZT_{eff} = \int_{T_c}^{T_h} zT \, dT \tag{3.7}$$

For the TEGs in this thesis, the efficiency of the TEG will be calculated and measured by the methods outlined in Chapter 2. However, for the conceptual model being developed in this introductory section, equation (3.6) will be used.

The overall efficiency of the STEG, defined as the ratio of the electrical power produced to the solar power intercepted, is the product of the optical, absorber, and TEG efficiency:

$$\eta_{steg} = \frac{P_{el}}{Q_{ap}} = \frac{Q_{abs}}{Q_{ap}} \frac{Q_h}{Q_{abs}} \frac{P_{el}}{Q_h} = \eta_{opt} \eta_{abs} \eta_{teg} \tag{3.8}$$

The optical efficiency is assumed to be independent of temperature. For a fixed optical concentration, the absorber efficiency decreases with increasing hot-side temperature. In contrast, the efficiency of a thermoelectric generator increases with increasing hot-side temperature. The product of these efficiencies has an optimal hot-side temperature for a given system. Assuming a TEG with an effective ZT of 1, a cold side of 50 °C, a front-side emittance which increases linearly from 0.05 at

100 °C to 0.24 at 700 °C, a back-side emittance of 0.05, an absorptance of 0.92, and an optical efficiency of 0.8 (or 0.9 for systems without concentrating optics), the efficiency vs. hot-side temperature graphs for a non-concentrating STEG and a STEG with a geometric concentration ratio of 100 are shown in figure 3-3.

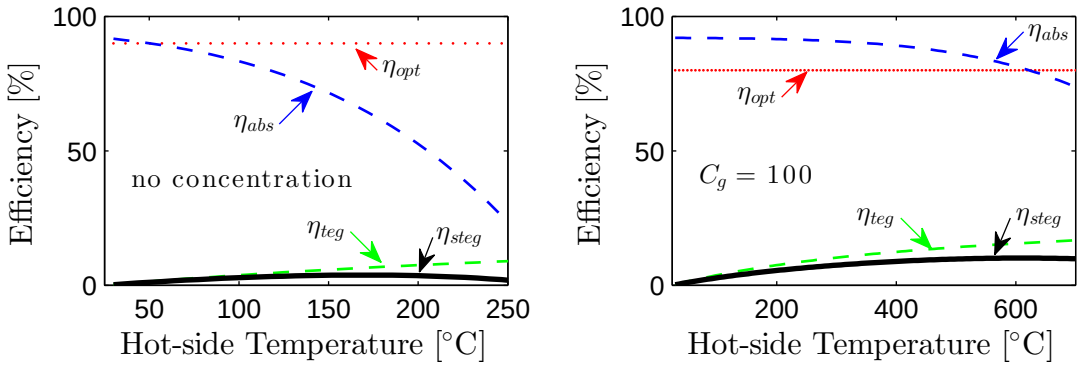

Figure 3-3: STEG and subsystem efficiencies for a STEG without concentrating optics (left) and a STEG with a geometric concentration ratio of 100 (right). The STEG efficiency (solid black) is the product of the optical efficiency (dashed red), the absorber efficiency (dashed blue), and the TEG efficiency (dashed green). The maximum efficiency of concentrating STEGs can exceed that of STEGs without concentrating optics.

It is clear from these figures that the optimal hot-side temperature is a strong function of optical concentration, and that higher concentrations and higher temperatures can result in higher STEG efficiencies. This is the motivation for developing concentrating STEGs which can take advantage of our TEGs which can operate up to 600 °C. In the following sections, the development of STEG optical systems and absorbers will be described. Advanced models will be used which will incorporate more of the details of these systems. A full STEG will be tested, and the results of the experiments will be compared to a full-system model.

3.2 Optical System

The design of the optical system is based on the requirements and capabilities of the TEGs. The TEGs can operate up to 600 °C, which would require an absorber

insolation in the range of $80\,\mathrm{kW\,m^{-2}}$. At these temperatures, the TEG should be operated under vacuum to eliminate convective losses and to prevent oxidation. The optical setup is shown in figure 3-4. The solar simulator shines a beam of light through the optical port in the vacuum chamber. The beam is redirected downward off of the mirror, where it is focused by the lens and directed to the absorber of the STEG.

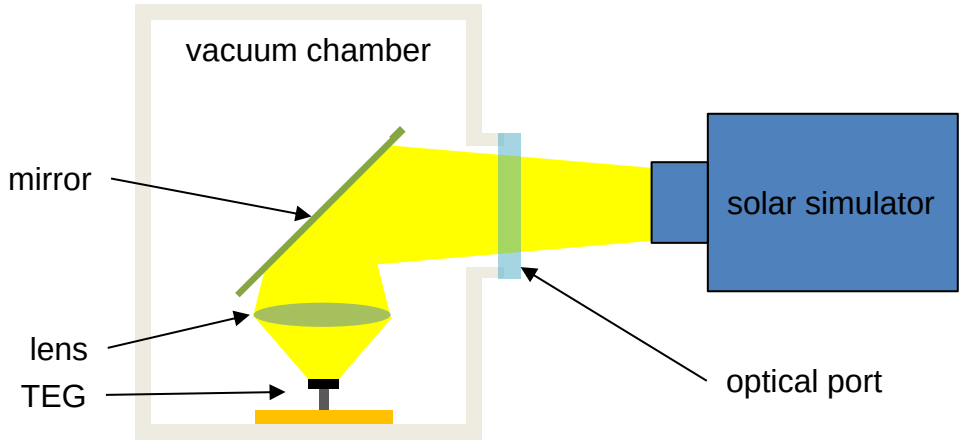

Figure 3-4: The STEG is placed inside a vacuum chamber. The solar simulator shines light through the optical port into the vacuum chamber, where it bounces off a mirror and is focused by a lens onto the STEG absorber.

From the optimization and experiments in Chapter 2, the built TEG needs to be supplied with approximately 2 W of power to reach 550 °C. If we assume the product of the optical efficiency will conservatively be 0.5, then we will need a lens which intercepts 4 W of solar flux. Given that the solar simulator produces an intensity of approximately $1000\,\mathrm{W\,m^{-2}}$ at its nominal settings, this requires a lens of at least 7 cm in diameter. The lens we chose to test (Thorlabs LA1740) has a 75 mm diameter and a back focal length of 69 mm. This may not produce high enough fluxes when the solar simulator is at its nominal distance and power, but we can easily double the intensity provided by the solar simulator by changing these two variables.

The lens itself is uncoated N-BK7 glass, which has a flat spectral response and should not alter the solar spectrum dramatically (Fig. 3-5). The AM1.5G-weighted normal incidence transmission for a 10 mm slab of N-BK7 is 0.92. Despite the fact that the lens varies in thickness from 3 to 24 mm, we would expect the transmission to be close to 0.9, since over most of the solar spectrum the losses in the lens are

due to reflection instead of absorption. It is difficult to measure the lens transmission directly, since the lens is larger than the power meter and therefore we cannot get a total incident power measurement on the lens. The smaller power meter must also be placed farther behind the lens, which means that any reduction in power could be due either to a transmission loss or to a spillage loss.

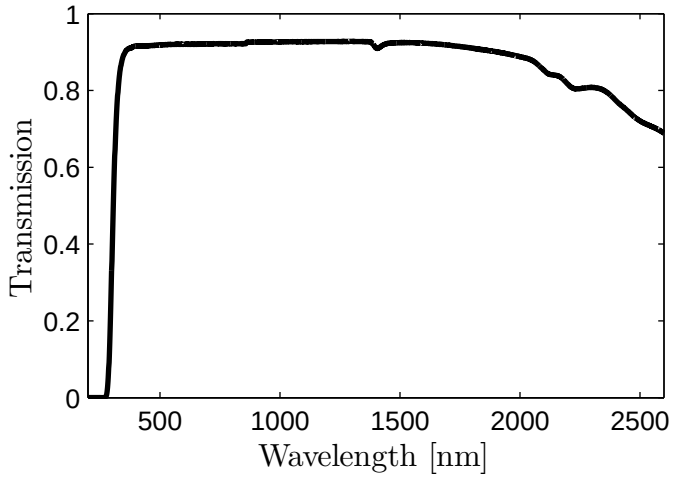

Figure 3-5: Transmission of a 10 mm thick BK7 glass slab. Data from Thorlabs. The total transmission weighted with the AM1.5G spectrum is 0.917.

To characterize the spillage from the lens, we place the 55 mm aperture behind the lens, at a position where the aperture does not block the concentrated beam from the lens. We also place an 80 mm aperture immediately in front of the lens to prevent light from the solar simulator passing around the lens and going to the power meter (Fig. 3-6). We measure the power behind the back aperture as the post-lens power. We then move the power meter lower, and place a variable-diameter iris between the back aperture and the power meter. The iris aperture is set at 7.1 mm diameter, and the iris distance behind the lens is varied. At each position, the power through the iris is measured with the power meter. This allows us to find the iris location where the solar flux is most concentrated, which should correspond to the focal plane. In this case, the focal plane is 67 mm behind the back (planar) face of the lens.

Next, the iris is placed at the focal plane. The power through the iris is measured as a function of iris diameter. The power is normalized to the post-lens power to

get the complement of the spillage of the optical system. This post-lens focusing efficiency is plotted in figure 3-7. In the ideal optical system, the spillage complement should proportional to the square of the iris diameter until it reaches the image size, after which it should be 1. In this tested system, the amount of light through the iris increases slowly with iris diameter, signifying that the system is not sharply focused. This is not surprising, as the nonuniformity of the focused spot is visible to the (safety-protected) eye. It is also clear in the average insolation data, where smaller spots have a higher concentration of light. These power and spillage data will be used in the following section to calculate the optimal absorber size.

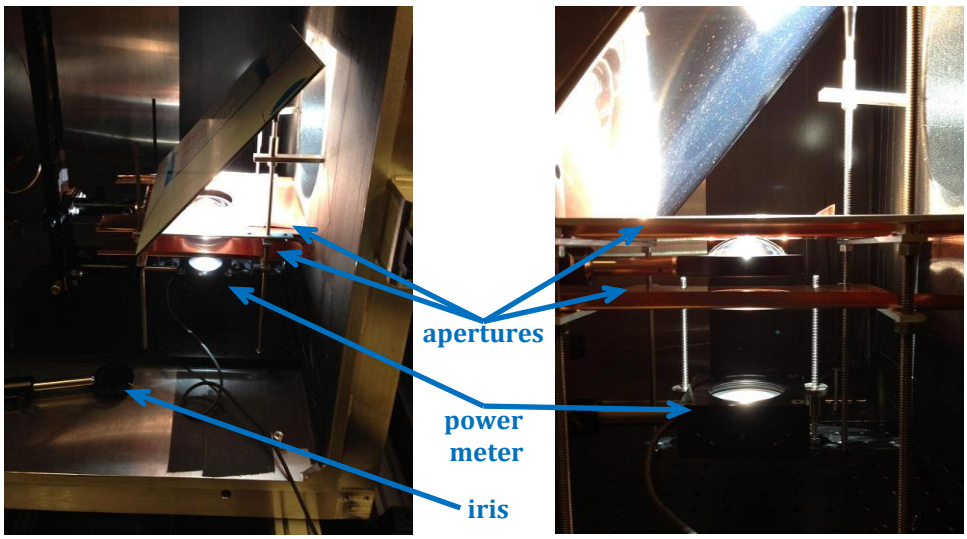

Figure 3-6: An 80 mm machine-polished copper aperture is placed in front of the 75 mm diameter lens. Behind the lens is a 55 mm aperture. The power meter and iris can be mounted on a vertical sliding rail.

3.3 Absorber

With air convection and conduction suppressed in the vacuum chamber, the only parasitic losses from the absorber are radiative. The absorbers used in this project are cermet-based selective surfaces deposited on 304 stainless steel substrates. The back sides of the absorbers are coated with a layer of tungsten to reduce the back-side emittance. The total hemispherical emittance of the selective surface as a function of

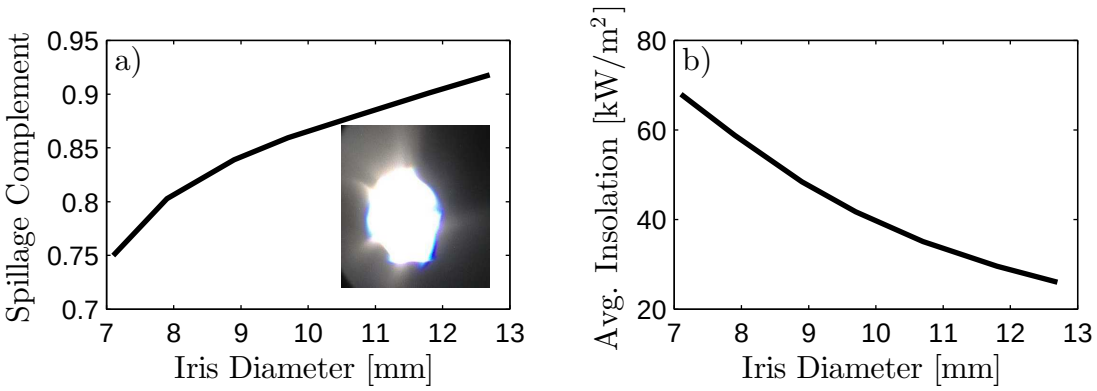

Figure 3-7: (a) The fraction of post-lens power that passes through a given diameter. (inset) The spot produced by the simulator and lens is not uniform. (b) The average insolation through the iris as a function of iris diameter.

temperature has been measured by Kraemer et al. on larger samples[69]; the data are reproduced in figure 3-8. They have also measured the near-normal solar absorptance of these surfaces to be 0.915. The emittance of the tungsten coating on the back side of the absorber has been measured by Chen et al.; it increases from 0.024 at room temperature to 0.11 at 1000 K[71](Fig. 3-8). The edge of the absorber is not coated, so the stainless steel substrate is exposed. The absorbers are too thin to measure the edge emittance directly, but 304 stainless steel can have an emittance exceeding 0.5, especially since the edges are not particularly smooth.

With these emittance values, the thermal losses from an absorber, Q_{rad}, can be calculated as a function of temperature (Eq. (3.9)). The thermal loss can be subtracted from the absorbed incident power values to attain the receiver efficiency as a function of temperature (Eq. (3.10)).

$$Q_{rad} = \left(\epsilon_{ss}\pi D_{abs}^2/4 + \epsilon_b\left(\pi D_{abs}^2/4 - A_{teg}\right) + \epsilon_{edge}\pi D_{abs}t\right)\sigma_{sb}\left(T_h^4 - T_{amb}^4\right) \tag{3.9}$$

$$\eta_{rec} = \frac{\alpha_{ss}H_{abs}\pi D_{abs}^2/4 - Q_{rad}}{H_{abs}\pi D_{abs}^2/4} \tag{3.10}$$

where D_{abs} is the absorber diameter, t is the absorber thickness, α_{ss} is the absorptance

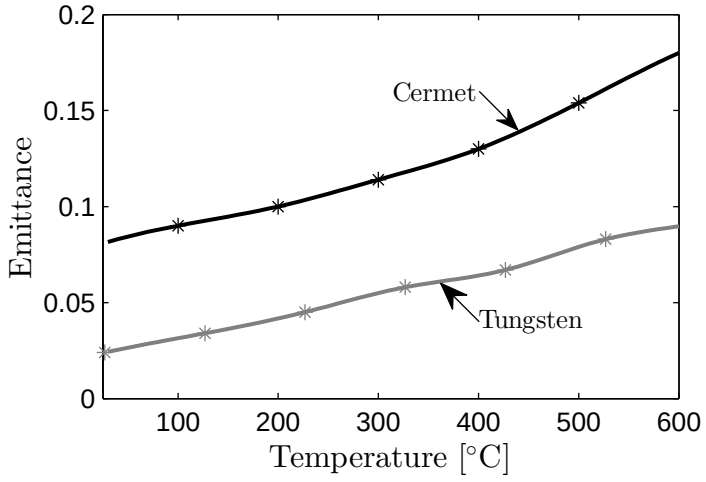

Figure 3-8: The total hemispherical emittance of (black) the cermet-based selective surface and (gray) tungsten, measured at elevated temperatures. Asterisks are data from [69] and [71]; lines are splined fits.

of the selective surface, ϵ_{ss} is the emittance of the selective surface, ϵ_b is the emittance of the tungsten back surface, and ϵ_{edge} is the emittance of the edge of the absorber. A_{teg} is the end cross-sectional area of the TEG which attaches to the back side of the absorber, and H_{abs} is the incident solar flux on the absorber (from Fig. 3-7). For a given incident flux, the hot-side temperature of the STEG is determined by performing an energy balance on the absorber (Eq. (3.11)). This requires knowing the hot-side heat flux through the TEG, Q_h, as a function of temperature. This heat flux is known from the modeling and experiments done described in Chapter 2.

$$0 = \alpha_{ss} H_{abs} \pi D_{abs}^2/4 - Q_{rad} - Q_h \tag{3.11}$$

The insolation from figure 3-7 was measured with the solar simulator at its nominal power setting. By adding dimming screens in front of the solar simulator or by increasing the power setting on the simulator, the insolation can be reduced to as low as 10% of the nominal power, or increased to 200% of the nominal power. This allows us to change the concentration on the absorber without needing to change the lens. The predictions for hot-side temperature, receiver efficiency, and STEG efficiency are plotted as a function of the average absorber insolation for various absorber diameters

in figures 3-9 through 3-11. It is assumed that the lens transmission is 0.9. The STEG efficiency is low, reaching a maximum predicted efficiency of only 6.2% with a 8.9 mm diameter absorber at an average absorber flux of 56 kW m^{-2}.

The optical system is a major source of loss, as the optical system efficiency is very low, mostly due to the spillage and transmission losses inflated by the large divergence of the solar simulator and the small scale of the system. Such large spillage also changes the optimal performance point, suggesting that it is better to use larger absorbers than would otherwise be optimal if better optics were used. And although it is useful to report the overall system efficiency including optical losses, many thermal systems report their efficiencies based on the absorber flux, not the aperture flux. The predictions for this STEG's efficiency based on the absorber flux are that it should reach an efficiency of 8.9% with a 7.1 mm diameter absorber at an absorber insolation of 84 kW m^{-2} (Fig. 3-11(b)).

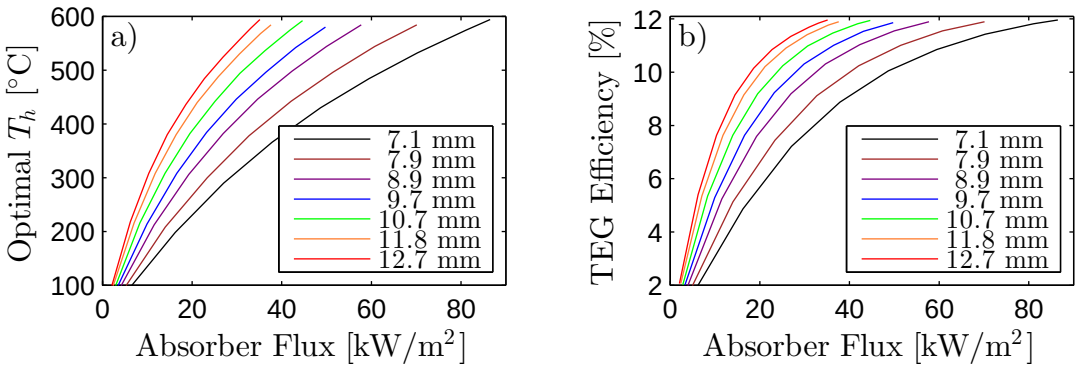

Figure 3-9: Predicted (a) hot-side temperature as a function of absorber flux. The TEG efficiency (b) is a function of the STEG's operating hot-side temperature.

3.4 STEG Testing

When testing a TEG, the skutterudite legs (with contacts) are brazed directly to a heater block to ensure good thermal contact. When testing a STEG, the legs must be attached directly to the absorber. For the first STEG tests, the legs were brazed to a 0.3 mm thick copper connection plate just large enough to accommodate both

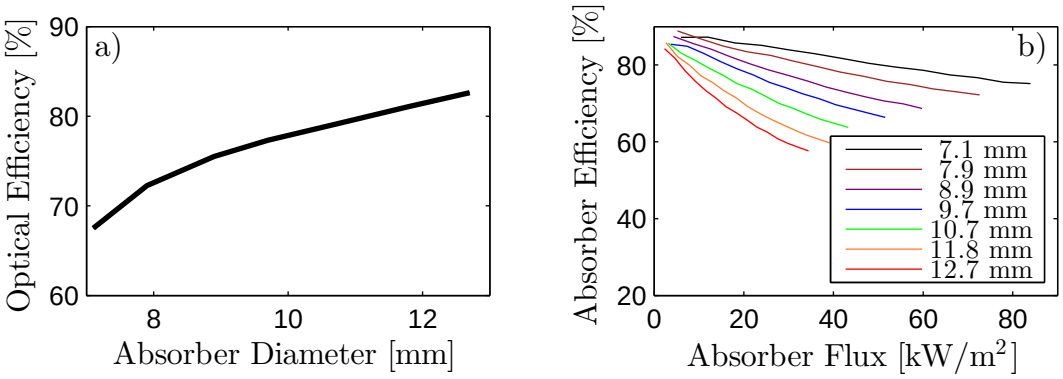

Figure 3-10: (a) The STEG optical efficiency is independent of temperature, and is only a function of the absorber diameter. (b) The absorber efficiency is a function of the absorber flux.

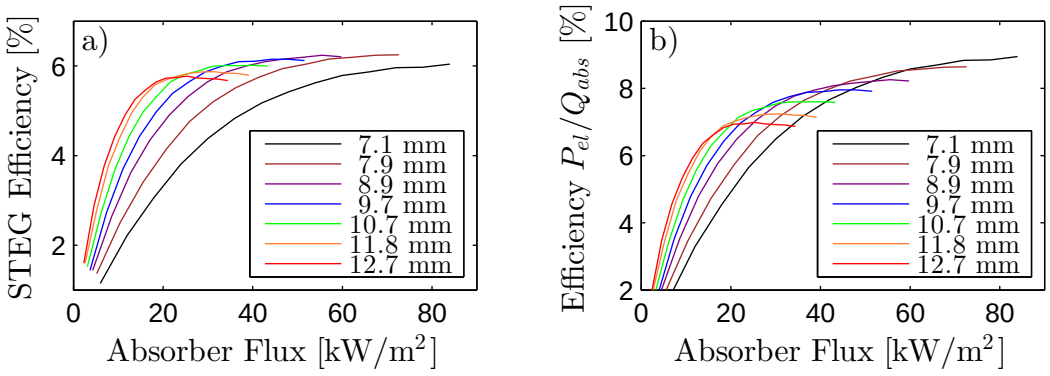

Figure 3-11: The STEG efficiency based on the (a) aperture flux and (b) absorber flux.

legs. After that, the bismuth telluride legs, cold junctions, and radiation shields were attached in the same manner described in chapter 2 for assembling TEGs. The unicouple was then attached to the cold stage developed for TEG testing. The mirror and lens remained in place in the vacuum chamber from the optics testing, but the power meter and iris were removed. The cold stage was positioned such that the top of the unicouple was located at the same position the iris aperture had occupied. A stainless steel absorber was then attached with liquid metal (75.5% Ga, 24.5% In) to the copper connector plate at the top of the unicouple. Small (on the order of a few millimeters) adjustments in the horizontal plane of the lens and aperture were made in order to have the solar spot centered on the absorber. The STEG in its testing configuration is shown in figure 3-12.

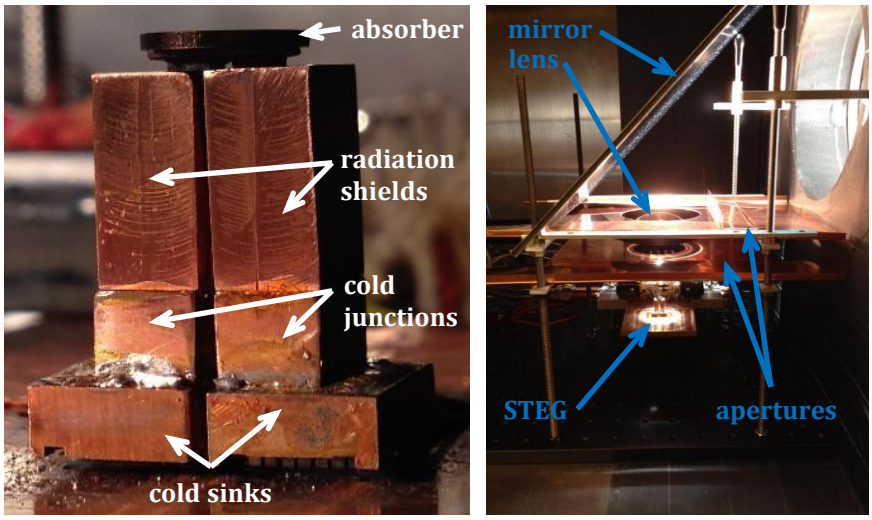

Figure 3-12: Photographs of the STEG ready to be tested. The STEG is mounted to a cold stage inside the vacuum chamber. The lens directs the solar beam downward through the lens to the STEG. Machine-polished copper apertures prevent solar radiation which does not pass through the lens from reaching the STEG.

The absorber was chosen to be 8 mm in diameter, as the 7.9 mm absorber had the highest predicted STEG efficiency of all the measured iris diameters, and the STEG efficiency based on the absorber flux was only 0.22% lower than the 7.1 mm diameter at a much lower absorber flux (66 $\mathrm{kW\,m^{-2}}$ instead of 84 $\mathrm{kW\,m^{-2}}$). The STEG was tested at cold sides of 25 °C and 50 °C at absorber fluxes between 6 and 72 $\mathrm{kW\,m^{-2}}$. At each flux, the system was brought to thermal equilibrium. Since the hot-side

temperature was not measured, the stability of the voltage generated by the STEG was used as a proxy for thermal equilibrium. When the did not vary by more than 30 µV over 30 seconds, the system was deemed to be in thermal equilibrium and data would be recorded. Given that the effective Seebeck voltage of the unicouple is approximately 300 µV K^{-1}, this corresponds to a temperature stability within 0.1 °C. The mean STEG voltage and current were recorded over 30 seconds of thermal equilibrium. An alternating DC electrical resistance test was performed at the end of the voltage and current recording periods. The current was swept to 3 A or until the short-circuit current.

The maximum efficiency measured was 5.7% at 56 kW m^{-2}. This is the second-highest STEG efficiency ever measured. A detailed examination of the measured properties during the experiment gives additional insight into the performance of the device. First, the measured electrical resistance of the STEG matched simulations closely (3-13). The open-circuit voltage was within the expected range for low absorber fluxes, but at high fluxes it diverged from the main trend. This may be due to a thermal contact resistance developing at higher temperatures and fluxes as the liquid metal hardens, or it is due to the lower Seebeck coefficient as seen with the TEGs. The same trend is seen in the STEG efficiency based on the absorber flux (Fig. 3-15).

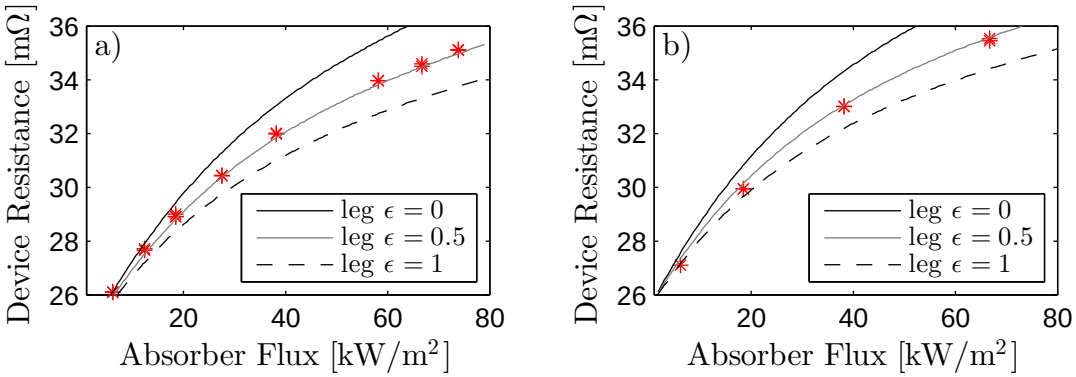

Figure 3-13: The resistance of the STEG as a function of absorber flux for (a) T_c=25 °C and (b) T_c=50 °C. The resistance lined up very well with the predictions with an effective leg emittance of 0.5.

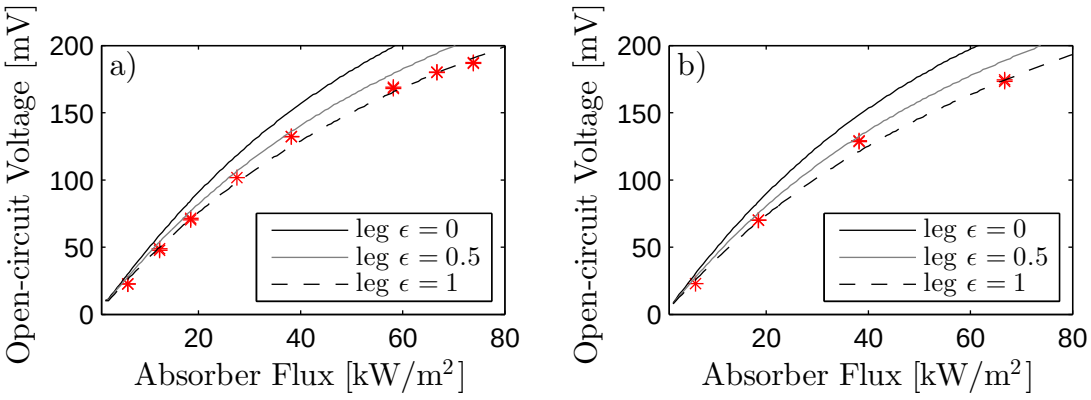

Figure 3-14: The open-circuit of the STEG as a function of absorber flux for (a) T_c=25 °C and (b) T_c=50 °C. The open-circuit voltage diverges from the trend of the simulations. This could be due to a low Seebeck coefficient, or a worsening of the thermal contact between the absorber and the top of the TEG.

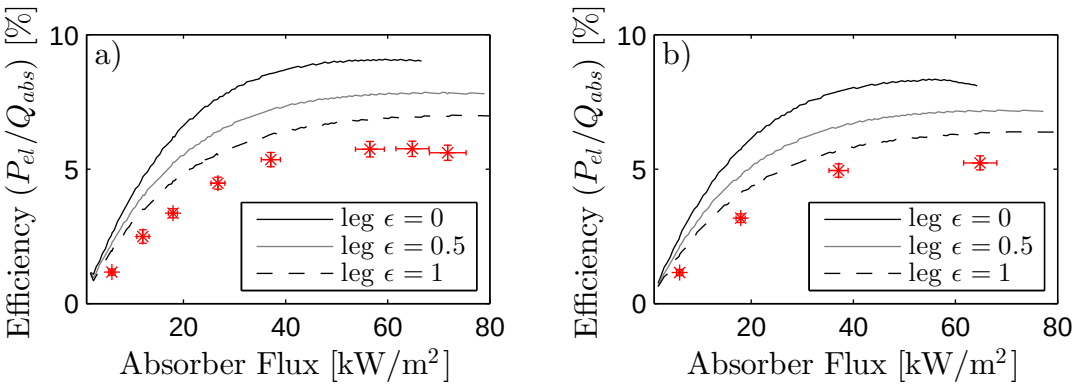

Figure 3-15: The STEG efficiency, based on the absorber flux, as a function of absorber flux for (a) T_c=25 °C and (b) T_c=50 °C. The efficiency is always lower than the simulations, but is the worst at highest fluxes. This could be due to a low Seebeck coefficient, or a worsening of the thermal contact between the absorber and the top of the TEG.

There are two additional potential causes for the lower STEG efficiency. The first is an alignment error. After the STEG is mounted, the optics must be shifted laterally so that the focused spot is as the center of the absorber. Given that the focused light does not create a clean spot and instead has blurry edges fading from the center, there is a chance that the spot is not centered on the absorber. If this happens, the total amount of light incident on the absorber will be smaller than if it were perfectly aligned. This discrepancy could be reducing the STEG efficiency at all incident fluxes. A second potential cause is the fouling of the backside of the absorber and the radiation shields, which we noticed upon disassembling the STEG. The most likely cause is the outgassing of residual flux that was not cleaned off of the brazed joints. Cleaning the brazed joints with deionized water, isopropanol, acetone, or heavy-duty flux remover could not prevent this problem. A fix for this problem may be to develop a vacuum-brazing technique that uses a different flux. The development of such a system would also allow direct brazing of the thermoelectric legs to the absorber, eliminating the copper header plate. That would reduce the radiation losses from the gap between the radiation shields and the back side of the absorber.

3.5 Conclusion

A STEG with an efficiency of 5.7% at $57\,\mathrm{kW\,m^{-2}}$ was modeled, built, and tested. Despite being the second-highest STEG efficiency ever measured, the STEG efficiency was still lower than predicted. Most likely, thermal losses from the absorber beyond what were predicted in the initial models are keeping the STEG efficiency low. In addition, the lower Seebeck coefficient seen in the TEG experiments is probably also negatively affecting the STEG performance. With new assembly procedures and new materials currently under development, we should be able to measure significantly higher STEG efficiencies in the near future.

Chapter 4

Aerogel-Based Solar Receivers

Aerogels are fascinating materials with a wide variety of applications. They can be highly thermally insulating while also being transparent to visible light. These properties allow aerogels to act like the glass in a greenhouse, allowing sunlight in and trapping the heat. This chapter investigates using aerogels in this capacity to improve the thermal efficiency of solar thermal heat collection. After a brief introduction to aerogels and solar receivers, the basic model will be described. The predicted performance of the aerogel receiver will then be compared to a traditional vacuum tube receiver. The chapter concludes with a discussion of the future of aerogel-based solar receivers.

4.1 Introduction to Aerogels

Aerogels are stable low-density foams which can be made from a variety of materials. Aerogels typically have densities on the order of 0.1 to 15% of the density of the solid constituent; the rest of the volume consists of tiny pores that either are gas-filled or are evacuated. Aerogels are produced by the sol-gel process, in which a solid is suspended in a liquid, and then the liquid is removed, leaving only the solid structure behind. If the liquid is removed via evaporation, the surface tension can cause the delicate solid structures to collapse. A breakthrough occurred in 1931, when Kistler showed that stable aerogels could be made by removing the liquid in a

supercritical process[72]. Shortly thereafter, Kistler further developed the fabrication technique and began characterizing a wide variety of aerogels, including measuring their thermal conductivities[73–75], which is on the order of $0.005\,\mathrm{W\,m^{-1}\,K^{-1}}$ for silica aerogels. Similar early work was performed by White[76]. Besides silica, aerogels have also been made from various materials including alumina [77,78], titania [79], borates [80,81], and organics [82,83].

While all of these aerogels exhibit low thermal conductivity, silica aerogels also have the interesting property that they are highly transparent to visible light but opaque in the infrared. This wavelength selectivity, noted from the very beginning by Kistler and White, is what makes silica aerogels potentially very useful in solar thermal receivers. The opacity of a medium can be characterized by its extinction coefficient, β, which determines how quickly the intensity decays as described by Beer's Law:

$$\frac{\mathrm{d}I}{\mathrm{d}x} = -\beta I \tag{4.1}$$

where I is the intensity of radiation in a given direction and x is the coordinate in that direction. The extinction within a medium can be due to both scattering and absorption by the medium. The extinction coefficient is the sum of the scattering coefficient s and absorption coefficient a: $\beta = s + a$.

Various methods exist to measure the wavelength-dependent extinction of aerogels. The most basic technique is the direct transmission method. In this method, the intensity of a beam of light is measured. Then, the aerogel is placed into the beam, and the intensity is measured again. The detector typically has a small acceptance angle, so the measured reduction in intensity can be due to extinction in the bulk, or from scattering or reflections at the surfaces of the sample. By measuring samples of varying thicknesses, it is possible to correct for the surface effects, thus yielding just the bulk extinction. This measurement can be made across a wide range of wavelengths with UV-Visible and FT-IR (Fourier transform infrared) spectrophotometers.

When aerogels scatter radiation, some of the radiation will be scattered in di-

rections with a forward component. This forward-scattered light can be captured in the measurement along with the transmitted light using an integrating sphere, which is a device that attaches to the detector on a spectrophotometer and captures all the transmission through the sample, not just the straight-line transmission. This is called the direct-hemispherical transmission measurement, as opposed to the direct-direct transmission without the integrating sphere. The difference between the direct-hemispherical transmission and the direct-direct transmission is the foward-scattered light. Basic scattering calculations can correlate the quantity of forward-scattered light to the scattering coefficient, as will be explained later in this chapter.

Scattering in aerogels can also be measured directly using the same concept as a nephelometer. In this measurement, a beam of light (usually a laser) is incident on a sample. Behind the sample, a narrow-range detector is swept through space, measuring the spatial distribution of light coming out of the sample. This technique not only determines the scattering and absorption coefficients, it also determines the scattering phase function, which is a measure of the spatial distribution of the scattered light. While this technique sounds ideal, it is a difficult, highly specialized measurement and is not commonly used. The vast majority of papers on aerogel radiative properties report the extinction measured with UV-Vis and FT-IR spectrophotometers.

Absorption within a silica aerogel can come from the bulk silica; from the gas in the aerogel if it is not evacuated; from precursor residues left in the aerogel; from surface states of the silica; and from any additional dopants. The measured extinction of silica aerogels normalized to the density of the aerogels, which is called the specific extinction and has units of $\mathrm{m^2\,kg^{-1}}$, elucidates the absorption mechanism. These data are plotted in figure 4-1. At wavelengths longer than 2 µm the specific extinction of these samples, ranging from 100 to 220 $\mathrm{kg\,m^{-3}}$, appears to be independent of density. Measurements by Heinemann et al. on samples ranging from 5 to 220 $\mathrm{kg\,m^{-3}}$ show the same density independence, with some variation at wavelengths less than 2 µm or more than 30 µm[84]. The long-wavelength deviations are not that important, since even at room temperature only 11% of the blackbody spectrum is beyond 30 µm. At wavelengths greated than 4 µm the specific extinction is essentially the same as

the specific extinction of fused silica. This aerogel density correlation, as well as agreement with fused silica data, strongly suggests that the nature of the extinction is bulk absorption. The major deviations occur below 5 µm, where absorbed water has a large effect on the absorption coefficient[85–87]. Enough water can be absorbed from the air in 24 hours to produce an order of magnitude change in the absorption coefficient[88, 89]. Absorption from 2 µm to 4 µm can also be attributed to SiO, OH, and SiOH[85] which are most likely found at the surface of silica particles. Residual precursors could also be a source of absorption[87, 90]. In the case of the data from Wei in figure 4-1, the authors attribute the additional extinction in the sub-5 µm range to water adsorbed to the silica[91].

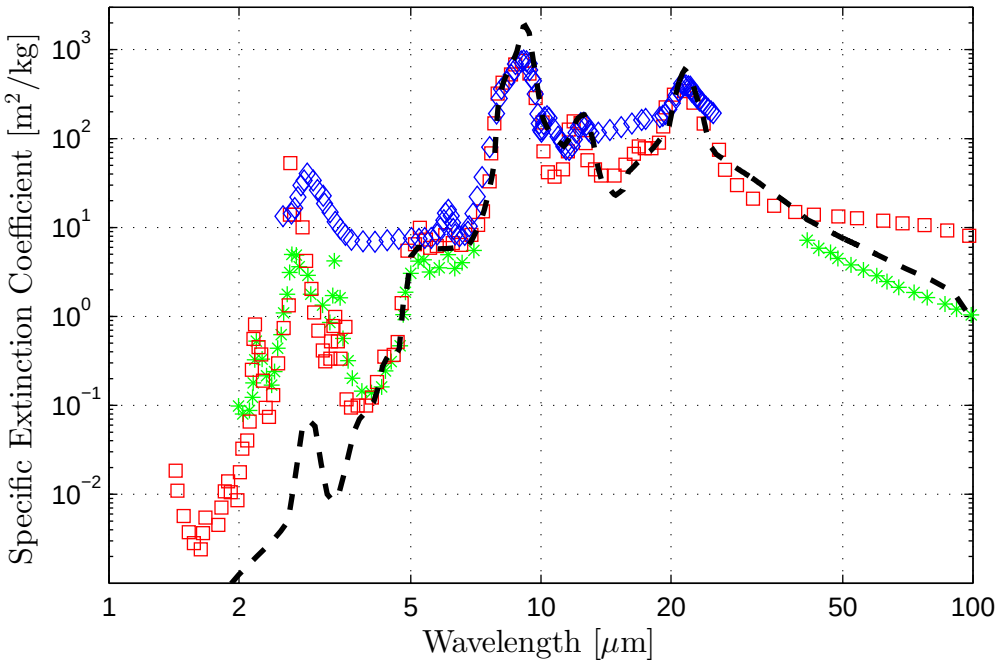

Figure 4-1: The specific extinction coefficient of updoped silica aerogels as a function of wavelength. Measured aerogel data from Hartmann et al. for approximately 140 kg m^{-3} (green asterisks)[89], Heinemann et al. for 70 kg m^{-3} (red squares)[84], and Wei et al. for 83 to 185 kg m^{-3} (blue diamonds)[92]. Fused quartz data from Kitamura et al. (black dashed line)[93].

At wavelengths less than 1 µm, there is almost no absorption of light in silica. Therefore all extinction at these wavelengths is due to scattering of the aerogel, or from absorption of surface states, residues, or gases in the structure. The wavelength-

dependent extinction shows no signature absorption bands, but instead shows the trend expected with Rayleigh scattering, where the scattering coefficient is proportional to the inverse fourth power of the wavelength. The extinction of aerogels in the sub-1 µm range is shown in figure 4-2. In these aerogels, the characteristic scattering length is representative of the pores in the aerogel[94], and thus the magnitude of scattering is dependent on the structure of the aerogel, which is a function of the manufacturing process[87,90,95–102]. The supposition that the extinction in the visible wavelengths is entirely due to scattering and not absorption is supported by the fact that three samples with the same density show different extinctions, as seen in figure 4-2.

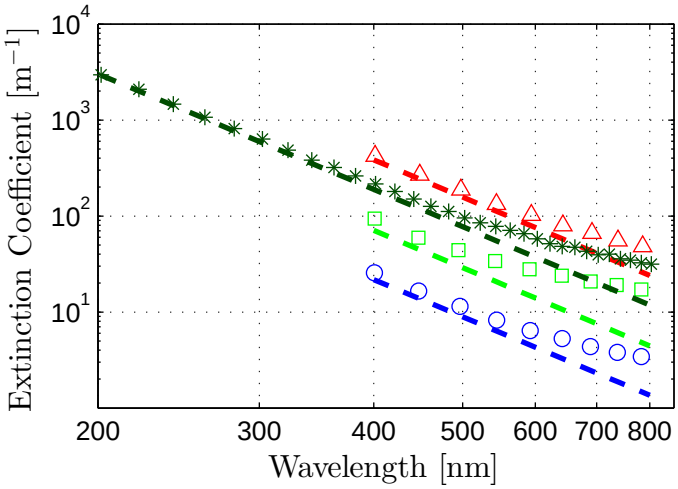

Figure 4-2: The extinction coefficient of updoped silica aerogels as a function of wavelength. Measured data (including surface and bulk scattering) from Emmerling et al. for 230 kg m^{-3} aerogels (green asterisks)[103]; three samples from Beck et al. for 80 kg m^{-3} aerogels from three precursors with different pH values: pH=9 (red triangles), pH=11 (green squares), and pH=13 (blue circles)[96]. Dashed lines are the fitted bulk Rayleigh scattering for each sample, which exclude the surface scattering effects.

The probability of light of wavelength λ being scattered from one solid angle Ω into another solid angle Ω' is described by the scattering phase function, $\Phi_{\lambda,\Omega\to\Omega'}$. By convention, the integral of the scattering phase function over all outgoing angles is 4π:

$$4\pi = \int_{4\pi} \Phi_{\lambda,\Omega\to\Omega'}\, \mathrm{d}\Omega' \tag{4.2}$$

The scattering phase function is a strongly affected by the type of scattering; the scattering phase function for Rayleigh scattering is nearly symmetric forward and backward, and the variation as a function of polar angle is small[104]. Aerogels have been shown to have nearly isotropic scattering, i.e. the phase function is 1 in all directions[103, 105–107]. The hemispherical transmission of a slab of scattering material is nearly the same whether an isotropic or Rayleigh scattering phase function is used[108], and therefore we treat aerogels as isotropic scatterers to greatly simplify the calculations in the following section.

4.2 Aerogel-based Solar Receivers

In any solar thermal system, such as domestic hot water systems, solar air conditioning systems, solar thermoelectric generators, or concentrating solar power (CSP) systems based on parabolic troughs, parabolic dishes, linear Fresnel lenses, or heliostat fields, the energy of the solar radiation must be converted into heat. The portion of the solar thermal system which receives the concentrated or unconcentrated sunlight and absorbs it is called the receiver. The ideal receiver would absorb all of the sunlight and lose none of the heat to the environment. This is thermodynamically impossible, so a receiver efficiency, η_{rec}, is introduced, defined as the fraction of the solar flux incident on the receiver which is delivered as heat to the working system and not lost:

$$\eta_{rec} = \frac{Q_h}{H_{rec} A_{rec}} \tag{4.3}$$

where Q_h is the heat delivered to the working system by the receiver, H_{rec} is the average solar irradiation (in $\mathrm{W\,m^{-2}}$) incident on the receiver, and A_{rec} is the area of the receiver. The solar irradiation can be larger than the standard AM1.5G value of $1000\,\mathrm{W\,m^{-2}}$ if concentrating optics are used. In order to absorb as much of the

sunlight as possible, receivers typically have an absorber that is black in the solar spectrum. To prevent heat losses to the environment, all hot surfaces including the absorbing surface typically have low emittance in the infrared. Various strategies can be used to prevent convective heat losses off of the hot surfaces as well.

Aerogels could potentially be used in solar receivers to prevent heat losses from the absorbing surface, presenting an alternative to what is typically used today. In the two most common solar receivers - flat-panel (air gap) absorbers and evacuated tubes - a layer of glass acts as a cover for the absorber surface. Between the absorber and the glass is either air or a vacuum. For air-gap solar receivers, the glass serves as a protective layer that also is a barrier to convective and radiative heat transfer, reducing heat loss while still transmitting most of the visible light similar to the greenhouse effect (Fig. 4-3(a)). For vacuum gap receivers, the glass is the protective covering as well as the outer structural wall enclosing the vacuum gap. In this case the vacuum gap eliminates convective losses, and the glass reduces the radiative losses without adding a large visible transmission loss (Fig. 4-3(b)). In an aerogel-based solar receiver, the air or vacuum gap is replaced with an aerogel layer (Fig. 4-3(c)).

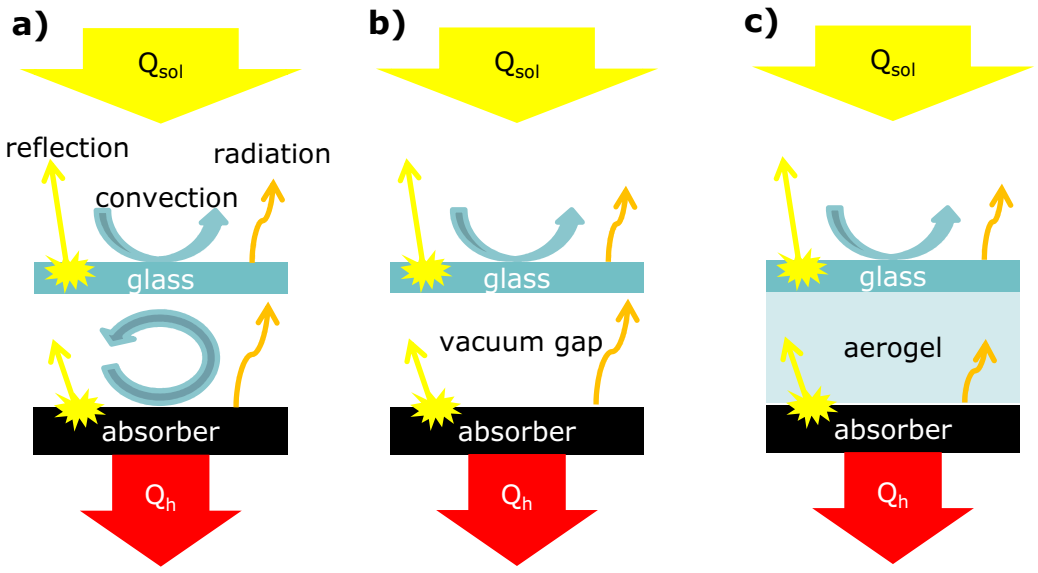

Figure 4-3: Schematic of three types of solar thermal receivers: (a) air gap, (b) vacuum gap, and (c) aerogel-based. A more efficient receiver converts more of the sunlight, Q_{sol}, into heat delivered to the system Q_h.

The concept of using aerogels for solar thermal applications is not new, but nearly all the work has focused on space heating. Papers in the 1980s investigated the possibility of replacing windows with aerogel tiles[85, 87, 89, 95, 99, 109], and it is now possible to buy such windows from Cabot, one of the largest aerogel manufacturers. Similarly, it was proposed to use aerogels in Trombe walls, which are essentially thin transparent panels outside the sun-facing exterior walls of a house which serve as a greenhouse shell[110, 111]. Now such systems have been demonstrated on existing houses[112]. Only a few papers have examined aerogels for solar thermal receivers[113, 114]; the results from tests in the range of 60 °C to 80 °C look promising when compared to flat-panel receivers with an air gap[114]. The next step is to use models to predict if aerogels can improve the performance of even higher temperature solar receivers compared to state-of-the-art evacuated tube collectors.

4.3 Modeling Heat Transfer within Aerogels

Heat transfer within an aerogel occurs via three methods: solid conduction, gaseous conduction, and radiation. Solid conduction is the heat transferred via conduction through the solid fraction of the aerogel. For silica aerogels, the solid conduction is usually very small, on the order of $0.004\,\mathrm{W\,m^{-1}\,K^{-1}}$[113]. Gaseous conduction across the pores varies from zero for evacuated aerogels to $0.02\,\mathrm{W\,m^{-1}\,K^{-1}}$ or more in silica aerogels; the gaseous conductivity is thus a strong function of the system pressure[74, 75, 84, 92, 115–120]. The third mode of heat transfer, radiation between and through the aerogel, can be the dominant method of heat transfer if the aerogel is sufficiently transparent to the thermal radiation, as will be discussed throughout this chapter. The transparency is a function of the aerogel wavelength-dependent specific properties, the density of the aerogel, the characteristic temperature of the radiation at the boundaries, and the temperature distribution within the aerogel.

Simulations of the thermal performance of an aerogel must treat in parallel the three modes of heat transfer outlined above. While the solid conductance and gaseous thermal conductance are frequently lumped together as one conductance, the radiative

heat transfer must be treated as an additional conductance in parallel[121]. This coupling can be modeled in a variety of ways. If the sample is optically dense for all the wavelengths of radiation present, the Rosseland diffusion approximation (4.4) can be used to calculate a radiative thermal conductivity, k_{rad}, which can be added in parallel to the solid and gaseous conductivities[122].

$$k_{rad} = \frac{16\sigma_{sb}T^3}{3\beta} \tag{4.4}$$

For materials such as silica aerogels the Rosseland diffusion approximation is not always a safe approximation, so more rigorous methods are often used. Most of these methods rely on solving the Equation of Radiative Transfer (ERT) and coupling it to the heat equation. These methods treat the wavelength-dependence of the aerogel properties by dividing the radiative spectrum into numerous finite bands, and calculating in parallel the radiative transfer in each band. Marques et al. treated the aerogel as nonscattering, and solved the resulting integro-differential equation[123]. Nordgaard and Beckman used a modified ERT, called the F-hat method, to treat the wavelength-dependent scattering and absorption[113]. Heinemann et al. used a multi-band ERT to treat the scattering and radiation[84].

In this thesis, the performance of the aerogels will be calculated with a band model coupling the ERT to the heat equation, similar to that of Heinemann. We assume the problem is one-dimensional, so we discretize the spectral intensity in position z and in angle θ (Fig. 4-4). The geometry is assumed to be planar, so Cartesian coordinates are used. The boundary conditions of a hot surface (bottom) and a layer of glass with convective cooling and an incident solar flux (top) are added to both the ERT and the heat equation. The details are outlined in the following subsections, using material properties taken from literature as an example. It will be shown that aerogels in fact have a much larger realm of potential applications than has been shown before. In particular, aerogel-based receivers could be useful for a wide range of high-temperature solar thermal systems.

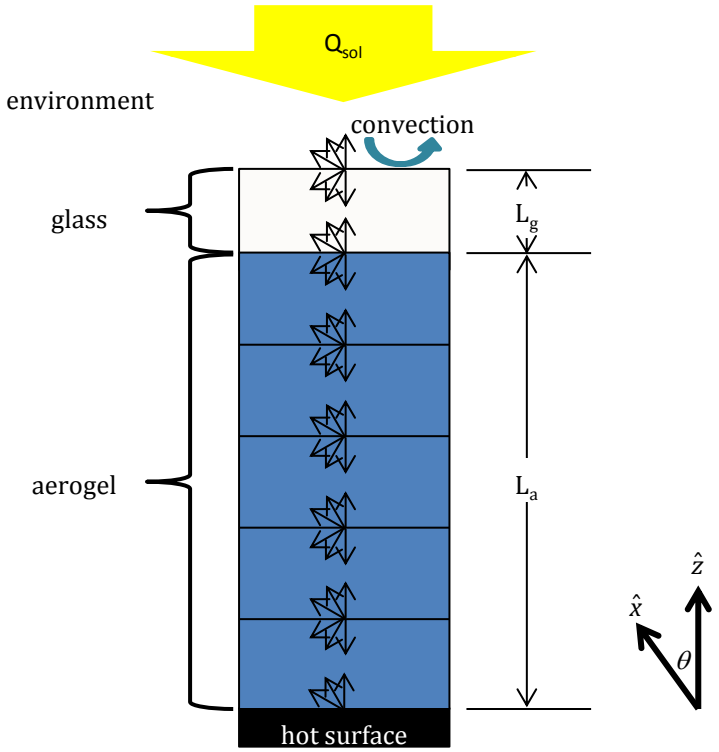

Figure 4-4: One-dimensional discretization for the equation of radiative transfer. $\hat{z}$ is the direction normal to the surface; $\hat{x}$ is the direction along the path of a given ray. θ is the angle between $\hat{x}$ and $\hat{z}$.

4.3.1 Equation of Radiative Transfer

The equation of radiative transfer states that the intensity of a specific wavelength of radiation within a given solid angle in a medium can be reduced by absorption, reduced by scattering to other directions, increased by thermal emission, and increased through scattering from other directions into the direction of interest[104]:

$$\frac{\mathrm{d}I_{\lambda\Omega'}}{\mathrm{d}x_{\Omega'}} = -(s_\lambda + a_\lambda)I_{\lambda\Omega'} + a_\lambda I_{b\lambda} + \frac{s_\lambda}{4\pi}\int_{4\pi} \Phi_{\lambda,\Omega\to\Omega'} I_\Omega \,\mathrm{d}\Omega \tag{4.5}$$

Here $I_{\lambda\Omega'}$ is the intensity for a given wavelength λ in a given solid angle Ω'; x is the distance along the direction of the solid angle; s_λ is the scattering coefficient; a_λ is the absorption coefficient; $I_{b\lambda}$ is the blackbody intensity for a given wavelength, which is a function of the local temperature; and $\Phi_{\lambda,\Omega\to\Omega'}$ is the scattering phase function from solid angle Ω into solid angle Ω'. In the gray approximation, the scattering and absorption coefficients and scattering phase function are assumed to be independent of wavelength. For silica aerogels, the absorption and scattering coefficients are strong functions of wavelength, and thus the ERT must be solved over distinct wavelength bands where these properties are assumed to be constant.

To discretize the ERT, we first replace the wavelength-dependent properties with the properties of each band, indexed with the subscript k. All radiation will be classified by the sign of the z-component of the direction as either positive-traveling radiation I^+ or negative-traveling radiation I^-. The solid angle is discretized by polar angle θ, and it is assumed that the intensity of radiation is uniform across the discretized solid angle. The first solid angle extends from a polar angle of $\theta_0 = 0$ to θ_1, the second from θ_1 to θ_2, up until the nth solid angle θ_{n-1} to $\theta_n = \pi/2$. These solid angles are reflected into the $-z$ direction. The extent of each discretized solid angle is a weighting function w and can be calculated using the equation for the area of a solid angle as:

$$w_j = 2\pi \int_{\theta_{j-1}}^{\theta_j} \sin\theta \, d\theta = 2\pi \left(\cos\theta_{j-1} - \cos\theta_j\right) \tag{4.6}$$

The absolute value of the z-component of the direction of the radiation in the solid angle, μ, can be calculated as:

$$\mu_j = \frac{1}{w_j} 2\pi \int_{\theta_{j-1}}^{\theta_j} \sin\theta \cos\theta \, d\theta = \frac{\pi}{w_j} \left(\sin^2 \theta_j - \sin^2 \theta_{j-1} \right) \tag{4.7}$$

The discretization of the z-direction requires a little bookkeeping. The intensity of radiation is kept track of at each plane bounding a differential slice of aerogel. It is indexed in space starting with the $i = 1$ plane just inside the aerogel at the hot surface. The antepenultimate plane is just inside the aerogel at the aerogel-glass interface. The penultimate plane is actually in the middle of the glass. The last plane is in the air, just above the surface of the glass. The temperature profile is kept track of at slightly different coordinates. The temperatures in the temperature matrix represent the average temperature within a differential slice of aerogel. The exceptions are the first temperature, which is the temperature of the hot surface; the penultimate temperature, which is at the aerogel-glass interface; and the last temperature, which is the temperature of the surface of the glass exposed to the air. With this we can fully discretize the ERT.

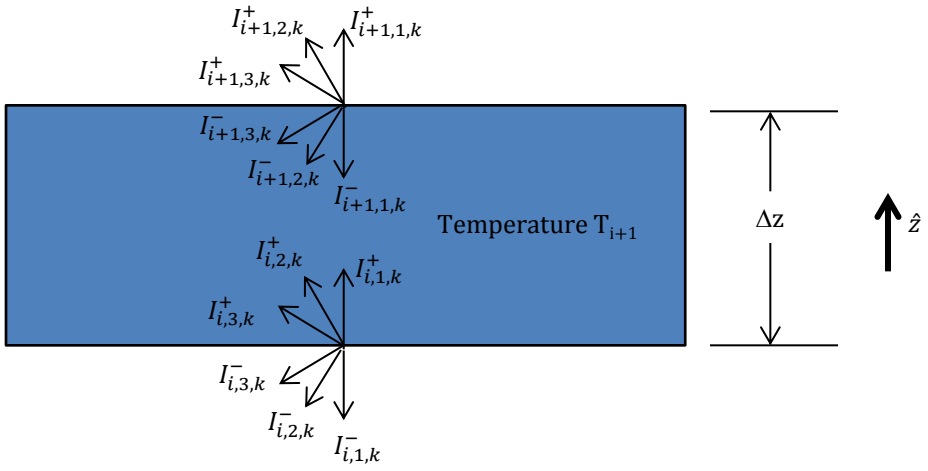

Figure 4-5: The intensity within the aerogel is discretized at planes separated by a spacing of Δz. The intensity is also discretized in a number of solid angles (three shown in schematic) and bands.

For any slice of aerogel of thickness Δz, we can calculate the change in intensity

of forward-going radiation I^+. A schematic of the slice is presented in figure 4-5. The path length within a slice for solid angle j is $\Delta x = \Delta z/\mu_j$: The forward-going radiation is diminished by absorption and scattering within the slice. It is augmented by radiation from within the slice, and also by any scattering that happens to occur within the slice. The amount of radiation in the blackbody spectrum in band k from λ_{k-1} to λ_k is calculated from Planck's blackbody radiation function:

$$I_{b:k}(T) = \int_{\lambda_{k-1}}^{\lambda_k} \frac{2hc_0^2}{n^2\lambda^5\left[e^{hc_0/n\lambda k_b T} - 1\right]}\, d\lambda \tag{4.8}$$

where h is Planck's constant, c_0 is the speed of light in a vacuum, n is the index of refraction of the medium, k_b is Boltzmann's constant, and T is the absolute temperature.

$$I^+_{i+1,j,k} = I^+_{i,j,k} + \frac{\Delta z}{\mu_j}\left(-\left(s_k + a_k\right) I^+_{i,j,k} + a_k I_{b:k}(T_{i+1}) + \frac{s_k}{4\pi}\sum_{J=1:n_j}\left(I^+_{i,J,k} + I^-_{i+1,J,k}\right) w_J\right) \tag{4.9}$$

Note that as was discussed in section 4.1, the phase function for aerogels can be assumed to be 1. At the hot boundary, the radiation in the positive z-direction the sum of the emittance and the specular and diffuse reflection:

$$I^+_{1,j,k} = \epsilon_{h:k} I_{b:k}(T_1) + (1-\epsilon_{h:k}) p_k I^-_{1,j,k} + \frac{1}{2\pi}\sum_{J\neq j}\left((1-\epsilon_{h:k})(1-p_k) I^-_{1,J,k} w_J\right) \tag{4.10}$$

where $T_1 = T_h$ is the temperature of the hot surface, $\epsilon_{h:k}$ is the emittance of the hot surface over band k, and p_k is the specularity parameter for that band.

The last three planes of radiation have their own sets of equations. This is done for two reasons. First, the ERT does not include Snell's Law; it must be calculated separately and added to the equations. Second, the glass, being at least an order of magnitude more dense than the aerogel, would require many discretized slices since each slice would need to be an order of magnitude thinner than the slices in aerogel - possibly even more slices than there are in the aerogel. There is no need to waste this

computational power on the glass; if we make the very safe assumption that there is no scattering in the glass, then the ERT just reduces to Beer's Law, which can be solved rapidly.

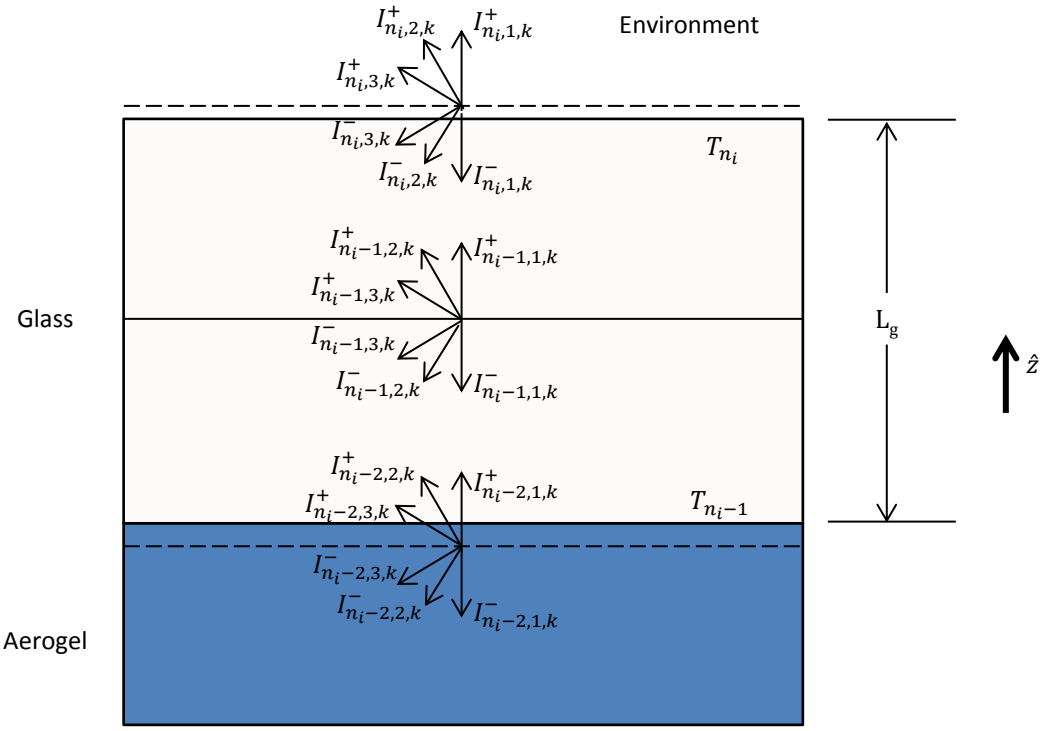

Figure 4-6: Schematic of the discretization of the radiation intensity near the glass. The last three planes of intensity must be solved separately than the planes in the rest of the aerogel.

The last three planes of radiation are depicted in figure 4-6. The positive-traveling intensities at the third-to-last plane are calculated in the same manner as the rest of the aerogel slices. The positive-traveling intensities in the penultimate plane are calculated according to the transmission of the glass:

$$I^+_{n_i-1,j,k} = T^+_{j,k} I^+_{n_i-2,j,k} \tag{4.11}$$

where $T^+_{j,k}$ is the transmission of the glass for incident rays from the aerogel in direction j in band k. The last positive-traveling intensities, as well as the antepenultimate and penultimate negative-traveling intensities, are similarly calculated. $R^-_{j,k}$ is the reflection of the glass for incident rays from the air in direction j in band k.

$$I^+_{n_i,j,k} = I^+_{n_i-1,j,k} + R^-_{j,k} I^-_{n_i,j,k} + \left(1 - R^-_{j,k} T^-_{j,k}\right) I_{b:k}(T_{n_i}) \tag{4.12}$$

$$I^-_{n_i-1,j,k} = T^-_{j,k} I^-_{n_i,j,k} \tag{4.13}$$

$$I^-_{n_i-2,j,k} = I^-_{n_i-1,j,k} + R^+_{j,k} I^+_{n_i-2,j,k} + \left(1 - R^+_{j,k} - T^+_{j,k}\right) I_{b:k}(T_{n_i-1}) \tag{4.14}$$

The boundary condition is the negative-traveling intensity in free space, which is the solar and ambient radiation incident on the surface of the glass.

$$I^-_{n_i,j,k} = I_{b:k}(T_{amb}) + I_{sol:j,k} \tag{4.15}$$

The incident solar radiation distribution in space is a function of the geometry of the concentrating optics; for low concentrations it may be all within the first discretized solid angle, in which case we have:

$$I_{sol:j,k} = \begin{cases} P_{sol:k}/w_j/\mu_j, & j = 1 \\ 0, & j \neq 1 \end{cases} \tag{4.16}$$

where $P_{sol:k}$ is the amount of solar flux within band k. It may be noticed that the penultimate slice is only serving to keep track of light transmitted through the aerogel; it is possible to incorporate equation (4.11) and equation (4.13) into equation (4.12) and equation (4.14). However, they do serve a purpose when coupled to the heat equation. Adding an extra radiation plane essentially deposits the energy of absorbed radiation within the half of the glass closest to where the radiation came from. Given that the absorption depth in the glass for much of the infrared is very short, this helps to localize that absorbed heat nearer to the appropriate surface as opposed to distributing it evenly throughout the glass.

The reflection and transmission coefficients in equations (4.11)–(4.14) are based on geometric ray tracing and Snell's Law. The positive-direction coefficients are not

necessarily equivalent to the negative-direction coefficients because the index of refraction of the aerogel is not the same as that of air. For a given direction, the three indices of refraction, N_1, N_2, and N_3 are determined (either aerogel/glass/air or air/glass/aerogel). The reflection at each interface is calculated with the Fresnel equations, averaging the p-polarized and s-polarized light. For example at the interface between the first two media:

$$R_{12} = \left(R_{12,s} + R_{12,p}\right)/2 \tag{4.17}$$

$$R_{12,s} = \left|\frac{N_1 \cos\theta_1 - N_2 \cos\theta_2}{N_1 \cos\theta_1 + N_2 \cos\theta_2}\right|^2 \tag{4.18}$$

$$R_{12,p} = \left|\frac{N_1 \cos\theta_2 - N_2 \cos\theta_1}{N_1 \cos\theta_2 + N_2 \cos\theta_1}\right|^2 \tag{4.19}$$

$$T_{12} = \left(T_{12,s} + T_{12,p}\right)/2 \tag{4.20}$$

$$t_s = \frac{2N_1 \cos\theta_1}{N_1 \cos\theta_1 + N_2 \cos\theta_2} \tag{4.21}$$

$$t_p = \frac{2N_1 \cos\theta_1}{N_2 \cos\theta_1 + N_1 \cos\theta_2} \tag{4.22}$$

$$T_{12,s} = \frac{\mathrm{Re}(N_2^* \cos\theta_2)}{\mathrm{Re}(N_1^* \cos\theta_1)} \left|t_s\right|^2 \tag{4.23}$$

$$T_{12,p} = \frac{\mathrm{Re}(N_2^* \cos\theta_2)}{\mathrm{Re}(N_1^* \cos\theta_1)} \left|t_p\right|^2 \tag{4.24}$$

Here θ_1 is the angle of the incident wave with respect to the interface normal, and θ_2 is the angle of the transmitted wave with respect to the interface normal. The same calculations are done for the second interface. Then geometric optics are used to calculate the transmittance of the two interfaces together:

$$b = \exp\left(-a_g L_g / \cos\theta_2\right) \tag{4.25}$$

$$R_{1-3} = R_{12} + \frac{T_{12}^2 R_{23} b^2}{1 - R_{12} R_{23} b^2} \tag{4.26}$$

$$T_{1-3} = \frac{T_{12}^2 T_{23} b}{1 - R_{12} R_{23} b^2} \tag{4.27}$$

Here a_g is the wavelength-dependent absorption coefficient of the glass and L_g is the thickness of the glass. These calculations are performed over a fine mesh of angles, and the results are averaged for each direction j and band k. The index of refraction of the glass is from the literature (Fig. 4-10)[93]. The index of refraction of the aerogel is density-dependent. The real part is calculated according to the density of the aerogel with respect to the density of glass[124]:

$$n_{aerogel} = 1 + (n_{glass} - 1)\frac{\rho_{aerogel}}{\rho_{glass}} \tag{4.28}$$

The imaginary part is calculated from the extinction coefficient:

$$\kappa = \frac{a_\lambda \lambda_0}{4\pi} \tag{4.29}$$

where λ_0 is the free-space wavelength of that frequency of radiation.

4.3.2 Coupling the ERT and Heat Equations

With the indicated boundary conditions, the radiation at each plane can be determined as long as the temperature profile within the aerogel and glass is known. However, the temperature profile is not known in advance; it must be solved using the heat equation with input from the ERT. Hence these two equations are coupled, and must be solved iteratively in parallel.

The steady-state heat equation can be discretized for any of the slices of glass or discretized aerogel as:

$$\rho c \Delta z \frac{dT}{dt} = 0 = (q_r + q_c)_z - (q_r + q_c)_{z+\Delta z} \tag{4.30}$$

where q_r is the net radiative flux and q_c is the heat flux via conduction and convection. The conductive and convective heat flux in the z-direction at any plane i is:

$$q_{c,i} = \begin{cases} -k_a \frac{T_2 - T_1}{\Delta z/2}, & i = 1 \\ -k_a \frac{T_{i+1} - T_i}{\Delta z}, & 1 < i < n_i - 2 \\ -k_a \frac{T_{n_i-1} - T_{n_i-2}}{\Delta z/2}, & i = n_i - 2 \\ -k_g \frac{T_{n_i} - T_{n_i-1}}{L_g}, & i = n_i - 1 \\ -h_{conv} \left(T_{amb} - T_{n_i}\right), & i = n_i \end{cases} \tag{4.31}$$

where k_a is the effective thermal conductivity of the aerogel including conduction in the solid chain and convection in the pores, k_g is the thermal conductivity of the glass, h_{conv} is the convective coefficient of the air at the surface of the glass, T_{amb} is the ambient air temperature.

The net radiative flux at any plane is the difference between the forward-traveling and backward-traveling radiative energies:

$$q_{r,i} = \sum_{K=1:n_k} \sum_{J=1:n_j} \left(I^+_{i,J,K} - I^-_{i,J,K}\right) w_J \mu_J \tag{4.32}$$

These equations can be implemented in matrix form to solve for the temperature profile with a given radiative solution. The a new radiative solution is formed from the new temperature profile; this process is repeated until the temperature profile converges.

$$A = \begin{bmatrix} 1 & 0 & 0 & 0 & \dots & 0 & 0 & 0 & 0 & 0 \\ 2\frac{k_a}{\Delta x} & -3\frac{k_a}{\Delta x} & \frac{k_a}{\Delta x} & 0 & \dots & 0 & 0 & 0 & 0 & 0 \\ 0 & \frac{k_a}{\Delta x} & -2\frac{k_a}{\Delta x} & \frac{k_a}{\Delta x} & \dots & 0 & 0 & 0 & 0 & 0 \\ \vdots & & & & \ddots & & & & & \vdots \\ 0 & 0 & 0 & 0 & \dots & \frac{k_a}{\Delta x} & -2\frac{k_a}{\Delta x} & \frac{k_a}{\Delta x} & 0 & 0 \\ 0 & 0 & 0 & 0 & \dots & 0 & \frac{k_a}{\Delta x} & -3\frac{k_a}{\Delta x} & 2\frac{k_a}{\Delta x} & 0 \\ 0 & 0 & 0 & 0 & \dots & 0 & 0 & 2\frac{k_a}{\Delta x} & -2\frac{k_a}{\Delta x} - \frac{k_g}{L_g} & \frac{k_g}{L_g} \\ 0 & 0 & 0 & 0 & \dots & 0 & 0 & 0 & \frac{k_g}{L_g} & -\frac{k_g}{L_g} - h_{conv} \end{bmatrix} \tag{4.33}$$

$$A \begin{bmatrix} T_1 \\ T_2 \\ T_3 \\ \vdots \\ T_{n_i} - 3 \\ T_{n_i} - 2 \\ T_{n_i} - 1 \\ T_{n_i} \end{bmatrix} = \begin{bmatrix} q_{r,2} - q_{r,1} \\ q_{r,3} - q_{r,2} \\ q_{r,4} - q_{r,3} \\ \vdots \\ q_{r,n_i-3} - q_{r,n_i-4} \\ q_{r,n_i-2} - q_{r,n_i-3} \\ q_{r,n_i-1} - q_{r,n_i-2} \\ q_{r,n_i} - q_{r,n_i-1} - h_{conv} T_{amb} \end{bmatrix} \tag{4.34}$$

4.3.3 Band Properties of Aerogels

Each spectral band can be broadly classified as either the infrared or the solar spectrum. In the infrared, the spectral bands can be chosen by eye; there are clear wavelength ranges where the absorption coefficient is nearly constant. Across each band, it is unknown whether there will be a larger intensity at some wavelengths than others, since the intensity will be a function of the local temperature and the boundary conditions. Therefore when averaging over the bands, the absorption coefficient of each wavelength will be weighted equally. The wavelengths within the band act as conductances in parallel; the conductance is approximately inversely proportional to the extinction coefficient (as is seen in the Rosseland diffusion approximation,

Eq. (4.4)), so the inverse of the absorption coeffients must be averaged (Eq. (4.35)). The IR data from Heinemann et al.[84] are averaged into bands using this method; the results are shown in figure 4-7. The bands span a range from 1.5 µm to 190 µm; this range captures more than 99.9% of the blackbody spectra for temperatures between 0 °C and 450 °C.

$$\frac{1}{a_{band}} = \int_{\lambda_1}^{\lambda_2} \frac{1}{a_\lambda}\, d\lambda \tag{4.35}$$

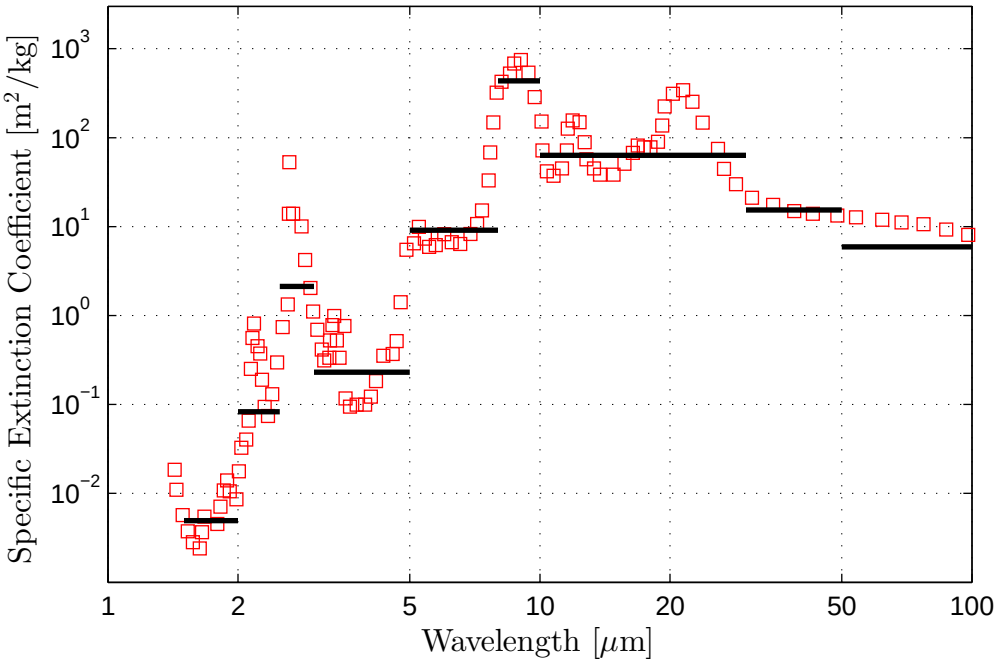

Figure 4-7: Extinction data from Heinemann et al.[84] are averaged into bands divided at 1.5, 2, 2.5, 3, 5, 8, 10, 30, 50, and 190 µm. Less than 0.1% of the 400 °C blackbody spectrum is at wavelengths shorter than 1.5 µm; less than 0.1% of the 25 °C blackbody spectrum is at wavelengths longer than 190 µm.

At wavelengths shorter than 1 µm, the clear trend is for the extinction to go as the inverse fourth power of the wavelength. This suggests that all the extinction is scattering. Without absorption and reemission, the transmission through a slab for a single wavelength of light is independent of what happens in other bands. The direct-hemispherical transmission for a slab of thickness L and scattering coefficient s can be

calculated as a function of the slab optical thickness, sL, using the ERT. This direct-hemispherical transmission is compared to the direct-direct transmission in figure 4-8. The direct-hemispherical transmission shows a nearly exponential decay with optical thickness. When the direct-hemispherical transmittance is fitted to Beer's Law in the form of $T = exp(-fsL)$, the exponential prefactor f is approximately 0.5; this comes from the fact that in the slab, roughly half of the light is scattered forward and half is scattered backward. This prefactor f is plotted as a function of optical thickness in figure 4-8.

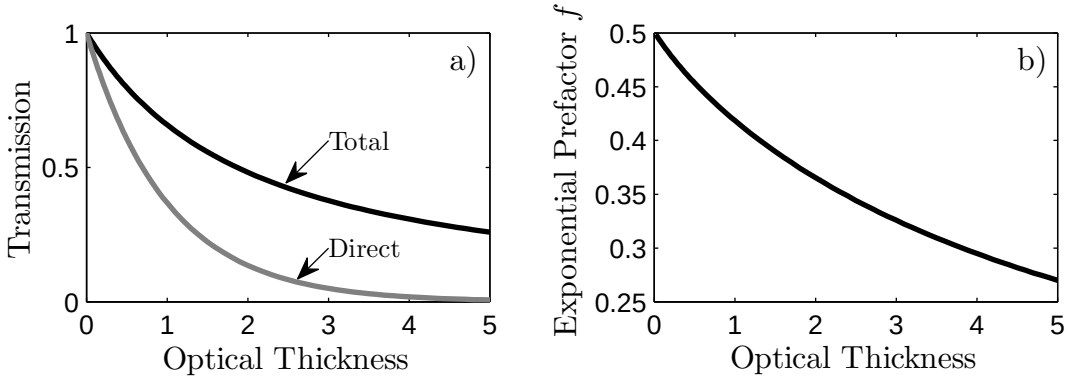

Figure 4-8: (a) The direct-hemispherical transmission through a slab for normal incidence light calculated with the ERT is much larger than the direct-direct transmission calculated with Beer's Law. (b) When Beer's Law is fitted to the direct-hemispherical transmission in the form $T = exp(-fsL)$, the prefactor f is roughly one half.

When calculating the aerogel transmittance at wavelengths where only scattering occurs, two approaches can be taken. If it is known that the incident light will be normal to the surface and that the interface reflectances will not be large, the aerogel direct-hemispherical transmission can be calculated for many narrow wavelength bands by interpolating the direct-hemispherical transmission curve from figure 4-8. If these conditions are not certain to be met, the scattering coefficient can be averaged over distinct bands, and the bands can be calculated in parallel with the other bands using the ERT model. As opposed to the uniform weighting when the IR band properties were calculated, there is essentially no blackbody emission in the sub-1 µm range for temperatures below 1200 °C, so the characteristic spectrum across this range is the incident solar spectrum. Instead of using the inverse of the extinc-

tion coefficient as the effective conductance parameter to be averaged, we can use the calculated direct-hemispherical transmittance as a function of optical thickness as a proxy for conductance. The steps for this method are as follows. First, a band of finite width is chosen. Second, the solar-weighted direct-hemispherical transmittance across this band for slabs of varying thickness are calculated by interpolating from the data plotted in figure 4-8 for each thickness and narrow wavelength band. This we call the true band transmittance, T_{true}. Third, an effective scattering coefficient, s_{band}, is fitted to this band transmittance for an intermediate value of the slab thickness. Fourth, the band transmittance $T_{s_{band}}$ is interpolated from figure 4-8, using s_{band} and a range of varying slab thicknesses. The error due to this band approximation is calculated by comparing $T_{s_{band}}$ to T_{true} for the range of slab thicknesses. If the band approximation error is large, the band is narrowed in width and the process is repeated. Using this procedure, band scattering coefficients were calculated from the three sets of experimental data reproduced in figure 4-2 from Beck et al.[96]. These sets are referenced by their scattering coefficient at 600 nm. The band approximation error is shown in figure 4-9. For all data sets and bands, the error is less than 1%, except in the shortest wavelength band for the highest scattering data set.

Table 4.1: Calculated band scattering coefficients for three scattering data sets identified by their precursor pH. Scattering data from [96].

	s at 600 nm	s_{band} [m^{-1}]			
Precursor pH	[m^{-1}]	250-450 nm	450-550 nm	550-700 nm	700-1000 nm
9	76	368	158	67	22.7
11	14.2	72.5	30.0	12.7	4.3
13	4.3	22.5	9.1	3.9	1.3

There exist little data on extinction in the wavelengths between 1 µm and 1.5 µm. Extrapolating from either the sub-1 µm data or the beyond-1.5 µm data, the expected extinction coefficient would be on the order of $1\,m^{-1}$ for a $100\,kg\,m^{-3}$ aerogel. In an aerogel slab 1 cm thick, this extinction coefficient would only attenuate a beam by 1%. For now we will use the extrapolation from the IR and assume there is some

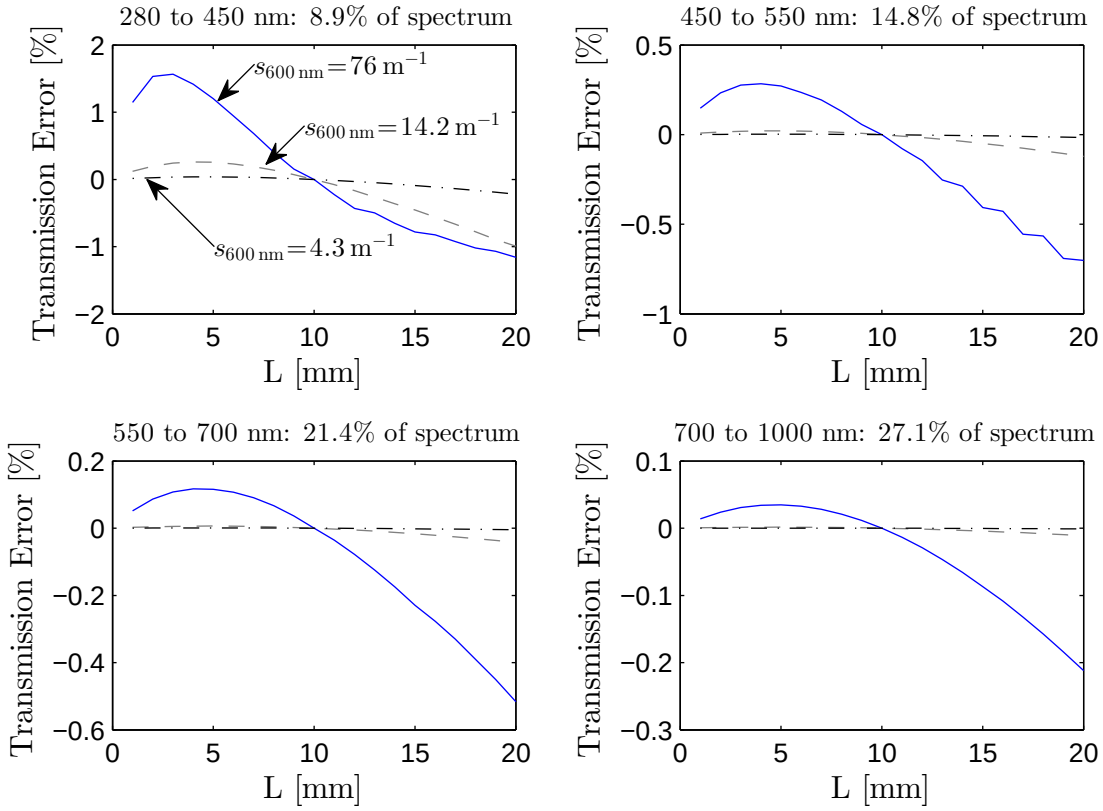

Figure 4-9: In a data set, the effective scattering coefficient for each band, s_{band}, will predict a band transmission that is in error with respect to the fine-meshed solar transmission integration. This error is plotted for four different bands and for four different scattering data sets. Coarseness at very high optical thicknesses is due to the interpolation process.

small absorption in this band. In the future, measurements on aerogel extinction and scattering in the range from 1 to 2 µm would be very useful.

4.3.4 Band Properties of Glass

The real and complex parts of the index of refraction of glass vary strongly with wavelength[93]. The model requires the data to be averaged over the same bands as the aerogel properties. Similar to the aerogels, the properties in bands at wavelengths shorter than 2 µm are averaged using the solar spectrum as a weighting factor; for the rest of the bands, the properties are averaged with equal weight per wavelength. The real part of the index of refraction of each band is averaged and shown in figure 4-10(a). For the imaginary part, the absorption coefficient is calculated from equation (4.29), and then the inverse of the absorption coefficient is averaged (Eq. (4.35)) with either a solar weighting or uniform weighting depending on the band. These averaged properties are shown in figure 4-10(b). Since the bands are given an average absorption coefficient, this results in an imaginary part of the index of refraction that is proportional to the wavelength.

4.4 Results

The methodology outlined above is applied to aerogel-based solar receivers and compared to state-of-the-art selective surface vacuum-gap receivers. Hot-side temperatures ranging from 100 °C, which would be appropriate for any hot-water systems, to 400 °C, which is the typical hot-side operating temperature of concentrated solar power troughs, are investigated. The aerogel-based system uses the properties of aerogels shown previously in the chapter; the density is $80\,\mathrm{kg\,m^{-3}}$ and the visible scattering is that of Beck's least-scattering aerogels (precursor pH=13). The hot surface is a blackbody. The thermal conductivity of the aerogel is $0.005\,\mathrm{W\,m^{-1}\,K}$. For each hot-side temperature, the aerogel thickness is optimized to maximize efficiency.

The results for the aerogel-based receiver are compared to a receiver with a selective surface under glass with a vacuum gap between, similar to a vacuum tube. The

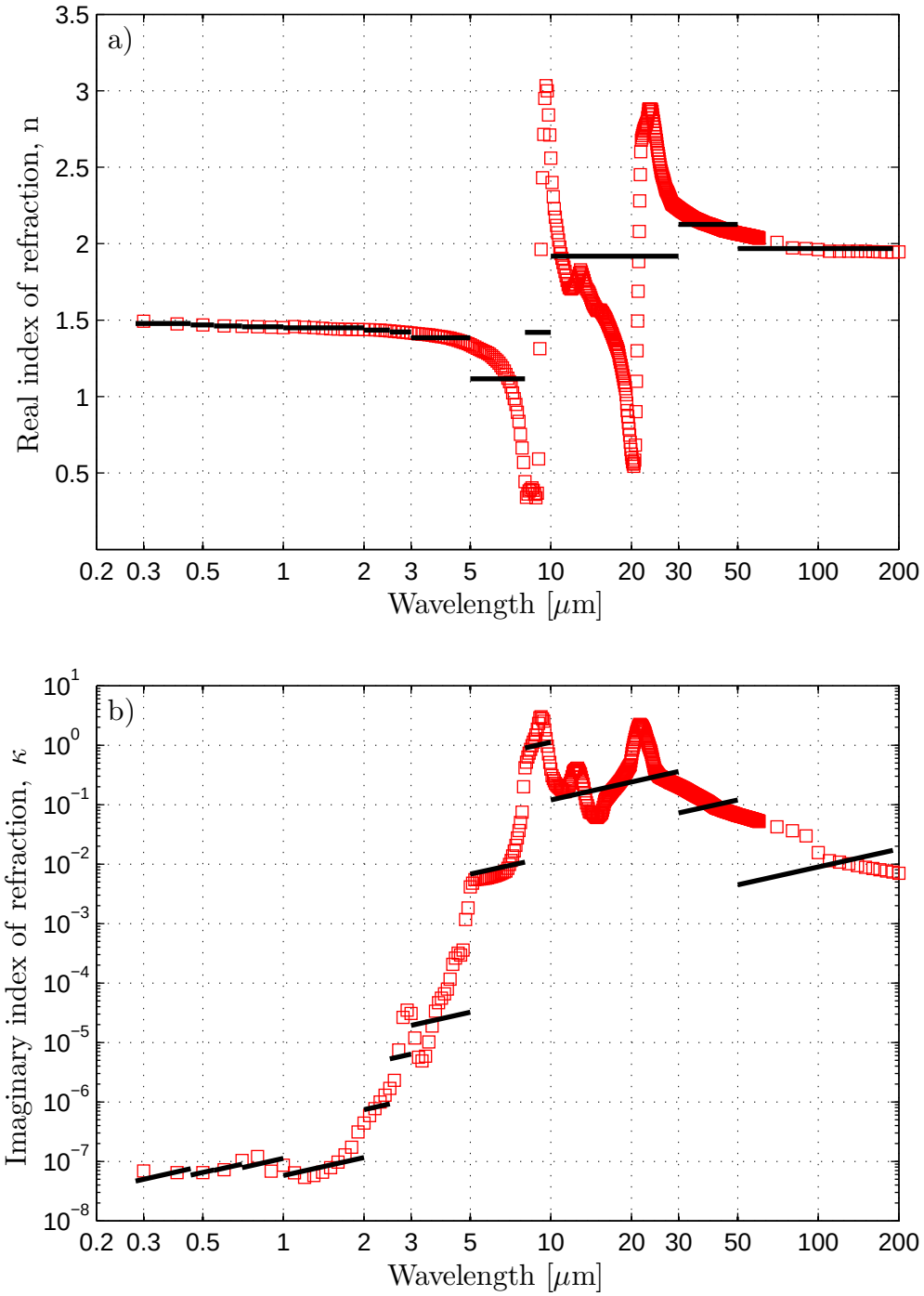

Figure 4-10: The real and imaginary components of the index of refraction of fused silica from [93](dashed lines). The band-averaged properties are shown in solid lines.

performance of this vacuum gap system is modeled with the same equations as the aerogel-based receiver, except in this case the medium (formerly the aerogel, now the vacuum gap) has zero thermal conductivity, an index of refraction of 1, and no extinction at any wavelength. This way the solar flux and the glass calculations are the same for both modeled systems. The selective surface has a temperature-independent spectral emittance of 0.95 at wavelengths less than 2 µm, and an emittance of 0.05 at wavelengths greater than 2 µm. This spectral selectivity results in a total emittance of 5% at 100 °C, increasing to 5.5% at 400 °C. This is a good estimate for the lower temperatures, but underestimates at higher temperatures the emittance of even the best available selective surfaces. Additional performance data has been calculated for a vacuum tube with a blackbody instead of a selective surface to elucidate the source of the performance gains seen in aerogel-based receivers.

At 100 °C, the aerogel-based receiver outperforms the vacuum gap receiver at all receiver flux larger than about 1.5 kW m^{-2}. The receiver efficiency is greater than 80% across the entire range (Fig. 4-11(a)). The optimal aerogel thickness is in the range of nearly 2 cm for the lowest fluxes, to almost nothing for the higher fluxes (Fig. 4-11(b)). At very high fluxes at this low temperature, the radiation losses are insignificant compared to the solar insolation, so the aerogel thickness is small in order to minimize the scattering of the solar flux. The higher glass temperature in the aerogel-based system (Fig. 4-11(c)) indicates that such a system will have slightly higher losses than an evacuated tube receiver. However, these higher losses are offset by the higher absorption of the black body as opposed to the selective surface.

As the temperature increases to 200 °C, the aerogel-based receiver only outperforms the evacuated tube at incident fluxes greater than 6 kW m^{-2} (Fig. 4-12). At these concentrations, the optimal aerogel thickness is less than 2 cm. At temperatures of 300 °C, the performance increase is only seen above 25 kW m^{-2}, where again the optimal thickness is less than 2 cm (Fig. 4-13). At temperatures of 400 °C, the performance benefit is only seen above 60 kW m^{-2}, with optimal thicknesses less than 1 cm (Fig. 4-14).

Over all the temperatures and incident fluxes investigated, the optimal aerogel

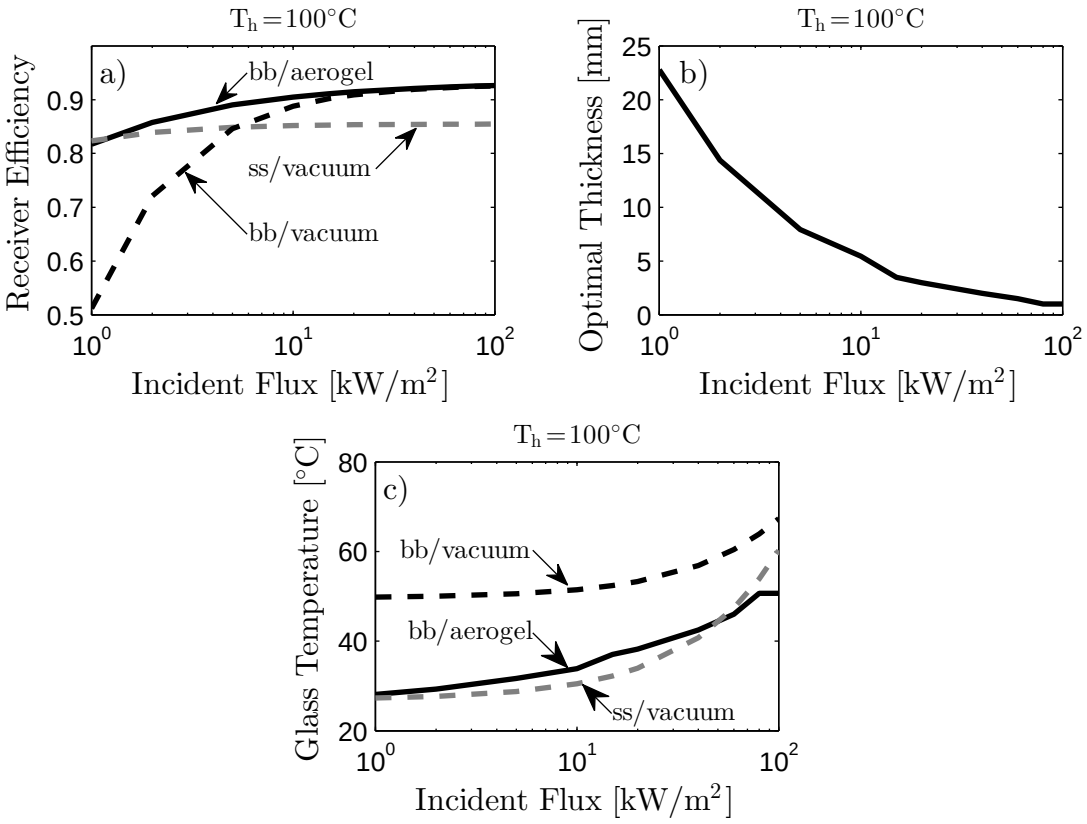

Figure 4-11: (a) The efficiency of solar receivers operating at 100 °C as a function of the solar insolation on the receiver. An aerogel-based solar receiver with a blackbody (bb/aerogel) can achieve higher efficiency than a receiver with a selective surface under a vacuum gap (ss/vacuum). The insulating effect of the aerogel is less important at high insolations, where a blackbody receiver without aerogels (bb/vacuum) does just as well. (b) The optimal aerogel thickness as a function of incident flux. (c) The temperature of the outer surface of the glass.

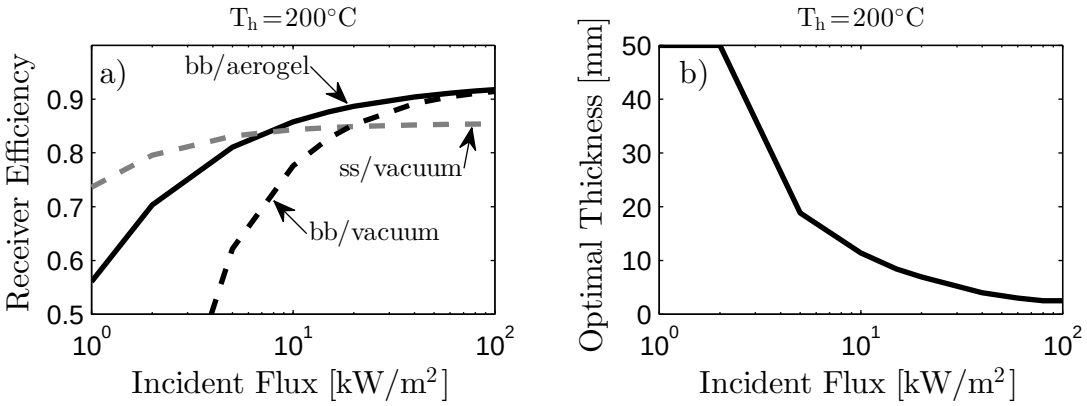

Figure 4-12: (a) The efficiency of solar receivers operating at 200 °C as a function of the solar insolation on the receiver. (b) The optimal aerogel thickness as a function of incident flux.

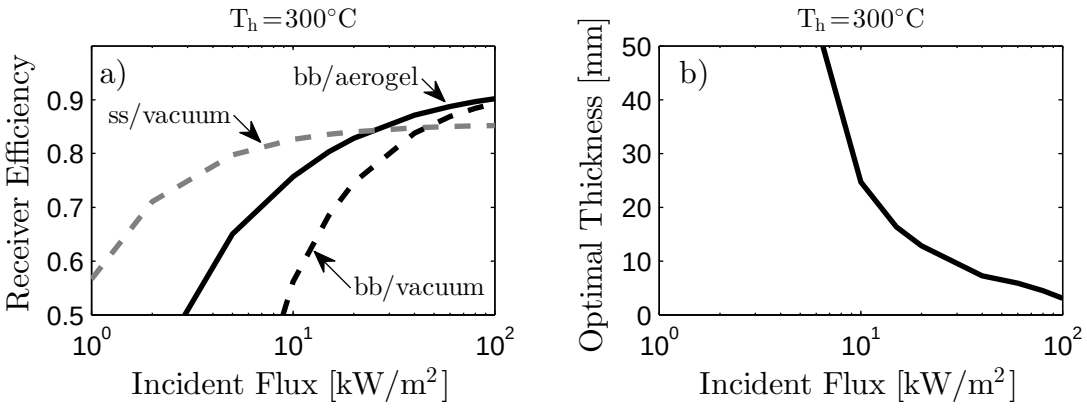

Figure 4-13: (a) The efficiency of solar receivers operating at 300 °C as a function of the solar insolation on the receiver. (b) The optimal aerogel thickness as a function of incident flux.

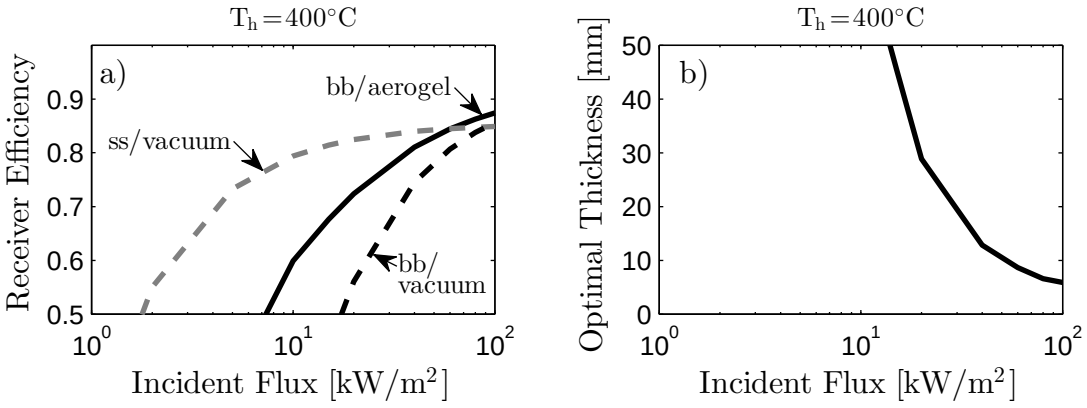

Figure 4-14: (a) The efficiency of solar receivers operating at 400 °C as a function of the solar insolation on the receiver. (b) The optimal aerogel thickness as a function of incident flux.

thicknesses for the situations when the aerogel-based receiver outperforms the vacuum tube are all less than 2 cm, and often less than 1 cm. At higher temperatures, the aerogel-based receiver can be competitive in terms of efficiency only at higher fluxes. In essence, the aerogels are less effective insulators at higher temperatures. For the aerogels described in this work, the average extinction coefficient decreases by an order of magnitude from 100 °C to 400 °C due to the transmission window in the 3 µm to 5 µm range (Fig. 4-15). At 100 °C, less than 5% of the blackbody spectrum falls into this window; at 400 °C, it is more than 35%. The effect of this lower extinction can be seen in the normalized temperature profiles within the aerogel (Fig. 4-16). The higher temperature profile is farther from the linear, diffusive transport.

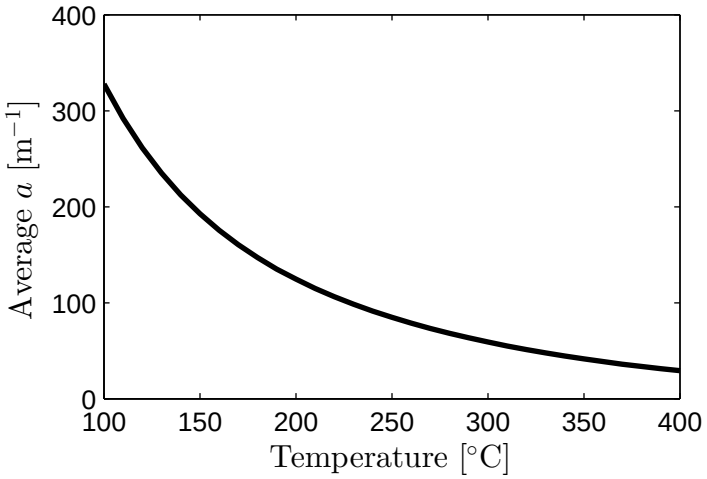

Figure 4-15: The average absorption coefficient in aerogels as a function of temperature.

It is clear that the more transparent window from 3 µm to 5 µm is detrimental to the performance of these aerogels. Fortunately, there are known strategies for increasing absorption in that range. Wei et al. have attributed their higher measured extinction in that range (shown in Fig. 4-1) to their samples not being fully dry, with water absorption as the main cause[91]. In the range from 3 µm to 5 µm, the specific extinction coefficient from Wei et al. is 8.3 m^2 kg^{-1}, nearly 40 times larger than that of the fully dried samples from Heinemann et al. which was used in the previous results. When the model is calculated with this change, the performance results are much

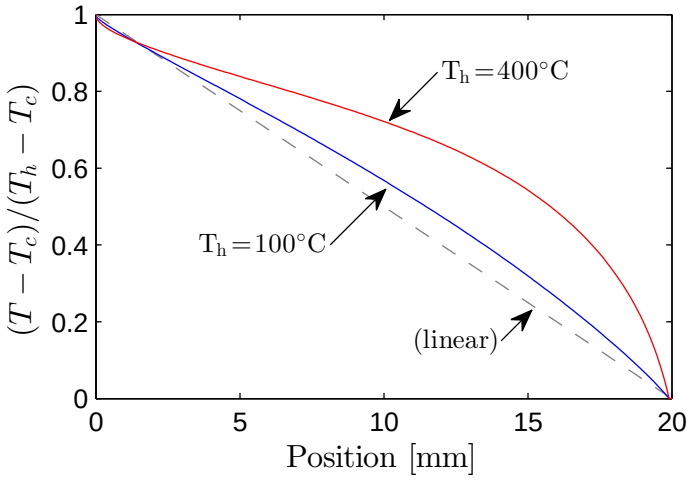

Figure 4-16: The temperature profile within a 2 cm thick aerogel slab. The temperature profiles are normalized to the temperature range. The dashed gray line is a guide for the eye showing a linear profile.

better for the aerogel-based receiver. However, these changes to the IR profile should have some effect on the visible scattering. This effect has not yet been measured, so it is misleading to only look at the improvement in the IR without considering an altered visible scattering.

There is also the possibility to use unevacuated aerogels as insulating layers. Unevacuated aerogels will have a conductivity (excluding radiation) of approximately $0.02\,\mathrm{W\,m^{-1}\,K}$, as opposed to $0.005\,\mathrm{W\,m^{-1}\,K}$ of evacuated aerogels. In the aerogel-based receiver calculations, the effective thermal conductivity of the aerogel, including radiation, is approximately $0.01\,\mathrm{W\,m^{-1}\,K}$. In this case, not evacuating the aerogel would increase the effective thermal conductivity significantly. At higher temperatures, the effective thermal conductivity of the aerogel is much higher, approaching $0.1\,\mathrm{W\,m^{-1}\,K}$ at 400 °C for a 5 cm thick aerogel. At this temperature, not evacuating the aerogel would not have nearly as large an impact on the heat loss through the aerogel.

In practice, unevacuated aerogels must be sealed from the environment, as any water vapor in the air could condense in the aerogel. Condensing water vapor could significantly damage the aerogel structure. On the other hand, adsorbed water also

greatly increases the absorption coefficient in the 3 µm to 5 µm range. If stable aerogels can be made which contain adsorbed water vapor in equilibrium with water vapor, the result could be beneficial in higher-temperature applications where the increase in absorption coefficient outweighs the additional gaseous thermal conductivity. Again, comparing such systems cannot be done until the effects on visible transmission are known.

4.5 Conclusion

At traditional domestic hot water or parabolic trough temperatures, aerogel-based solar thermal receivers can match or outperform the efficiency of vacuum gap selective surface receivers. Because aerogels can act as a structural support for a glass layer, it may be possible to move away from the tube geometry of existing high-efficiency domestic hot water systems that require vacuum and begin to use even higher-efficiency flat panel aerogel receivers. Flat panel systems have the benefits of utilizing much more of the area of a system; using less glass per unit surface area; and eliminating the shading from tubes blocking each other. If it is possible to keep the aerogels dry, it may even be possible to eliminate the need for evacuating the system, which could be a tremendous cost savings. Finally, the aerogel-based systems use a black absorber instead of a selective surface, which could be another cost savings.

All of these potential benefits point toward aerogel-based receivers becoming a serious competitor in the solar thermal market. These calculations predicting better efficiencies than that of vacuum tube systems should inspire researchers to move forward with prototyping and testing of these systems. The major challenges will be manufacturing the aerogels that have the same properties as the best reported in the literature, not just at the lab scale but on the meter-size scale. This may have to be done with tiling of aerogels instead of making monolithic slabs.

Chapter 5

Conclusion

5.1 Summary

Thermoelectric generators show great promise as solid-state heat engines. They can be used for a wide variety of applications, including solar thermoelectric generators. In chapter 2, a model of segmented thermoelectric generators, including parasitic losses such as contact resistances and radiative losses, was presented. The model also elucidated the complex effects of radiation shields on a thermoelectric generator's efficiency. The model was used to model and optimize segmented thermoelectric generators with skutterudite and bismuth telluride legs. The segmented thermoelectric generators were built, and tested on a custom thermoelectric characterization stage. The results of the experiments matched well with the models, with a maximum efficiency of 10.7% seen at a cold side of 25 °C and a hot side of 550 °C. This is the second-highest TEG efficiency ever measured, and the highest measured in this temperature range. In chapter 3, these segmented thermoelectric generators were incorporated in solar thermoelectric generators. These generators were optimized, built, and tested. The devices achieved 5.7% sunlight-to-electricity efficiency at a solar flux of $57\,\mathrm{kW\,m^{-2}}$, the second-highest STEG efficiency ever recorded, and the highest without requiring a solar furnace to generate the optical concentration.

In chapter 4, a model for predicting the performance of flat-plate aerogel-based solar thermal receivers is presented. When the properties of state-of-the-art aerogels

are used for the model, aerogel-based receivers are predicted to outperform traditional vacuum receivers at the operating conditions of no optical concentration, and receiver temperatures of 100 °C. Extending this model, it is also predicted that aerogel-based receivers can outperform vacuum receivers at high temperatures and concentrations. To our knowledge, this is the first prediction of the operation in this regime. This should open up interesting new applications for aerogel-based receivers.

5.2 Future Directions

Solar thermoelectric generators show promise as an energy conversion technology. If they are to have an impact in the energy landscape, cost must be addressed. A full analysis of the cost of STEGs is a large project. First, what would STEGs look like at scale? Would storage be integrated into the STEG? How large can the systems be made? Is the target large-scale plants, or would small domestic systems be appropriate? In any case, cooling the back side of the STEG will be critical. For homes and businesses, it may be possible to integrate STEGs with a domestic hot water or process heat loop on the cooling side. If the cold side temperature is raised significantly, is it still cost-effective to include both skutterudites and bismuth telluride? On the manufacturing end, getting a true cost of the materials and the processes necessary to make these systems must be investigated.

The levelized cost of energy would also improve if the STEGs were more efficient. New thermoelectric materials, such as MgAgSb-based materials, could be good replacements for the bismuth telluride at the cold ends, potentially boosting the efficiency of the TEG. It is also clear that inefficiencies exist in the conversion of sunlight to heat especially with regard to focusing and the small scale of the system. Building a large-scale STEG would require designing and building optics and a tracker to do testing using the sun. Such a system would be a major benefit to this program as well as other solar thermal programs at MIT.

Aerogel solar receivers seem to be very close to a reality. Manufacturers are making aerogel tiles with good visible transparency on a large scale, clearly targeting

solar applications. With this push from industry, the time is ripe to design and test innovative solar thermal receivers which incorporate aerogels. As with the STEGs, having a prototype-scale solar tracker for on-sun testing would be a huge benefit.

If we can push forward these technologies, solar thermal energy could become a serious player in the global energy market. Reliable, cheap energy that can be produced anywhere the sun shines could have a significant impact on the climate, energy independence, and even global access to clean water.

Bibliography

[1] IEA key world energy statistics. Technical report, International Energy Agency, 2013.

[2] International energy outlook 2013. Technical Report DOE/EIA-0484(2013), U.S. Energy Information Administration, 2013.

[3] Renewables 2014 global status report. Technical report, Renewable Energy Policy Network for the 21st Century, 2014.

[4] NARVA Vacuum Tube Information Sheet. `http://nts-solar.com/documents/NARVA-Tube-information.pdf`. Accessed: 2014-06-10.

[5] Solar trough systems. Technical Report 22589, National Renewable Energy Laboratory, 1998.

[6] R. Abbas, J. Muñoz-Anton, M. Valdés, and J.M. Martínez-Val. High concentration linear fresnel reflectors. *Energy Conversion and Management*, 72(0):60 – 68, 2013.

[7] D. R. Mills. Solar process heat: distillation, drying, agricultural and industrial uses. In B. Norton, editor, *Solar Energy The State of The Art*, chapter 9. James & James Ltd., London, 2001.

[8] R. Winston. Solar concentrators. In J. Gordon, editor, *Solar Energy The State of The Art*, chapter 7. James & James Ltd., London, 2001.

[9] E. Altenkirch. Über den nutzeffekt der thermosäule. *Physikalische Zeitschrift*, 10(16):560–568, 1909.

[10] G. J. Snyder and E. S. Toberer. Complex thermoelectric materials. *Nature Materials*, 7(2):105–114, 2008.

[11] M. Telkes. The efficiency of thermoelectric generators. I. *Journal of Applied Physics*, 18(12):1116–1127, 1947.

[12] C. B. Vining, W. Laskow, J. O. Hanson, R. R. Van der Beck, and P. D. Gorsuch. Thermoelectric properties of pressure-sintered $Si_{0.8}Ge_{0.2}$ thermoelectric alloys. *Journal of Applied Physics*, 69(8):4333, 1991.

[13] H.-W. Jeon, H.-P. Ha, D.-B. Hyun, and J.-D. Shim. Electrical and thermoelectrical properties of undoped $Bi_2 - Te_3 - Sb_2Te_3$ and $Bi_2Te_3 - Sb_2Te_3 - Sb_2Se_3$ single crystals. *The Journal of physics and Chemistry of Solids*, 52(4):579–585, 1991.

[14] B. Poudel, Q. Hao, Y. Ma, Y. Lan, A. Minnich, B. Yu, X. Yan, D. Wang, A. Muto, D. Vashaee, X. Y. Chen, J. Liu, M. S. Dresselhaus, G. Chen, and Z. F. Ren. High-thermoelectric performance of nanostructured bismuth antimony telluride bulk alloys. *Science*, 320(5876):634–638, 2008.

[15] W. Xie, J. He, H.-J. Kang, X. Tang, S. Zhu, M. Laver, S. Wang, J. R. D. Copley, C. M. Brown, Q. Zhang, and T. M. Tritt. Identifying the specific nanostructures responsible for the high thermoelectric performance of $(Bi, Sb)_2Te_3$ nanocomposites. *Nano Letters*, 10(9):3283–3289, 2010.

[16] P. F. P. Poudeu, J. D'Angelo, A. D. Downey, J. L. Short, T. P. Hogan, and M. G. Kanatzidis. High thermoelectric figure of merit and nanostructuring in bulk p-type $Na_{1-x}Pb_mSb_yTe_{m+2}$. *Angewandte Chemie International Edition*, 45(23):3835–3839, 2006.

[17] J. P. Heremans, V. Jovovic, E. S. Toberer, A. Saramat, K. Kurosaki, A. Charoenphakdee, S. Yamanaka, and G. J. Snyder. Enhancement of thermoelectric efficiency in PbTe by distortion of the electronic density of states. *Science*, 321(5888):554–557, 2008.

[18] H. Wang, Y. Pei, A. D. LaLonde, and G. J. Snyder. Heavily doped p-type PbSe with high thermoelectric performance: an alternative for pbte. *Advanced materials (Deerfield Beach, Fla.)*, 23(11):1366–1370, 2011.

[19] K. Biswas, J. He, Q. Zhang, G. Wang, C. Uher, V. P. Dravid, and M. G. Kanatzidis. Strained endotaxial nanostructures with high thermoelectric figure of merit. *Nature chemistry*, 3(2):160–166, 2011.

[20] K. Biswas, J. He, I. D. Blum, C.-I. Wu, T. P. Hogan, D. N. Seidman, V. P. Dravid, and M. G. Kanatzidis. High-performance bulk thermoelectrics with all-scale hierarchical architectures. *Nature*, 489(7416):414–418, 2012.

[21] S. N. Girard, J. He, X. Zhou, D. Shoemaker, C. M. Jaworski, C. Uher, V. P. Dravid, J. P. Heremans, and M. G. Kanatzidis. High performance Na-doped PbTe-PbS thermoelectric materials: electronic density of states modification and shape-controlled nanostructures. *Journal of the American Chemical Society*, 133(41):16588–16597, 2011.

[22] Y. Pei, X. Shi, A. LaLonde, H. Wang, L. Chen, and G. J. Snyder. Convergence of electronic bands for high performance bulk thermoelectrics. *Nature*, 473(7345):66–69, 2011.

[23] K. Ahn, M.-K. Han, J. He, J. Androulakis, S. Ballikaya, C. Uher, V. P. Dravid, and M. G. Kanatzidis. Exploring resonance levels and nanostructuring in the PbTe-CdTe system and enhancement of the thermoelectric figure of merit. *Journal of the American Chemical Society*, 132(14):5227–5235, 2010.

[24] K. F. Hsu, S. Loo, F. Guo, W. Chen, J. S. Dyck, C. Uher, T. Hogan, E. K. Polychroniadis, and M. G. Kanatzidis. Cubic $AgPb_mSbTe_{2+m}$: bulk thermoelectric materials with high figure of merit. *Science*, 303(5659):818–821, 2004.

[25] J. Androulakis, K. F. Hsu, R. Pcionek, H. Kong, C. Uher, J. D'Angelo, A. Downey, T. Hogan, and M. G. Kanatzidis. Nanostructuring and high thermoelectric efficiency in p-type $Ag(Pb_{1y}Sn_y)_mSbTe_{2+m}$. *Advanced Materials*, 18(9):1170–1173, 2006.

[26] J. Davidow and Y. Gelbstein. A comparison between the mechanical and thermoelectric properties of three highly efficient p-type GeTe-rich compositions: TAGS-80, TAGS-85, and 3% Bi_2Te_3 – doped $Ge_{0.87}Pb_{0.13}Te$. *Journal of Electronic Materials*, 42(7):1542–1549, 2013.

[27] Jong-S. Rhyee, K. H. Lee, S. M. Lee, E. Cho, S. I. Kim, E. Lee, Y. S. Kwon, J. H. Shim, and G. Kotliar. Peierls distortion as a route to high thermoelectric performance in $In_4Se_{3-\delta}$ crystals. *Nature*, 459(7249):965–968, 2009.

[28] G Rogl, A Grytsiv, P Rogl, E Bauer, and M Zehetbauer. A new generation of p-type didymium skutterudites with high *ZT*. *Intermetallics*, 19(4):546–555, 2011.

[29] X. Shi, J. Yang, J. R. Salvador, M. Chi, J. Y. Cho, H. Wang, S. Bai, J. Yang, W. Zhang, and L. Chen. Multiple-filled skutterudites: high thermoelectric figure of merit through separately optimizing electrical and thermal transports. *Journal of the American Chemical Society*, 133(20):7837–7846, 2011.

[30] Q. Jie, H. Wang, W. S. Liu, H. Wang, G. Chen, and Z. F. Ren. Fast phase formation of double-filled p-type skutterudites by ball-milling and hot-pressing. *Physical Chemistry Chemical Physics*, 15:6809–6816, 2013.

[31] A. May, J.-P. Fleurial, and G. J. Snyder. Thermoelectric performance of lanthanum telluride produced via mechanical alloying. *Physical Review B*, 78(12):125205, 2008.

[32] B. Wölfing, C. Kloc, J. Teubner, and E. Bucher. High performance thermoelectric Tl_9BiTe_6 with an extremely low thermal conductivity. *Physical Review Letters*, 86(19):4350–4353, 2001.

[33] T. Caillat, J.-P. Fleurial, and A. Borshchevsky. Preparation and thermoelectric properties of semiconducting Zn_4Sb_3. *Journal of Physics and Chemistry of Solids*, 58(7):1119–1125, 1997.

[34] S. R. Brown, S. M. Kauzlarich, F. Gascoin, and G. Jeffrey Snyder. $Yb_{14}MnSb_{11}$: New high efficiency thermoelectric material for power generation. *Chemistry of Materials*, 18(7):1873–1877, 2006.

[35] R. Venkatasubramanian, E. Siivola, T. Colpitts, and B. O'Quinn. Thin-film thermoelectric devices with high room-temperature figures of merit. *Nature*, 413(6856):597–602, 2001.

[36] T C Harman, P J Taylor, M P Walsh, and B E LaForge. Quantum dot superlattice thermoelectric materials and devices. *Science (New York, N.Y.)*, 297(5590):2229–2232, 2002.

[37] C. A. Domenicali. Irreversible thermodynamics of thermoelectric effects in inhomogeneous, anisotropic media. *Physical Review*, 92(4):877–881, Nov 1953.

[38] H. J. Goldsmid. *Applications of Thermoelectricity*. Methuen and Co., London, 1960.

[39] K. McEnaney. Modeling of solar thermal selective surfaces and thermoelectric generators. Master's thesis, Massachusetts Institute of Technology, 2010.

[40] A. J. Minnich, M. S. Dresselhaus, Z. F. Ren, and G. Chen. Bulk nanostructured thermoelectric materials: current research and future prospects. *Energy and Environmental Science*, 2:466–479, 2009.

[41] A. N. Himle, D. S. Brush, J. B. Roes, and E. L. Brady. Flat-plate solar thermoelectric conversion panels. Technical Report ASD-TDR-62-214, General Atomic Division of General Dynamics Corporation, May 1962.

[42] Nicholas Fuschillo, R. Gibson, and F. K. Eggleston. Theory and performance of flat plate solar thermoelectric generator for near-earth orbits. In *Supplement to IEEE Transactions on Aerospace*, pages 652–663, Houston, TX, June 1965. Proceedings of the Aerospace Technical Conference and Exhibit.

[43] E. Gross, M. Riffel, and U. Sthrer. Thermoelectric generators made of $FeSi_2$ and HMS: Fabrication and measurement. *Journal of Materials Research*, 10:34–40, 1 1995.

[44] T. Caillat, J.-P. Fleurial, G.N. Snyder, and A Borshchevsky. Development of high efficiency segmented thermoelectric unicouples. In *Twentieth International Conference on Thermoelectrics*, pages 282–285, 2001.

[45] M. S. El-Genk, F. H. Saber, J. Sakamoto, and T. Caillat. Life tests of a skutterudites thermoelectric unicouple (MAR-03). In *Twenty-second International Conference on Thermoelectrics*, pages 417–420, 2003.

[46] D. Crane, D. Kossakovski, and L. Bell. Modeling the building blocks of a 10% efficient segmented thermoelectric power generator. *Journal of Electronic Materials*, 38:1382–1386, 2009.

[47] J. D'Angelo, E. D. Case, N. Matchanov, C.-I. Wu, T. P. Hogan, J. Barnard, C. Cauchy, T. Hendricks, and M. G. Kanatzidis. Electrical, thermal, and mechanical characterization of novel segmented-leg thermoelectric modules. *Journal of Electronic Materials*, 40(10):2051–2062, 2011.

[48] J.Q. Guo, H.Y. Geng, T. Ochi, S. Suzuki, M. Kikuchi, Y. Yamaguchi, and S. Ito. Development of skutterudite thermoelectric materials and modules. *Journal of Electronic Materials*, 41(6):1036–1042, 2012.

[49] A. Muto, J. Yang, B. Poudel, Z. F. Ren, and G. Chen. Skutterudite unicouple characterization for energy harvesting applications. *Advanced Energy Materials*, 3(2):245–251, 2013.

[50] J. R. Salvador, J. Y. Cho, Z. Ye, J. E. Moczygemba, A. J. Thompson, J. W. Sharp, J. D. Koenig, R. Maloney, T. Thompson, J. Sakamoto, H. Wang, and A. A. Wereszczak. Conversion efficiency of skutterudite-based thermoelectric modules. *Phys. Chem. Chem. Phys.*, 16:12510–12520, 2014.

[51] T. Caillat, S. Firdosy, B. C.-Y. Li, C.-K. Huang, B. Cheng, J. Paik, J. Chase, T. Arakelian, L. Lara, and J.-P. Fleurial. Progress status of the development of high-efficiency segmented thermoelectric couples. In *Nuclear and Emerging Technologies for Space*, 2012.

[52] J. Yang and T. Caillat. Thermoelectric materials for space and automotive power generation. *MRS Bulletin*, 31:224–229, 3 2006.

[53] E. Weston. U.S. Patent No. 389,124, 1888.

[54] W. W. Coblentz. Harnessing heat from the sun. *Scientific American*, 127(5):324, 1922.

[55] M. Telkes. Solar thermoelectric generators. *Journal of Applied Physics*, 25(6):765–777, 1954.

[56] N. F. Schuh and R. J. Tallent. Solar-powered thermoelectric generator design considerations. *Electrical Engineering*, 78:345–352, 1959.

[57] G. W. Glassburn. Flat plate solar thermoelectric generator orbital experiment. *IEEE Transactions on Aerospace*, 1(2):1396 –1403, 1963.

[58] R. Rush. Solar flat plate thermoelectric generator research. Technical Report APL TDR 64-87, General Instrument Corporation, September 1964.

[59] N. Fuschillo, R. Gibson, F. K. Eggleston, and J. Epstein. Flat plate solar thermoelectric generator for near-earth orbits. *Advanced Energy Conversion*, 6(2):103 – 118, IN3–IN6, 119–125, 1966.

[60] V. Raag. Solar thermoelectric generator design and panel development program. Technical Report CR-72340, NASA, December 1967.

[61] M. Swerdling and V. Raag. Solar thermoelectric power generation for Mercury orbiter missions. *Journal of Energy*, 3(5):291–298, 1979.

[62] D. M. Rowe. A high performance solar powered thermoelectric generator. *Applied Energy*, 8(4):269 – 273, 1981.

[63] R. Amatya and R. Ram. Solar thermoelectric generator for micropower applications. *Journal of Electronic Materials*, 39:1735–1740, 2010. 10.1007/s11664-010-1190-8.

[64] C. L. Dent and M. H. Cobble. A solar thermoelectric generator and analysis. In *Proceedings of the Fourth International Conference on Thermoelectric Energy Conversion*, pages 75–78, Arlington, TX, 1982.

[65] D. Kraemer, B. Poudel, H.-P. Feng, J. C. Caylor, B. Yu, X. Yan, Y. Ma, X. Wang, D. Wang, A. Muto, K. McEnaney, M. Chiesa, Z. F. Ren, and G. Chen. High-performance flat-panel solar thermoelectric generators with high thermal concentration. *Nature Materials*, 10(7):532 – 538, 2011.

[66] K. McEnaney, D. Kraemer, Z. Ren, and G. Chen. Modeling of concentrating solar thermoelectric generators. *Journal of Applied Physics*, 110(7):074502, 2011.

[67] K. McEnaney, D. Kraemer, and G. Chen. Direct heat-to-electricity conversion of solar energy. In G. Chen, V. Prasad, and Y. Jaluria, editors, *Annual Review of Heat Transfer*, chapter 6. Begell House, New York, 2012.

[68] T. P. Hogan and T. Shih. Modeling and characterization of power generation modules based on bulk materials. In D. M. Rowe, editor, *Thermoelectrics Handbook: Macro to Nano*, chapter 12. CRC Press, New York, 2006.

[69] D. Kraemer, F. Cao, K. McEnaney, Z.F. Ren, and G. Chen. Accurate determination of the total hemispherical emittance and solar absorptance of opaque surfaces at elevated temperatures. *Solar Energy Materials and Solar Cells (submitted)*, 2014.

[70] Standard terminology of solar energy conversion. Technical Report ASTM Standard E 772-11, ASTM International, 2011.

[71] S. H. P. Chen and S. C. Saxena. Experimental determination of hemispherical total emittance of metals as a function of temperature. *Industrial and Engineering Chemistry Fundamentals*, 12(2):220–224, 1973.

[72] S. S. Kistler. Coherent expanded aerogels and jellies. *Nature*, 127:741, 1931.

[73] S. S. Kistler. Coherent expanded aerogels. *The Journal of Physical Chemistry*, 36(1):52–64, 1932.

[74] S. S. Kistler and A. G. Caldwell. Thermal conductivity of silica aerogel. *Industrial and Engineering Chemistry*, 26(6):658–662, 1934.

[75] S. S. Kistler. The relation between heat conductivity and structure in silica aerogel. *The Journal of Physical Chemistry*, 39(1):79–86, 1935.

[76] J. F. White. Silica aerogel: Effect of variables on its thermal conductivity. *Industrial and Engineering Chemistry*, 31(7):827–831, 1939.

[77] E. Ponthieu, J. Grimblot, E. Elaloui, and G. M. Pajonk. Synthesis and characterization of pure and yttrium-containing alumina aerogels. *Journal of Materials Chemistry*, 3(3):287–293, 1993.

[78] T. F. Baumann, A. E. Gash, S. C. Chinn, A. M. Sawvel, R. S. Maxwell, and J. H. Satcher. Synthesis of high-surface-area alumina aerogels without the use of alkoxide precursors. *Chemistry of Materials*, 17(2):395–401, 2005.

[79] L. K. Campbell, B. K. Na, and E. I. Ko. Synthesis and characterization of titania aerogels. *Chemistry of Materials*, 4(6):1329–1333, 1992.

[80] C. J. Brinker, K. J. Ward, K. D. Keefer, E. Holupka, P. J. Bray, and R. K. Pearson. Synthesis and structure of borate based aerogels. In J. Fricke, editor, *Aerogels*, volume 6 of *Springer Proceedings in Physics*, pages 57–67. Springer Berlin Heidelberg, 1986.

[81] C. J. Brinker and G. W. Scherer. *Sol-Gel Science*. Academic Press, Boston, 1990.

[82] R. W. Pekala. Organic aerogels from the polycondensation of resorcinol with formaldehyde. *Journal of Materials Science*, 24:3221–3227, 1989.

[83] S. Al-Muhtaseb and J. A. Ritter. Preparation and properties of resorcinol-formaldehyde organic and carbon gels. *Advanced Materials*, 15(2):101–114, 2003.

[84] U. Heinemann, R. Caps, and J. Fricke. Radiation-conduction interaction: an investigation on silica aerogels. *International journal of heat and mass transfer*, 39(10):2115–2130, 1996.

[85] M. Rubin and C. M. Lampert. Transparent silica aerogels for window insulation. *Solar Energy Materials*, 7:393–400, 1983.

[86] R. Caps and J. Fricke. Infrared radiative heat transfer in highly transparent silica aerogel. *Solar Energy*, 36(4):361–364, 1986.

[87] P. H. Tewari, A. J. Hunt, and K. D. Lofftus. Advances in production of transparent silica aerogels for window glazings. In J. Fricke, editor, *Aerogels*, volume 6 of *Springer Proceedings in Physics*, pages 31–37. Springer Berlin Heidelberg, 1986.

[88] P. Scheuerpflug, R. Caps, D. Buttner, and J. Fricke. Apparent thermal conductivity of evacuated SiO_2-aerogel tiles under variation of radiative boundary conditions. *International Journal of Heat and Mass Transfer*, 28(12):2299–2306, 1985.

[89] J. Hartmann, M. Rubin, and D. Arasteh. Thermal and solar-optical properties of silica aerogel for use in insulated windows. In D. Andrejko, editor, *Proceedings of the 12th Annual Passive Solar Conference*, Portland, OR, 1987. American Solar Energy Society.

[90] J. Zarzycki and T. Woignier. Aerogels: Precursors or end materials? In J. Fricke, editor, *Aerogels*, volume 6 of *Springer Proceedings in Physics*, pages 42–48. Springer Berlin Heidelberg, 1986.

[91] G. Wei, Y. Liu, X. Zhang, and X. Du. Radiative heat transfer study on silica aerogel and its composite insulation materials. *Journal of Non-Crystalline Solids*, 362:231–236, 2013.

[92] G. Wei, Y. Liu, X. Zhang, F. Yu, and X. Du. Thermal conductivities study on silica aerogel and its composite insulation materials. *International Journal of Heat and Mass Transfer*, 54(11-12):2355–2366, 2011.

[93] R. Kitamura, L. Pilon, and M. Jonasz. Optical constants of silica glass from extreme ultraviolet to far infrared at near room temperature. *Applied optics*, 46(33):8118–8133, 2007.

[94] A. J. Hunt and P. Berdahl. Structure data from light scattering studies of aerogel. In *Symposium B Better Ceramics Through Chemistry I*, volume 32 of *MRS Proceedings*, pages 275–280, 1984.

[95] E. Elaloui, P. Achard, B. Chevalier, J. L. Chevalier, M. Durant, and G. M. Pajonk. Improved monolithic aerogel for transparent glass spacer in innovative windows. In A. Hugot-Le Goff, C. M. Lampert, and C.-G. Granqvist, editors, *Optical Materials Technology for Energy Efficiency and Solar Energy Conversion*, volume 1727, pages 402–415, Tolouse-Labege, France, 1992.

[96] A. Beck, G. Popp, A. Emmerling, and J. Fricke. Preparation and characterization of sio2 two-step aerogels. *Journal of Sol-Gel Science and Technology*, 2:917–920, 1994.

[97] W. Cao and A. J. Hunt. Improving the visible transparency of silica aerogels. *Journal of Non-Crystalline Solids*, 176(1):18–25, 1994.

[98] G. M. Pajonk, E. Elaloui, B. Chevalier, and R. Begag. Optical transmission properties of silica aerogels prepared from polyethoxidisiloxanes. *Journal of Non-Crystalline Solids*, 210(2-3):224–231, 1997.

[99] K. Duer and S. Svendsen. Monolithic silica aerogel in superinsulating glazings. *Solar Energy*, 63(4):259–267, 1998.

[100] A. J. Hunt and M. R. Ayers. Light scattering studies of UV-catalyzed gel and aerogel structure. *Journal of non-crystalline solids*, 225:325–329, 1998.

[101] P. B. Wagh and S. V. Ingale. Comparison of some physico-chemical properties of hydrophilic and hydrophobic silica aerogels. *Ceramics International*, 28:43–50, 2002.

[102] G. Reichenauer, J. Fricke, J. Manara, and J. Henkel. Switching silica aerogels from transparent to opaque. *Journal of Non-Crystalline Solids*, 350:364–371, 2004.

[103] A. Emmerling, R. Petricevic, A. Beck, P. Wang, H. Scheller, and J. Fricke. Relationship between optical transparency and nanostructural features of silica aerogels. *Journal of Non-Crystalline Solids*, 185(3):240–248, 1995.

[104] M. F. Modest. *Radiative Heat Transfer*. Academic Press, Boston, second edition, 2003.

[105] A. Beck, R. Caps, and J. Fricke. Scattering of visible light from silica aerogels. *Journal of Physics D: Applied Physics*, 22:730–734, 1989.

[106] K. Kamiuto, S. Saitoh, and Y. Tokita. Scattering phase function of a silica aerogel at 450 nm wavelength. *Journal of Quantitative Spectroscopy and Radiative Transfer*, 50(3):293–299, 1993.

[107] R. Stangl, M.-A. Einarsrud, W. Platzer, and V. Wittwer. Optical characterization of silica xerogel with spectral and angle-dependent resolution. *Solar Energy Materials and Solar Cells*, 54(1-4):181–188, 1998.

[108] L. B. Evans, C. M. Chu, and S. W. Churchill. The effect of anisotropic scattering on radiant transport. *Journal of Heat Transfer*, 87(3):381–387, 1965.

[109] J. Schultz, K. Jensen, and F. Kristiansen. Super insulating aerogel glazing. *Solar Energy Materials and Solar Cells*, 89(2-3):275–285, 2005.

[110] J. Fricke, R. Caps, D. Buttner, U. Heinemann, and E. Hummer. Silica aerogel - a light-transmitting thermal superinsulator. *Journal of Non-Crystalline Solids*, 95:1167–1174, 1987.

[111] A. Beck, W. Körner, and J. Fricke. Optical investigations of granular aerogel fills. *Journal of Physics D: Applied Physics*, 27(1):13–18, 1994.

[112] M. Dowson, I. Pegg, D. Harrison, and Z. Dehouche. Predicted and in situ performance of a solar air collector incorporating a translucent granular aerogel cover. *Energy and Buildings*, 49:173–187, 2012.

[113] A. Nordgaard and W. A. Beckman. Modelling of flat-plate collectors based on monolithic silica aerogel. *Solar Energy*, 49(5):387–402, 1992.

[114] S. Svendsen. Solar collector with monolithic silica aerogel. *Journal of Non-Crystalline Solids*, 145:240–243, 1992.

[115] D. Lee, P. C. Stevens, S. Q. Zeng, and A. J. Hunt. Thermal characterization of carbon-opacified silica aerogels. *Journal of Non-Crystalline Solids*, 186:285–290, 1995.

[116] S. Q. Zeng, A. Hunt, and R. Greif. Geometric structure and thermal conductivity of porous medium silica aerogel. *Journal of Heat Transfer*, 117(4):1055–1058, 1995.

[117] M. Reim, G. Reichenauer, W. Körner, J. Manara, M. Arduini-Schuster, S. Korder, A. Beck, and J. Fricke. Silica-aerogel granulate structural, optical and thermal properties. *Journal of Non-Crystalline Solids*, 350:358–363, 2004.

[118] S. Spagnol, B. Lartigue, A. Trombe, and F. Despetis. Experimental investigations on the thermal conductivity of silica aerogels by a guarded thin-film-heater method. *Journal of Heat Transfer*, 131(7):074501, 2009.

[119] K. Swimm, G. Reichenauer, S. Vidi, and H.-P. Ebert. Gas pressure dependence of the heat transport in porous solids with pores smaller than 10 μm. *International Journal of Thermophysics*, 30(4):1329–1342, 2009.

[120] E. Cohen. Thermal properties of advanced aerogel insulation. Master's thesis, Massachusetts Institute of Technology, 2011.

[121] J. Fricke and T. Tillotson. Aerogels: production, characterization, and applications. *Thin Solid Films*, 297(1-2):212–223, 1997.

[122] T. Xie, Y.-L. He, and Z.-J. Hu. Theoretical study on thermal conductivities of silica aerogel composite insulating material. *International Journal of Heat and Mass Transfer*, 58(1-2):540–552, 2013.

[123] S. P.C. Marques, E. J. Barbero, and J. S.R. Murillo. Analysis of conduction-radiation problem in absorbing and emitting nongray materials. *International Journal of Numerical Methods for Heat & Fluid Flow*, 19(2):165–181, 2009.

[124] S. Henning and L. Svensson. Production of silica aerogel. *Physica Scripta*, 23:697–702, 1981.